

**Star Formation in the Central 400 pc of the Milky Way:
Evidence for a Population of Massive YSOs**

F. Yusef-Zadeh¹, J. W. Hewitt¹, R. G. Arendt², B. Whitney³, G. Rieke⁴, M. Wardle⁵, J. L. Hinz⁴,
S. Stolovy⁶, C. C. Lang⁷, M. G. Burton⁸, S. Ramirez⁶

ABSTRACT

The central kpc of the Milky Way might be expected to differ significantly from the rest of the Galaxy with regard to gas dynamics and the formation of young stellar objects (YSOs). We probe this possibility with mid-infrared observations obtained with IRAC and MIPS on Spitzer and with MSX. We use color-color diagrams and spectral energy distribution (SED) fits to explore the nature of YSO candidates (including objects with $4.5\mu\text{m}$ excesses possibly due to molecular emission). There is an asymmetry in the distribution of the candidate YSOs, which tend to be found at negative Galactic longitudes; this behavior contrasts with that of the molecular gas, approximately 2/3 of which is at positive longitudes. The small scale height of these objects suggests that they are within the Galactic center region and are dynamically young. They lie between two layers of infrared dark clouds (IRDCs) and may have originated from these clouds. We identify new sites for this recent star formation by comparing the mid-IR, radio, submillimeter, and methanol maser data. The methanol masers appear to be associated with young, embedded YSOs characterized by $4.5\mu\text{m}$ excesses. We use the SEDs of these sources to estimate their physical characteristics; their masses appear to range from ~ 10 to $\sim 20 M_{\odot}$. Within the central 400×50 pc ($|l| < 1.3^{\circ}$ and $|b| < 10'$) the star formation rate based on the identification of Stage I evolutionary phase of YSO candidates is about $0.14 M_{\odot} \text{ yr}^{-1}$. Given that the majority of the sources in the population of YSOs are classified as Stage I objects, we suggest that a recent burst of star formation took place within the last 10^5 years. This suggestion is also consistent with estimates of star formation rates within the last $\sim 10^7$ years showing a peak around 10^5 years ago. Lastly, we find that the Schmidt-Kennicutt Law applies well in the central 400 pc of the Galaxy. This implies that star formation does not appear to be dramatically affected by the extreme physical conditions in the Galactic center region.

Subject headings: Galaxy: center - clouds - ISM: general - ISM - radio continuum - masers - cosmic rays - stars: formation - galaxies: starburst

1. Introduction

Understanding the processes occurring in the nuclear disk of our own Galaxy is interesting not only for insight into our own Milky Way Galaxy, but also because its study can potentially provide a template to the closest galactic nuclei. This important region of the Galaxy hosts several sources of energetic activity, and is the site of massive molecular clouds with pockets of past and present massive star formation. On a larger scale, the distribution of molecular clouds is asymmetric in the so-called “central molecular zone” showing 2/3 of the molecular gas on the positive longitude side of the Galactic center region (Bania 1977; Bally et al. 1988; Oka et al. 2005; Tsuboi et al. 1999; Martin et al. 2004; Morris & Serabyn 1996). The nature of this asymmetry in the context of gas dynamics is not understood. This unique region is also distinguished from the rest of the Galaxy by the presence of a bar that is responsible for feeding gas into the central few hundred parsecs of the Galaxy. In particular, the non-circular motion of the gas in this region is thought to be induced by the bar’s potential combined with dynamical friction leading to migration of molecular clouds to the Galactic center (Binney et al. 1991; Stark et al. 1991). The collision of these migrating molecular clouds with each other in a small volume of the Galactic center is thought to be the driving mechanism for star formation on a wide range of scales (Wardle & Yusef-Zadeh 2008). Thus, it is possible that the star formation process depends on the Galactic center environment including the effects of the bar on the gas dynamics.

Although there is a high concentration of dense molecular clouds distributed in the Galactic center region, the star formation rate has shown extreme values. On the one hand, the massive star forming region Sgr B2 points to the closest example of starburst activity in our Galaxy. This region contains some of the most spectacular young and dense stellar clusters having an age of a few million years (Figer et al. 1999; Paumard et al. 2006; Lu et al. 2006). In the context of recently formed stars in the nuclear disk, detailed study using Infrared Space Observatory (ISO) at 7 and $15\mu\text{m}$ indicates the presence of a population of young stellar object (YSO) candidates in the region $-0.424^\circ < l < -0.115^\circ$ and $-0.194^\circ < b < 0.089^\circ$ (Omont 2003; Schuller et al. 2006). On the other hand, quiescent giant molecular clouds such as G0.25-0.01 (Lis & Carlstrom 1994; Lis & Menten

¹Department of Physics and Astronomy, Northwestern University, Evanston, IL 60208 (zadeh@northwestern.edu)

²Science Systems and Applications, Inc. and University of Maryland - Baltimore County, GSFC, Code 665, Greenbelt, MD 20771

³Space Science Institute, 4750 Walnut Street, Suite 205, Boulder, CO 80301

⁴Steward Observatory, University of Arizona, 933 North Cherry Avenue, Tucson, AZ 85721

⁵Department of Physics and Engineering, Macquarie University, Sydney, NSW 2109, Australia

⁶Spitzer Science Center, California Institute of Technology, Mail Code 220-6, 1200 East California Boulevard, Pasadena, CA 91125

⁷Department of Physics & Astronomy, University of Iowa, Iowa City, IA 52245, USA

⁸School of Physics, University of New South Wales, Sydney, NSW 2052, Australia

1998) appear to contain highly inefficient star formation.

One intriguing question is whether the star formation in this region proceeds analogously to that elsewhere in the Galaxy, or whether the central region provides a unique environment and might provide a template for alternative modes of star formation in galactic nuclei generally. For example, the molecular clouds in the Galactic center region have elevated temperatures. Molecular line studies yield temperature estimates of 75 to 200K (Hüttemeister et al. 1993), while far-infrared data indicate dust temperatures $\leq 30\text{K}$ (Odenwald & Fazio 1984; Cox & Laureijs 1989; Pierce-Price et al. 2000). This temperature discrepancy suggests direct heating of the molecular gas either by cosmic rays or shocks, which may reduce the efficiency of star formation in the region (Lis et al. 2001b; Yusef-Zadeh et al. 2007b).

In order to census past and present star formation activity and to gain insight into the nature of star formation in the unique environment of the Galactic center, we carried out a $24\mu\text{m}$ survey of the central molecular zone and beyond between $|l| < 4^\circ$ and $|b| < 1^\circ$. This is the most recent in a series of papers that have presented sensitive surveys of the Galactic center region at near-IR and mid-IR wavelengths. Our MIPS survey provides an important data point when combined with the *Spitzer Infrared Array Camera* survey of the Galactic center region (Ramirez et al. 2008; Stolovy et al. 2006; Arendt et al. 2008). This allows us to distinguish YSOs and AGBs by fitting the spectral energy distribution (SED) of infrared point sources as well as by constructing color magnitude diagrams (CMDs). Furthermore, $24\mu\text{m}$ observations reveal dense, cold dust clouds through their absorption against background emission and identify warm dust clouds through their emission without being contaminated by PAH emission. The presence of large-scale IRDCs in the Galactic center at this wavelength traces potential sites of the earliest phase of active and quiescent star formation. In particular, the correlation of $24\mu\text{m}$ point sources distributed toward infrared dark clouds with $4.5\mu\text{m}$ excess sources, thought to trace shock excited molecular emission, can be used to identify the earliest phase of massive star formation (Chambers et al. 2009). Lastly, $24\mu\text{m}$ emission points to HII regions with embedded thermal sources of heating as well as to sites where synchrotron emission from relativistic particles is produced. The ratio of $24\mu\text{m}$ to radio emission can separate thermal from nonthermal sources (Fuerst et al. 1987).

The structure of this paper is as follows. Section 2 describes details of observations using MIPS, IRAC, and radio data, while section 3 presents the large scale distribution of extended clouds and compact stellar sources. Then in section 4 we focus on the stellar distribution of $24\mu\text{m}$ sources and the color magnitude diagram of the sources covered by the MIPS and IRAC surveys. Section 5 discusses the SEDs of candidate YSOs followed by a brief description of individual candidate sites of on-going star formation activity. The new sites of young, massive star formation are found by the detection of sources with excess $4.5\mu\text{m}$ emission. There is a rich collection of prominent infrared sources toward the Galactic center, some of which such as Sgr A, the radio Arc and Sgr C, are saturated. We discuss elsewhere the distribution of $24\mu\text{m}$ emission from Sgr A (G0.0-0.0) and the Galactic center radio Arc (G0.2-0.0), the Sgr B HII complex (G0.7-0.0) and G0.6-0.0, Sgr C (G359.4-0.1), Sgr E (G358.7-0.0) and the Tornado nebula. Here we assume the distance to the

Galactic center is 8.5 kpc (Ghez et al. 2008).

2. Observations and Data Reductions

Apart from the $24\mu\text{m}$ survey, several other surveys of this region have recently been carried out in other wavelength bands, as described briefly below. We have correlated these data with our MIPS survey data.

2.1. MIPS Survey at $24\mu\text{m}$

The Galactic Center region is very bright at mid-IR wavelengths. Therefore, to cover the full $8 \times 2^\circ$ survey area most efficiently, we used MIPS in fast scan mode with large cross-scan steps of $302''$. Because of the permitted scan orientation during the Galactic center visibility window, the map was a parallelogram. This fast scan mode achieved enough individual source sightings for high reliability and reached the specified 1 mJy detection limit. Eight rectangular scans were performed in sequence, each taking approximately 2.3 hours, giving a total observing time of ~ 18 hours. The diffraction limit of the $24\mu\text{m}$ image is $5.8''^2$. These data represent the highest spatial resolution and sensitivity large-scale map made of the inner few degrees of the Galactic center at $24\mu\text{m}$. The source photometry was based on the $24\mu\text{m}$ catalog compiled by Hinz et al. (2009).

Our data are complemented by the *Spitzer* Legacy program MIPS Inner Galactic Plane Survey (MIPSGAL) which observed 220 deg^2 of the inner Galactic plane, $65^\circ > l > 10^\circ$ and $-10^\circ > b > -65^\circ$ for $|b| < 1^\circ$, at 24 and $70 \mu\text{m}$ (Carey et al. 2009) which avoided duplicating coverage of the Galactic center region. MIPSGAL-II post-BCD data were used to fill gaps around the high latitude edges. This was done by reprojecting the MIPSGAL II data over the whole field. The MIPSGAL data are only used where there is zero coverage at the edges of the mosaic.

There are several HII regions where the $24\mu\text{m}$ emission is saturated. The most extended saturated regions lie toward Sgr A, the radio Arc and Sgr C, near $l \sim 0^\circ, 0.2^\circ, 0.6^\circ$, respectively. The point source saturation limit, depending on the background level, ranges between 4 and 4.5 Jy which correspond to 0.60 and 0.51 magnitudes at $24 \mu\text{m}$. In order to remedy the saturation artifacts, we replaced the saturated regions by MSX Band E data ($21.34 \mu\text{m}$) using the following steps. (1) The MSX data are reprojected to match the pixel scale and alignment of the MIPS image. A relative distortion between the positions of sources in MSX and MIPS images was corrected by a 4th-order 2-D polynomial warping of the MSX images. This correction reduced positional differences to ~ 0.5 pixels ($2.49''$ pixels). (2) A linear fit to the correlation between pixel intensities is performed to derive a photometric scale factor and offset to be applied to match MSX Band E intensities with MIPS $24\mu\text{m}$ intensities. The correlation is performed with bright (but not saturated) data by restricting pixel intensities to $> 500 \text{ MJy sr}^{-1}$ for the MIPS data and in the range of $[1 - 4.5] \times 10^{-5} \text{ W m}^{-2} \text{ sr}^{-1}$. The derived scale factor was $\sim 40\%$ larger than the quoted factor for converting MSX

data from $\text{W m}^{-2} \text{sr}^{-1}$ to MJy sr^{-1} . The reason for such a discrepancy is not clear, but part of the difference may be caused by the slightly different nominal wavelengths of the instruments. (3) A mask is defined to identify the saturated regions. The mask is set to 1.0 where the rescaled MSX data are brighter than 1000 MJy sr^{-1} and then ramped down to 0.0 for any pixels > 3 pixels away from these regions. (4) The mask, and 1.0 minus the mask, are then applied as weights in the linear combination of the MSX and MIPS images. Thus, in the resulting image, 99.6% of the pixels contain unmodified MIPS intensities, 0.3% of the pixels contain scaled MSX intensities, and in between 0.1% of the pixels contain a weighted average of MIPS and scaled MSX intensities. (5) Lastly, we interpolate over ~ 10 small MIPS coverage gaps that occupy 0.03% of the image.

Despite the weighted averages, differences in the PSF widths ($\sim 18.3''$ for MSX, $\sim 6''$ for MIPS) create artifacts where MSX data replace saturated MIPS point sources. Therefore, any quantitative analysis on MIPS saturated sources should be performed on the original MSX images, rather than the combined MIPS+MSX images. The combined images are useful for qualitative evaluation of the structure and color of bright extended emission, and of course, for any unsaturated emission.

2.2. MIPS Survey at $70\mu\text{m}$

In order to obtain more complete SEDs of some of the high latitude $24\mu\text{m}$ sources that show excess emission at $4.5\mu\text{m}$, we selected a total of nine such sources distributed at high Galactic latitudes within our survey. These sources were observed separately with MIPS at $70\mu\text{m}$. The low-latitude sources were not selected due their possible saturation at low latitudes in the plane. These targets were observed in MIPS photometry mode with the exposure time for each object of 3 seconds and default pixel scale of $10''$. All observations were obtained between 2007 September 21 and 23. These data were reduced using the MIPS Instrument Team’s Data Analysis Tool v. 3.06 (Gordon et al. 2007). Aperture photometry was performed utilizing a set of custom IDL scripts. The data were flux calibrated using the conversion factor of $702 \pm 35 \text{ MJy sr}^{-1}$ per raw MIPS units (5% uncertainty) following Gordon et al. (2007). An aperture of $35''$ was used, with a sky radius of $39'' - 65''$. The aperture correction for this configuration is 1.185.

2.3. Radio Surveys

Radio continuum observations at $\lambda 20\text{cm}$ surveyed the $-2^\circ < l < 5^\circ$ and $|b| < 40'$ region with a spatial resolution of $\approx 30''$ and $10''$ using two different array configurations of the Very Large Array (VLA) of the National Radio Astronomy Observatory⁹ (Yusef-Zadeh et al. 2004). Another recent survey at 20cm has extended this region to higher positive latitudes of up to 1° (Law et al.

⁹The National Radio Astronomy Observatory is a facility of the National Science Foundation, operated under a cooperative agreement by Associated Universities, Inc.

2008). We obtained 32 overlapping images at 20cm from these two surveys and convolved individual images with a Gaussian having a FWHM= $12.8'' \times 12.8''$ before the images were mosaiced.

This region has also been observed at 20 and 6cm with the VLA (Becker et al. 1994; Zoonematkermani et al. 1990). However, these surveys are short snapshot observations of a region dominated by bright sources with a wide range of angular scales and poor sensitivity and so are not useful for comparison with infrared sources due to the non-uniform uv coverage. The detection of point sources at 90 and 20cm (Nord et al. 2004; Yusef-Zadeh et al. 2004; Law et al. 2008) does suffer from the artifacts introduced by the lack of uv coverage. More recently, Lang et al. (2009) have completed a 6cm survey of the Galactic center region with a uniform uv coverage. We have used this data set to measure the fluxes of several point sources in the G359.43+0.02 cluster, as described below.

2.4. Other Surveys

A survey of Spitzer/IRAC observations of the central $2^\circ \times 1.4^\circ$ ($\sim 290 \times 210$ pc) was recently conducted in the four wavelength bands at 3.6, 4.5, 5.8 and $8\mu\text{m}$ (Stolovy et al. 2006; Ramirez et al. 2008; Arendt et al. 2008). The catalog presented in Ramirez et al. (2008) includes point source photometry from the IRAC survey and correlates those sources with previously published photometry from 2MASS at J, H, and K_s bands (Skrutskie et al. 1997).

A Submillimeter Common-User Bolometer Array (SCUBA) survey of the Galactic center covered a region of $2^\circ \times 0.5^\circ$ at 450 and $850\mu\text{m}$ with a spatial resolution of $8''$ and $15''$, respectively (Pierce-Price et al. 2000). Given the low resolution of the submillimeter data, the detected submillimeter flux is used as upper limits at $450\mu\text{m}$ and $850\mu\text{m}$ (Di Francesco et al. 2008) in the spectral energy distribution of individual point sources. However, large-scale submillimeter maps of extended sources at 450 and $850\mu\text{m}$ have been used for comparison with radio and mid-IR images.

3. Large-Scale Distribution of $24\mu\text{m}$ Emission

3.1. Extended Sources

Figure 1a shows the large scale view of the surveyed region at $24\mu\text{m}$. In order to bring out the weak sources, the sources distributed between $-1.8^\circ < l < 0.8^\circ$ are burned out in this figure. The mean brightness of this region is roughly 4 to 5 times higher than the region beyond the inner few degrees of the Galactic center. Several extended HII regions are identified to have radio continuum and submillimeter counterparts (Yusef-Zadeh et al. 2004; Pierce-Price et al. 2000). An enlarged view of the burned-out $3^\circ \times 2^\circ$ region is shown in Figure 1b. Prominent Galactic center HII complexes along the Galactic plane are associated with Sgr A – E, the Arches and the Pistol, all of which are labeled, as shown in Figure 1c. We note two extended $24\mu\text{m}$ emitting features

G0.23-0.05 and G0.31-0.07 lying between the radio Arc and Sgr B1. The radio Arc, which includes the Arches cluster and the Pistol nebula, consists of a network of nonthermal radio filaments running perpendicular to the Galactic plane (Yusef-Zadeh et al. 1984; Lang et al. 1999). We note a number of parallel filamentary features at $24\mu\text{m}$ associated with G0.31-0.07 which will be discussed elsewhere. At positive latitudes, two extended clouds known as the western and eastern Galactic center lobes are shown prominently in Figure 1b near $l \sim -0.5^\circ$ and $\sim 0.2^\circ$, respectively. The striking structure of the western lobe with its strong $24\mu\text{m}$ emission coincides with AFGL 5376 (Uchida et al. 1990). In the eastern lobe, two columns of $24\mu\text{m}$ features with an extension of about $30'$ run parallel to each other away from the Galactic plane. These features lie in the region of the Galactic center lobe that is known to emit strong synchrotron emission (Law et al. 2008). The “double-helix” nebula (Morris et al. 2006) lies along the northern extension of the eastern linear feature in the Galactic center lobe. The southern ends of these linear features appear to be pointed toward the large-scale ionized features associated with the Arches cluster G0.12+0.02 and a cluster of HII regions (H1–H5) (Yusef-Zadeh & Morris 1987; Zhao et al. 1993). In addition, there are several counterparts to foreground H α emission line nebulae, RCW 137, 141, and 142, which are prominent at $|b| > 0.2^\circ$.

At positive longitudes, a string of IRDCs is concentrated between $l \sim 0.2^\circ$ and Sgr B2 near $l=0.7^\circ$. Sub-millimeter emission from these clouds is prominent at 450 and $850\mu\text{m}$ (Lis & Carlstrom 1994; Pierce-Price et al. 2000). Figure 2a displays an enlarged view of $24\mu\text{m}$ emission from dust clouds and stellar sources distributed at positive longitudes. With careful adjustment of the overall background level, the ratio of IRAC images, such as $I(4.5)/[I(3.6)^{1.4} * I(5.8)]^{0.5}$, are used to highlight the location and structure of the IR dark clouds. This ratio is high for the IRDCs (Figure 2b). The bright feature in this figure corresponds to a dust lane that consists of a string of dust clouds. These clouds appear narrow near $l=0.25^\circ$ and become increasingly wider extending toward negative latitudes near Sgr B2. The kinematics of this dust lane have been studied in numerous molecular line surveys of this region (Oka et al. 1998; Martin et al. 2004).

At negative latitudes, the distribution of dust emission at $24\mu\text{m}$ and the ratio map are shown in Figure 3a,b, respectively. IRDCs are detected toward the well-known molecular clouds M-0.13-0.08 (20 km s^{-1}) and M-0.02-0.07 (50 km s^{-1}) (Herrnstein & Ho 2005; Armstrong & Barrett 1985). Both clouds are located near the Galactic center. One of the largest structures in the ratio map is the pair of two dust lanes that run parallel to each other along the Galactic plane between $l=0^\circ$ and $l=-40'$ on the positive and negative latitudes. The previous CS (1-0) line study of this region has shown the counterpart to the positive latitude dust lane to have a coherent kinematic structure. We also note an elongated dust cloud (called “Vertical IRDC” in Fig. 1c) running toward positive latitudes at $l=-40'$, $b=4'$ with a latitude extent of $12'$. The prominence of this feature with respect to the dust lanes in the ratio map suggests that it is a foreground cloud.

3.2. Color Distribution of Extended Emission

In order to analyze the color distribution at different bands, a close-up view of the central region of the $24\mu\text{m}$ survey is cropped to the exact size of the $8\mu\text{m}$ survey (Stolovy et al. 2006). Figure 4a shows the combined 24, 8 and $4.5\mu\text{m}$ images with red, green and blue colors, respectively. Figure 4b shows only the 3.6, 4.5, and $8\mu\text{m}$ images in blue, green and red colors, respectively. Overall, there is a great deal of non-uniformity in the color distribution detected between IRAC and MIPS images, as shown in Figure 4a. In contrast, uniform color distribution is noted in IRAC images, as shown in Figure 4b (Arendt et al. 2008). One of the main reasons for the non-uniformity of colors is that $24\mu\text{m}$ emission is an excellent diagnostic of local sources of heating of large dust grains. This is in part due to the fact that thermal emission from large dust grains at $24\mu\text{m}$ becomes significantly enhanced when the radiation field is only 100 times that of the local interstellar radiation field (ISRF) in the solar vicinity (Arendt et al. 2008). In contrast, $8\mu\text{m}$ emission mainly arises from aromatics (hereafter PAHs) that are excited by the interstellar radiation field and nearby OB stars. Thermal emission from small dust grains becomes strong enough to compete with the PAH emission in the $8\mu\text{m}$ band only when the local radiation field is about 10^4 times that of the solar neighborhood (Li & Draine 2001). Thus, there is much less variation in the $8\mu\text{m}$ to $5.8\mu\text{m}$ color than in the $24\mu\text{m}$ to $8\mu\text{m}$ color. These color distribution images based on IRAC and MIPS data place a lower limit of ~ 100 times the ISRF throughout the Galactic center region with the exception of the regions known to have a very strong radiation field such as the Arches and Sgr A (see Arendt et al. 2008).

Several extended sources show a distinct pattern of excess $24\mu\text{m}$ emission (red in Fig. 4a) surrounded by $8\mu\text{m}$ emission (green and yellow in Fig. 4a). The $24\mu\text{m}$ excess (or $8\mu\text{m}$ deficit) can be accounted for by the destruction of PAHs by local sources of UV radiation or shocks (Watson et al. 2008; Churchwell et al. 2007; Povich et al. 2007). In contrast to small grains and PAHs that can be destroyed, the large dust grains re-radiate the absorbed UV radiation at long wavelengths, $24\mu\text{m}$. The most striking example that shows these effects is the optical $\text{H}\alpha$ line emission nebulae RCW 137, 141 and 142 which are foreground sources and are internally heated. PAHs are destroyed close to the source of heating, but are excited at the edge of the cloud by the external ISM radiation field. The $24\mu\text{m}$ diffuse emission along the Galactic plane traces local sources of heating by HII regions.

There is another type of $24\mu\text{m}$ source that shows neither $8\mu\text{m}$ counterpart nor any evidence for embedded sources of heating. AFGL 5376 (Uchida et al. 1990) is one example that is located at high latitudes. G0.85-0.44 is another source that shows similar characteristics. Alternative mechanisms must be responsible for heating these clouds. One candidate is the high flux of cosmic rays that could be responsible for heating large dust grains but not PAHs.

3.3. Infrared Dark Clouds

We note several IRDCs in Figure 4a with different levels of darkness. These cold, dark clouds are seen in absorption against the diffuse background emission. The IRDCs are optically thick even at $24\mu\text{m}$. Therefore, their apparent surface brightnesses are more of an indication of the emitting column density on the line of sight to the cloud (i.e., the cloud’s distance) than a sign of the optical depth of the IRDCs. For example, we note that the IRDCs at high and low Galactic plane latitudes, such as G0.2+0.47 and G-0.67+0.18 are the darkest clouds, suggesting that they are distributed locally along the line of sight.

As was shown in the ratio maps, the large scale distribution of IRDCs forming a dust lane implies an early phase of massive star or star cluster formation in the Galactic center region. IRDCs are dense ($> 10^5 \text{ cm}^{-3}$), cold ($< 25\text{K}$) and attain high column densities (10^{23} cm^{-2}) in the Galactic disk (Egan et al. 1998; Carey et al. 2000; Simon et al. 2006). The extreme physical properties of the clouds in the Galactic center region should be even more suitable for young, massive star cluster formation. We note the string of IRDCs is coincident with the “Dust Ridge” (Lis et al. 2001), as shown in Figure 1c. What is remarkable is a large-scale east-west ridge of IRDCs tracing dense molecular gas between G0.25+0.01 and Sgr B2. This continuous east-west IRDC ridge shows a sinusoidal appearance on a scale of $\sim 5'$ corresponding to 12 pc. The western half of this large-scale ridge of IRDCs is quiescent (Lis et al. 2001) in its star formation activity whereas the eastern half shows spectacular on-going star formation. The string of submillimeter emitting molecular clouds includes G0.25+0.01 and the Sgr B complex and is darker than the well-known 20 and 50 km s^{-1} molecular clouds M-0.13-0.08 and M-0.02-0.07 as well as clouds in the negative longitude side of the Galactic center. This behavior suggests that the positive-longitude IRDCs are closer than the 20 and 50 km s^{-1} and Sgr C clouds. The large-scale distribution of IRDCs traces coherent molecular lanes running parallel to the nuclear disk (Bania 1977; Bally et al. 1988; Oka et al. 2005; Tsuboi et al. 1999; Martin et al. 2004), as shown in ratio maps of Figures 2 and 3. The color contrast of the coherent, large scale dust lane suggests that the molecular gas in the central molecular zone is oriented in the same direction as that of the well-known stellar bar (Binney et al. 1991; Stark et al. 1991).

3.4. Distribution of Compact Sources

The blue color ($4.5\mu\text{m}$ emission) in Figure 4a represents the stellar density distribution in Sgr A where the evolved stellar core of the bulge peaks. This is mostly unresolved stellar sources, not intrinsically diffuse emission. A number of red ($24\mu\text{m}$) point sources are also seen in this figure that appear to be embedded within IRDCs suggesting that they are protostellar candidates, as will be discussed in section 5. The red color reveals embedded stellar sources that heat surrounding dust grains to high temperatures. Numerous compact HII regions with radio continuum counterparts are distributed along the Galactic plane near the Galactic center.

To reveal the distribution of intrinsically red compact sources against the strong extended emission, we constructed a $24\mu\text{m}$ to $8\mu\text{m}$ intensity ratio image, which is presented in Figure 5a. Regions with relatively strong $24\mu\text{m}$ emission are light whereas regions with strong $8\mu\text{m}$ (PAH) emission are dark. Most of the emission from the ISM (including that on the line of sight to IRDCs) disappears into a flat gray background. The disappearance of IRDCs is because they are opaque at both $8\mu\text{m}$ and $24\mu\text{m}$. The extinction ratio ($A_{8\mu\text{m}}/A_{24\mu\text{m}} \sim 1$) (Li & Draine 2001) implies a lack of reddening even for clouds that are not opaque (e.g., their edges). The “removal” of the typical ISM emission and dark clouds accentuates a number of structures and helps reveal some fainter, compact and extended sources with excess $24\mu\text{m}$ emission. The most striking feature in the ratio map is the distribution of compact emission from a high concentration of strong IR-excess objects, candidate YSOs or UCHII regions distributed between $l = 0^\circ$ and $l = -1.2^\circ$.

Figure 5b shows the relationship between the compact $24\mu\text{m}$ point sources and the molecular gas. It is a composite image indicating $24\mu\text{m}$ in green and $450\mu\text{m}$ in red. Sub-millimetre emission at $450\mu\text{m}$ is optically thin and is known to be an excellent tracer of molecular gas distributed in the central molecular zone. The comparison of the distribution of $24\mu\text{m}$ emission and the ratio map shows two features. One is the distribution of extended sub-millimetre emission being strongest in the positive longitude side the Galactic center. It is clear that molecular gas distribution at $l > 0^\circ$ is more uniform and more intense at $450\mu\text{m}$ than that at negative longitudes. Similar asymmetric structure is also noted in CS and CO line observations (Bally et al. 1988; Martin et al. 2004; Oka et al. 2005; Tsuboi et al. 1999). This asymmetric distribution shows 2/3 of the mass of molecular gas on the positive longitude side of the Galactic center region (Bally et al. 1988; Oka et al. 2005; Martin et al. 2004). The presence of such an asymmetry is mainly due to massive clouds associated with Sgr B2 and the dust ridge and a lack of massive, dense clouds at $l < 0^\circ$ with the exception of Sgr C.

The second feature is the distribution of $450\mu\text{m}$ emission at negative longitudes showing that $24\mu\text{m}$ sources anti-correlate with the distribution of dust clouds. Remarkably, the distribution of $24\mu\text{m}$ point sources appears to be sandwiched by two layers of dust and gas clouds running parallel to the Galactic plane and symmetrically distributed with respect to the Galactic center. The “bow-tie” dust layers, as schematically drawn in Figure 1c, stretch along both positive and negative longitudes and coincide with IRDCs at $8\mu\text{m}$ and $24\mu\text{m}$. Submillimeter emission is also noted from a cloud at negative latitudes $b = -5'$. This feature is the negative latitude counterpart to the layer of submillimeter emitting cloud in the region between G0.25+0.01 and Sgr B1 at positive longitudes. The negative latitude submillimeter layer does not have an IRDC counterpart, implying that it is most likely located on the far side of Sgr B2. Thus, it is likely that these molecular layers are closer to us at positive longitudes than at negative ones. What is remarkable from the mid-IR and submillimeter images are that the “bow-tie” structure in fact consists of two layers of molecular and dust clouds that are symmetrically distributed with respect to the Galactic center. However, it is most likely that the positive longitude side of these molecular layers is closer to us than those at negative latitudes.

We also note that unlike the gas and dust distributions, the $24\mu\text{m}$ point sources are more uniformly distributed on the negative longitudes than at positive ones. Given that the chain of IRDCs that include Sgr B2 are thought to be closer than those at negative longitude, it could be that they hide a distant population of $24\mu\text{m}$ sources and create an apparent asymmetry, as discussed in more detail below.

4. Candidate YSOs

To investigate the nature of the $24\mu\text{m}$ compact sources, $8\text{--}24\mu\text{m}$ ($[8]\text{--}[24]\mu\text{m}$) color magnitude diagrams (CMDs) are constructed for sources within $|b| = 10'$ and $|l|=1.4$ degrees, corresponding to the central 0.4×0.05 kpc region. The CMD of these sources identified in the positive and negative longitudes is shown in Figure 6. These data used the MIPS catalog at $24\mu\text{m}$ (Hinz et al. 2009) and IRAC catalog at $8\mu\text{m}$ (Ramirez et al. 2008). A total of 172,670 sources is detected, 70,794 and 101,876 of which are found in the region restricted to positive and negative longitudes, respectively. There is an excess of 31082 sources identified in negative longitudes. This asymmetry could be explained by the high extinction experienced by mid-IR sources in the region where dense molecular clouds are highly concentrated. Alternatively, the distribution of compact dusty sources could be due to an intrinsic excess of YSOs or evolved AGB stars. The dashed line in Figure 6 is chosen empirically, as discussed below, to separate the reddest YSOs from AGBs. Each of the two possibilities is discussed below.

OH/IR stars are oxygen-rich, mass-losing cool giants that represent evolved AGB stars at the end of their lives (Habing 1996). These post AGB stars are known to be dusty with excess emission at infrared wavelengths. YSOs are also known to have excess emission in infrared wavelengths and are characterized by dusty envelopes and disks that absorb the radiation from the central protostar (Whitney et al. 2003a; Adams et al. 1987). To explore the color of evolved stars in the Galactic center, we examined the spatial distribution of known OH/IR stars in the region shown in Figure 6 using the OH 1612 MHz catalogs (Lindqvist et al. 1992; Sevenster et al. 1997a,b; Sjouwerman et al. 1998). OH/IR surveys are not affected by visual extinction. These surveys have uniformly sampled the region covered by IRAC observations. The shallow but uniformly sampled survey by Sevenster et al. (1997a) finds a total of 7 and 9 OH/IR stars in the restricted region, for positive and negative longitudes, respectively. Similarly, the spatial distribution of OH/IR stars on a large scale is symmetric with respect to the Galactic center. Although, there are not many OH/IR masers that we found to have infrared counterparts in the restricted region of our survey, we find no evidence of asymmetry in the distribution of OH/IR stars with respect to the Galactic center.

To examine whether the observed color of the infrared sources (Ortiz et al. 2002; Ojha et al. 2007) can be due to the excess of YSOs, we first identify the color of OH/IR stars. The reddening toward these Galactic center sources is minimally affected by the differential extinction between 8 and $24\mu\text{m}$. Flaherty et al. (2007) have recently derived $A(8\mu\text{m}) - A(24\mu\text{m}) \sim 0.0 \pm 0.05 \times A(K)$. The color variation between 8 and $24\mu\text{m}$ should be < 0.2 mag assuming $A(K) \sim 3.2$ or ~ 30 magnitudes

of visual extinction. Thus, the observed color of the sources is intrinsic. Here, we make an empirical assumption that the very red sources are likely to be candidate YSOs. Figure 7a shows the CMD of all the $24\mu\text{m}$ sources found in the surveyed region by IRAC. The colors of OH/IR stars that are found using the survey by Sevenster et al. (1997a) are shown as triangles in Figure 7a and are distributed to the left of the dashed line that was selected empirically. The color of OH/IR masers is clearly distinguished from the reddest and faintest sources (by a few magnitudes). The dashed line in Figure 7a is the slope that separates most of the YSO candidates to the right from the rest of the sources that have 24 and $8\mu\text{m}$ counterparts. The left side of the slope in Figure 7a indicates a trend of IR excess sources with luminosity. The CMD of the LMC shows a similar trend among luminous AGB stars due to the relationship between increasing radiation pressure resulting in more mass loss in dust, and therefore more IR excess (see Fig. 3a of Whitney et al. 2008). Thus, we believe the sources to the right of the slope in Figure 7a are dominated by candidate YSOs. The color-color diagram between $[8]-[24]\mu\text{m}$ is also shown in Figure 7b where the candidate YSOs are shown as crosses. In the restricted $l = \pm 1.4^\circ$, $b = \pm 10'$ region the total number of YSO candidates is found to be 347 and 212 distributed on the negative and positive longitudes, respectively. The spatial distribution of candidate YSOs with $[8]-[24]$ greater than 4 is shown in Figure 7c revealing that the reddest infrared sources are distributed mostly along the Galactic plane. The numbers of YSO candidates are lower limits because the colors of stars in the saturated regions near $l \sim 0^\circ$ and $l \sim 0.2^\circ$ could not be examined (see Figure 7c). In spite of these restrictions, we note that most of the candidate YSOs are distributed in the negative latitudes, very close to the Galactic equator.

The saturated sources at $24\mu\text{m}$ as well as the contaminating sources limit our ability to address the issue of completeness. However, we believe that the distribution of OH/IR sources validates our empirical choice for the slope of the dashed line used to identify most of the YSO candidates. An additional step is taken in §5.3 to identify the fraction of YSO candidates via SED fitting of the sources selected from the right region of the CMD of Figure 7. As discussed below, $\sim 60\text{-}65\%$ of the total number of sources from the CMDs are SED fitted. Ultimately, future spectroscopic measurements of YSO candidates should be able to address the completeness issue.

4.1. Excess Candidate YSOs in $l < 0^\circ$?

To test the possibility that there is an asymmetric distribution of candidate YSOs with respect to the Galactic center, we examined two tracers that are not affected by visual extinction. First, we examined compact radio continuum sources (Yusef-Zadeh et al. 2004) and found 44 and 58 sources in the positive and negative longitude sides of the Galactic center, restricted to the same regions where candidate YSOs are found. It is known that Sgr B2 is one of the most active star-forming sites in the Galaxy at $l \sim 0.7^\circ$ (Mehring et al. 1998; De Pree et al. 2005). We note that 16 of the 44 compact radio sources at the positive longitudes arise only from ultracompact HII regions in Sgr B2. On the other hand, compact radio continuum sources in the $l < 0^\circ$ region are distributed more uniformly than in the region at $l > 0$ degrees. The excess number of 14 sources at

negative longitudes combined with non-uniform distribution of compact radio continuum sources at positive longitudes imply an asymmetry of radio continuum sources that can not be explained by excess extinction at positive latitudes. This is consistent with the excess of infrared sources in the negative longitudes of the Galactic center. Additional support for this picture comes from H₂O maser study of the same region showing a similar distribution to that of compact 20cm radio continuum sources. This survey used the *Infrared Astronomical Satellite* (IRAS) Galactic center catalog (Taylor et al. 1993) to search for H₂ masers. The largest concentration of star forming water masers is found in Sgr B2 whereas the star forming H₂O masers are populated uniformly in the negative longitude sides of the Galactic center (Taylor et al. 1993). For example, the targeted survey by Taylor et al. which excluded the Sgr B2 region, detected a total of 13 and one star forming H₂O masers at the negative and positive longitudes, respectively. Although water maser survey observations have not uniformly sampled the Galactic center region, the available data are consistent with the picture that the largest concentration of quiescent molecular clouds such as the string of IRDCs distributed in $l > 0^\circ$ do not have a high density of 24 μ m sources, H₂O masers and ultracompact radio continuum sources (Lis & Carlstrom 1994).

Since most of the candidate YSOs are distributed asymmetrically on the negative longitude side of the Galactic center, we constructed another histogram of candidate YSOs for $l < 0^\circ$. This histogram should be a better representation of the scale height of the uniformly distributed YSO candidates. Gaussian fits to the narrow and broad components give FWHM $\sim 5.17' \pm 0.2'$ centered at $b = -2.4'$ and FWHM $\sim 28.6' \pm 2'$ centered at $b = -0.02'$, respectively. The scale height of the YSO candidates in $l < 0^\circ$ is $h \sim 6.3$ pc is similar to $h \sim 7$ pc when all the sources at both positive and negative longitudes are included.

4.2. Distribution of 24 μ m Sources

To examine the distribution of YSO candidates as a function of latitude, a histogram was made using the data from the central $2.6^\circ \times 2^\circ (l \times b)$. Figure 8a shows a broad and narrow component. The broad and narrow components are fitted with two Gaussians. The broad component is centered near $b \sim 0'$ with a FWHM $= 64.9' \pm 2'$ whereas the narrow component is displaced with respect to the Galactic plane at $b = -3'$ with a FWHM $\sim 5.6' \pm 0.2'$. Figure 8b shows the distribution of the candidate YSOs when they are restricted to $|b| < 10'$. This distribution is consistent with the narrow latitude distribution of YSO candidates with an offset with respect to the Galactic equator near $b = -2.4'$. This value is likely to be close to the true latitude of the Galactic plane since Sgr A*, the massive black hole at the Galactic center, lies at $b = -2.8'$. Unlike the broad distribution that is likely due to foreground sources toward the Galactic center, the narrow distribution of the candidate YSOs suggests a uniform sample of sources located along the midplane of the Galactic center. The scale height of the candidate YSOs is estimated to be $h \sim 7$ pc assuming the distance to the Galactic center is 8.5 kpc. Molecular line observations of this region based on CS (1-0) transition also finds a narrow scale height $h \sim 10$ pc (Bally et al. 1988). The narrow scale height of

both candidate YSOs and molecular clouds can be used as a support for the association of infrared sources and the disk population of molecular gas distributed in the Galactic center region. To test that the reddest sources belong to a population of YSOs distributed in the midplane of the Galactic center region, the YSO candidates from the color-magnitude diagrams of Figures 6 and 7 are presented in two dimensional histograms in Figures 8c and 8d to emphasize the higher fraction of brighter, redder YSO candidates within $|b| < 10'$ and the exterior region $|b| > 10'$, respectively. These CMDs are selected from the point source catalogs. The fraction of redder YSO candidates with $[8]-[24] > 3$, relative to the total number of sources in the inner $10'$ is found to be a factor of five to ten higher than the region beyond the inner $10'$. This suggests that there are more red YSOs in proportion to the total YSOs detected for the innermost region of the Galactic center than those found in the outermost region. There are 1720 YSO candidates, 599 of which are in the region restricted to $-1.4^\circ < l < 1.4^\circ$ and $-10' < b < 10'$; there are 347 and 252 sources distributed in the negative and positive longitudes, respectively.

To compare the scale heights of candidate YSOs and the bright $24\mu\text{m}$ point sources, we constructed Figure 9a which shows the distribution of bright unsaturated $24\mu\text{m}$ sources between 0 and 5 magnitudes as a function of latitude within $|l| < 1.3^\circ$. The narrow and wide components reflect the scale height of all bright stars which include both the evolved dusty stars and YSO candidates. The fitted values give two components with $\text{FWM} \sim 15'$ and $96'$, both of which are broader than those of the candidate YSO's. To measure the scale height of the bright dusty stars without being contaminated by the YSO candidates, we subtracted the candidate YSOs and determined the latitude distribution of dusty sources. Two components were fitted with $\text{FWHM} \sim 16.2' \pm 0.3'$ and $105' \pm 3'$. The scale height of the narrow and bright component corresponds to a value of ~ 20 pc. The higher values of the scale heights of bright dusty sources compared to YSO candidates suggest they are more evolved dynamically than the YSOs. An important implication of these scale heights is the support for a new population of YSOs distributed in the Galactic center region.

Using the mosaic image based on the combined MSX and MIPS data, we also constructed the brightness distribution of $24\mu\text{m}$ emission as a function of latitude and longitude. Figure 9b shows the latitude distribution where two broad and narrow components are detected. The broad background emission is subtracted followed by a Gaussian fit to the narrow component, giving a $\text{FWHM} \sim 8'$ which corresponds to a scale height of ~ 10 pc. This value is slightly thicker than the scale height of candidate YSOs having $h = 7$ pc but close to the scale height of molecular gas $h=10$ pc. The fit to the broad component gives $\text{FWHM}=61'$, representing the scale height of bright sources in the disk distributed along the line of sight.

To examine the brightness distribution of point sources for a given flux, we plot the brightness distribution of $24\mu\text{m}$ sources as a function of longitude and present the results in three different panels in Figure 10. The flux of selected YSO candidates range between 0-5, 5-7 and 7-10 magnitudes corresponding to bright, intermediate and faint sources in the entire region of the $24\mu\text{m}$ survey but restricted only to within $b = \pm 10'$. Such a tight latitude restriction most likely selects the sources that populate the Galactic plane. It is clear that the brightest $24\mu\text{m}$ sources show a

stronger asymmetry in longitude, as shown in Figure 10a, when compared to the distribution of fainter sources, as shown in Figure 10b,c. The faintest stars dominate at greater longitudes but are not detected in the innermost region of the Galactic center. This is because of the confusion and the saturation caused by the extremely strong background. These distributions indicate that the brightest $24\mu\text{m}$ point sources exhibit an excess at negative longitudes similar to that seen in the candidate YSOs. The fainter $24\mu\text{m}$ sources seem to be uniformly distributed.

5. The SEDs of candidate YSOs

One of the difficulties in identifying YSOs by selecting them from 8– $24\mu\text{m}$ color magnitude diagrams is the contamination by dusty and bright AGB stars. In addition, YSOs can populate left of the CMD line as well (as seen in Figs. 6 & 7). In order to have more confidence in identifying YSO candidates and to characterize their properties, we obtained the Spectral Energy Distributions (SEDs) of selected number of YSO candidates using measurements at eight wavelengths from $1.24\mu\text{m}$ to $24\mu\text{m}$ in order to determine the evolutionary phases. The SED fitting technique is motivated by physical models and determines the physical properties of the sources. This technique is used for further refinement of the list of YSO candidates based on the CMD technique with its ad hoc distinctions in color. The SEDs of the sources are analyzed by comparing to a set of SEDs produced by a large grid of YSO models (Robitaille et al. 2006; Whitney et al. 2003b,a). We use a linear regression fitter (Robitaille et al. 2007) to find all SEDs from the grid of models that are fit within a specified χ^2 range to the data. The χ^2 of the fit depends on the errors assumed for the data. We set lower limits on the fractional flux error (dF/F) to be 20% to account for variability between the 2MASS, IRAC and MIPS observation dates. The minimum reduced χ^2 for each source is determined. For all the models with a reduced χ^2 within 1 of the minimum value, physical parameters corresponding to those models are averaged along with their standard deviations. The models are not always well-constrained due to the incomplete SED information (many lower and upper limits and relatively few overall data points). However, this averaging is constrained by the finite extent of the grid of models.

We carried out our search for candidate YSOs toward two regions, using SED fitting of sources selected from CMDs. One is a small cluster of $24\mu\text{m}$ sources at G359.43+0.02 and the other is the candidate YSOs distributed within $|b| = 10'$ and $|l| = 1.3^0$. We caution that the CMD selection biases us to redder sources. In addition, we have employed conservative errors in the SED fitting. Robitaille et al. (2006) defined three evolutionary stages based on their derived model properties, analogous to the classification based on the observed SED slope (Lada 1987): Stage I objects have envelope infall rate $\dot{M}_{\text{env}}/M_{\star} > 10^{-6} \text{ yr}^{-1}$, Stage II objects have $\dot{M}_{\text{env}}/M_{\star} < 10^{-6} \text{ yr}^{-1}$ and $M_{\text{disk}}/M_{\star} > 10^{-6}$, and Stage III objects have $\dot{M}_{\text{env}}/M_{\star} < 10^{-6} \text{ yr}^{-1}$ and $M_{\text{disk}}/M_{\star} < 10^{-6}$. That is, Stage I objects are young protostars embedded in an opaque infalling envelope. In Stage II objects the envelope has mostly dispersed, and the central star is surrounded by an opaque disk. In Stage III the disk is optically thin. It is not clear if there is a long-lived disk stage (Stage II)

in high-mass sources, or if the disk is dispersed with the envelope. There are good reasons for the conservative (20%) error bars, but it means that Stage II and III YSOs with smaller IR excesses may fail to be distinguished from reddened stellar atmospheres. It is clear that the YSO list will be incomplete and biased towards younger evolutionary stages, which are readily distinguishable from even dusty evolved stars. We discuss these two groups separately below and then estimate the star formation rate.

5.1. G359.43+0.02 Cluster

A striking cluster of $24\mu\text{m}$ sources lies about $8'$ north of the Sgr C complex G359.4-0.1 with its thermal and nonthermal radio continuum components. Figure 11a,b show grayscale images of G359.43+0.02 at $24\mu\text{m}$ and 20cm, respectively. This cluster of $24\mu\text{m}$ source (G359.43+0.02) is distributed in the region where the northern extension of the nonthermal radio filament of Sgr C dominates the radio continuum emission. In spite of strong extended background emission from the nonthermal filaments, there are several compact radio sources that are detected toward this cluster. The positions, the flux densities at 20 and 6cm and the sizes of individual radio sources are listed in Table 1; column 1 identifies the source number, columns 2 and 3 show the Galactic coordinates, and columns 4 to 7 give the flux densities in mJy and the source sizes at 6 and 20cm, respectively. These values are estimated by two-dimensional Gaussian fits to individual compact radio sources at 6 and 20cm. The finding chart for the radio and $24\mu\text{m}$ sources is shown in Figure 11c. The crosses drawn on Figure 11a,c show the positions of radio continuum point sources whereas the circles drawn on Figure 11b,c show the position of compact $24\mu\text{m}$ sources. Because of the saturation of several $24\mu\text{m}$ sources in this cluster, there are only two radio sources, as listed in Table 1, that have cataloged $24\mu\text{m}$ counterparts.

The CMD covered by the region shown in Figure 11a,b is shown in Figure 11d. A total of 28 candidate YSOs is detected in the YSO candidate region of Figure 11d. We selected these candidate YSOs and fitted their SEDs. The SED fitting leads to the rejection of 10 sources as YSO candidates. Thus the total number of YSO fitted sources is about 64% of the sources that are selected from CMDs. The fraction of Stage I objects is 78% of the total number of SED fitted sources.

The rejected sources are likely to be evolved stellar sources, for which the model YSO SEDs give poor fits. Other reasons for rejecting sources could be i) variability between IRAC and MIPS, ii) errors in photometry, iii) source confusion where multiple sources contribute and give an SED that is not well fit by a single YSO model, iv) bad extraction of data or v) there are no correct models in the grid.

Figure 12a shows the fitted SEDs for each individual YSO candidate source and Table 2 shows the physical characteristics derived from their SED fitting. These sources are assumed to be 8.5 kpc away with A_v values ranging between 5 and 50 magnitudes. Given that 9 out of 18 of these have

fewer than 5 data points, we note from Figure 12a that the flux of most cluster members is elevated at $24\mu\text{m}$ when compared to IRAC and 2MASS data points. This supports the identification of these sources as YSOs. The parameters of the fits to these 18 sources suggest that the masses of the individual protostars range between 5 and $11.7 M_{\odot}$ with corresponding luminosities ranging between 6.5×10^2 and $10^4 L_{\odot}$.

Columns 1-10 of Tables 2, 3 and 4 show (1) the the SST (Spitzer Space Telescope) Galactic center (GC) number based on the IRAC catalogs (Ramirez et al. 2008), (2-3) Galactic coordinates, (4) χ^2 values, (5) number of acceptably fitting models “nfits”, (6) the visual extinction A_v , (7-8) the average mass and luminosity of the protostar, (9) the average mass accretion rate which includes their corresponding standard deviations, and (10) the evolutionary stage of the fitted sources. The error bars are 1σ standard deviations of the well-fit values. The standard deviation of the fitted values reflect the limited number of data points that went into a fit. Thus, additional data points in other wavelength bands should improve the reliability in a fit. We examined χ^2 with values ranging between 0.5 to 2. There were many fits that did not go through the data points when a value of 2 was selected. On the other hand, when we used a value of 0.5, there were not enough fits. Thus, we visually selected fits with $\chi^2 \sim 1$. A_v values ranging between 5 and 50 magnitudes. A_v restriction is unlikely to bias the results. It is restricting some of the less likely models from being included in the fitting. For example, if the A_v to a source is 10, and the fitter finds a model with $A_v=0$, it is going to find a more embedded model than it should in order to fit the high extinction. By selecting a reasonable range of A_v , we are getting more appropriate YSO models to fit the source.

5.2. Sources within $|b| = 10'$

The number of candidate YSOs, as shown to the right in the CMDs of Figure 7a is 347 and 212 distributed at negative and positive longitudes, respectively. These numbers are obviously lower limits due to the bright saturated background at $24\mu\text{m}$. SED fitting showed a total of 213, 112 and 35 for Stage I, II, and III sources. We note that $\sim 60\%$ of YSO candidates are identified as Stage I sources. When grouped by longitude, the total numbers of Stage I, II, and III sources are 131, 69, 23 at $l < 0^\circ$ whereas 82, 43, 12 sources are distributed at $l > 0^\circ$, respectively. The total number of acceptable sources that are SED fitted within the restricted region is 360. This number is $\sim 64\%$ of the total number of sources that are selected from CMDs. A similar fraction of SED fitted stars is found in the G359.43+0.02 cluster. The total fraction of the SED fitted YSOs in Stage I is $\sim 60\%$. Assuming that these sources are within the central region and hence located at distances of 7.5 and 8.5 kpc, Tables 3 and 4 list the physical parameters of individual sources distributed at negative and positive longitudes, respectively.

5.3. Star Formation Rate

5.3.1. G359.43+0.02 Cluster

We now estimate the star formation rate (SFR) from the sum of average masses and luminosities derived from fitting of the SEDs of the YSOs. We first determine the SFR in the G359.43+0.02 cluster which is a subset of the detected YSOs found throughout the nuclear disk. The characteristics of this cluster are described in §5.1. The total stellar mass in the cluster is estimated to be $\sim 148 M_{\odot}$. Assuming a distance ~ 8.5 kpc, SED fitting to a sample of 18 sources yields masses ranging from 8 to $20 M_{\odot}$ and classifies 14 candidates in Stage I, three in Stage II and one in Stage III. This result suggests that the majority (nominally 78%) are Stage I YSOs, which have stellar ages $\sim 10^5$ years and masses in excess of $8 M_{\odot}$. The canonical age for a Class I source for low-mass stars is thought to be $1\text{--}5 \times 10^5$ years. This is based on the ratio of number of Class I to Class II sources in nearby star forming regions. The ages of the Class II sources are known from their stellar parameters (temperature, radius) and PMS stellar evolutionary tracks, so a combination of theory and observations. and Class 0 sources are estimated to be $\sim 10^4$ yrs, from ratio of the numbers and dynamical timescales of their outflows. For higher mass stars which presumably form much faster, we believe 10^5 years for a Stage I source is reasonable (Lada 1999; Beuther et al. 2007).

To compute the total cluster mass of only Stage I YSOs, we adopt a standard broken power-law form of the IMF (Whitney et al. 2008; Kroupa 2001), with the number of stars per unit mass scaling as $M^{-1.3}$ between 0.08 and $0.5 M_{\odot}$ and as $M^{-2.3}$ between $0.5 M_{\odot}$ and $50 M_{\odot}$ (designated the Kroupa IMF hereafter). Figure 12b shows the broken power-law form, as a dashed line, which is normalized to pass through the peak in the histogram of the stellar mass distribution derived from SED fitting of the YSOs in the G359.43+0.02 cluster. The stellar mass associated with the Stage I YSOs in this cluster is $\sim 1400 M_{\odot}$.

The lack of observed high mass stars is most likely due to saturated sources and confusion. Another possibility is that the SED models of massive stars with a large inner hole in the surrounding material were not included in the grid, and thus are not represented in this study. Lastly, most massive stars embedded in the dense molecular material, which is on average 10^2 higher than that in the Galactic disk, may evolve rapidly. The residence time of an expanding remnant in dense molecular clouds such as found in the Galactic center is unknown. Numerical simulations are needed to examine whether the evolution of supernova remnants give shorter residence time in high density medium than in low density medium (Tilley et al. 2006). This may be relevant to the fact that the Galactic center region is known to host a high cosmic ray flux (Law et al. 2008). The advantage of using only Stage I YSOs is that the average lifetime of these sources is better constrained than when all YSOs are included. Assuming that the typical age of Stage I YSOs is 10^5 years, the SFR in this cluster is $\sim 1.4 \times 10^{-2} M_{\odot} \text{ yr}^{-1}$.

5.3.2. Nuclear Disk

SFR Using YSO Candidates

We now estimate the SFR in the nuclear disk restricted to a region between $|l| < 1.3^\circ$ and $|b| < 10'$. The characteristics of the YSOs are described in §5.2. The stellar mass associated with only Stage I YSOs gives a total mass of $\sim 1.4 \times 10^4 M_\odot$. The star formation rate is estimated to be $\sim 0.14 M_\odot \text{yr}^{-1}$. Figure 12c shows the histogram of the mass distribution for both longitudes as well as the broken power law of the chosen IMF. SFRs for YSOs at negative and positive longitudes are estimated to be 0.1 and $0.05 M_\odot \text{yr}^{-1}$, respectively. The SED fitting of YSOs confirms a 10^5 year duration of star formation because the number of Stage I YSO candidates dominates over Stage II and III YSOs. This implies an asymmetric star formation rate with respect to the Galactic center. The cause of this asymmetry could be due to a short-lived random event causing a lop-sided star formation rate or it might be due to a more stable structure, possibly related to the bar.

The mass of molecular gas in the central region allows us to determine the star formation rate per unit mass and compare it with the efficiency of star formation elsewhere in the Galaxy. The observed anti-correlation of molecular clouds and the population of YSO candidates suggest that molecular clouds have already been consumed in the formation of YSOs. If we make an assumption that a fraction of the molecular mass presently distributed in the central region has gone into formation of YSO candidates, and adopt an initial molecular gas mass of $10^6 - 10^7 M_\odot$, then the star formation efficiency is estimated to be $\times 10^{-7} - 10^{-8} \text{yr}^{-1}$. The total mass of molecular gas is estimated to be $\sim 5 \times 10^7 M_\odot$ (Pierce-Price et al. 2000). The estimated star formation efficiency of the Galactic disk is $5 \times 10^{-9} \text{yr}^{-1}$ (Güsten & Philipp 2004). The dominance of Stage I YSO candidates relative to Stage II suggests that a burst of star formation must have occurred $\sim 10^5$ years ago, consistent with our estimate above being higher than the average star formation efficiency. The global properties of interstellar and stellar components of the Galactic center region also suggest star formation occurs in burst (Tutukov & Kruegel 1978; Loose et al. 1982).

SFR Using Thermal Radio Measurements

If the candidate YSOs are massive and are sufficiently evolved, they are likely to produce HII regions that can be detected at radio wavelengths if their spectral type is earlier than B3 stars (Felli et al. 2000). To examine further the nature of infrared sources that have radio continuum counterparts, the masses inferred from radio data are compared with those inferred from SED fitting. Assuming the fluxes given in Table 1 are HII regions and are produced by optically thin bremsstrahlung radiation, then we can estimate the lower limit to the number of ionizing photons to sustain the ionization. As given by (Condon 1992),

$$N_{Ly} = 6.3 \times 10^{52} s^{-1} (T_e/10^4)^{-0.45} \times (\nu/GHz)^{0.1} (L_{thermal}/10^{27} \text{ergs}^{-1} \text{Hz}^{-1})$$

where T_e is the electron temperature, ν is the observed frequency and $L_{thermal}$ is the observed luminosity. The number of Lyman continuum photons per second calculated from 5 GHz data for radio sources 5 and 6 in Table 1 are 3.6 and 3.4 mJy corresponding to $N_{Ly} \sim 1.5 \times 10^{46}$. These rates are consistent with B2 ZAMS stars (Vacca et al. 1996; Panagia 1973). The average masses estimated from SED fitting for sources 5 and 6 are 8.8 and 9.6 M_\odot , respectively. The discrepancy between the inferred mass from free-free continuum flux and from SED fitting may come from the fact these YSOs are more evolved and SED modeling is not accounting for the Lyman continuum flux and therefore, mass determination may not be accurate. An additional uncertainty is that some of the YSO candidates may not be YSOs. These sources are likely to be found in high galactic latitudes as well as in the regions where there is no evidence for dense molecular clouds or IRDCs.

The resulting population of high-mass stars produces ionizing photons and associated free-free emission. For our adopted IMF, this population produces ionizing photons at a rate $Q \approx 3 \times 10^{50} \text{ s}^{-1}$ and a brehmsstrahlung flux of $\sim 50 \text{ Jy}$ at 5GHz. Recent single dish radio observations of this region show a flux density of $\sim 10^3 \text{ Jy}$ at 5 GHz which includes both thermal and nonthermal emission (Law et al. 2008). The large scale $4^\circ \times 1^\circ$ radio study of this region shows that only $\sim 20\%$ of the flux at 5GHz is likely to be thermal. Thus, the YSO population may contribute up to a quarter of the observed thermal emission from the Galactic center region assuming that the fraction of thermal to nonthermal emission is the same in the central $400 \times 50 \text{ pc}$ ($|l| < 1.3^\circ$ and $|b| < 10'$) as it is in the central $4^\circ \times 1^\circ$. The remaining thermal flux of $\sim 150 \text{ Jy}$ may be associated with highly evolved HII regions resulting from earlier generations of star formation activity. This point will be discussed further in section 7.

6. $4.5\mu\text{m}$ Excess Sources

In previous sections, we have identified YSO candidates in the Galactic center region by studying the CMDs of the point sources in the surveyed region. We then refined the list of selected point sources from the CMD. The SED fitting of these selected sources used IRAC, MIPS and 2MASS data. These YSOs are identified to be mainly of Stage I with an age of $\sim 10^5$ years. We now identify YSOs that may be in a phase of star formation younger than $\sim 10^5$ years by examining the color of their emission in the IRAC bands. Recent studies have identified “green fuzzies” on the basis of excess emission at $4.5\mu\text{m}$ (Chambers et al. 2009). (the $4.5\mu\text{m}$ sources are also known as ‘extended green objects (EGSs)’ Cyganbowski et al. (2008)). Active cores show a correlation between $24\mu\text{m}$ point sources and the “green fuzzies” whereas a quiescent core shows no IR emission. The $4.5 \mu\text{m}$ excess emission is considered to be due to shock excited H_2 0-0 S(9) line emission (Noriega-Crespo et al. 2004) or the CO $\nu=1-0$ rovibrational bandhead (Marston et al. 2004). Using this color selection criterion, a recent IRAC survey of the Galactic plane has identified a number of interacting supernova remnants showing excess emission at $4.5\mu\text{m}$, indicating shocked, excited CO and H_2 molecular line emission (Reach et al. 2006). A strong correlation between shocked molecular H_2 gas and methanol masers has also been noted (Lee et al. 2001), suggesting outflow is taking place

at a very early stage of massive star formation, prior to the formation of a HII region. Also, more recently, the $4.5\mu\text{m}$ excess emission has been detected in DR21, a massive star formation site, in which the excess $4.5\mu\text{m}$ color is considered to be due a shocked molecular outflow (Marston et al. 2004; Smith et al. 2006; Cyganowski et al. 2008) or associated with high-mass protostars within the cores of IRDCs (Rathborne et al. 2005; Beuther et al. 2005).

6.1. Correlation with IRDCs

Since there is a great deal of molecular material as traced by IRDCs in the nuclear disk, we searched for excess emission at $4.5\mu\text{m}$ (“green” in 3-color images combining 3.6, 4.5 and $8\mu\text{m}$ emission) that traces molecular line emission. A quantified indication of excess $4.5\mu\text{m}$ emission is obtained by constructing the ratio $I(4.5)/[I(3.6)^{1.2} * I(5.8)]^{0.5}$. This essentially is the ratio of the actual $4.5\mu\text{m}$ intensity to that determined by a power-law interpolation of the 3.6 and $5.8\mu\text{m}$ intensities. It was found empirically that a slight ($\sim 10\%$) modification to the interpolation coefficients helps emphasize sources with unusually strong $4.5\mu\text{m}$ emission. In a map of this ratio across the entire IRAC survey of the Galactic center, most point sources exhibit a uniform ratio that is not very different from the background. In regions of high extinction (e.g. IR dark clouds, and Sgr B2), this ratio rises because the reddening reduces the $3.6\mu\text{m}$ intensity. However, there were of order 100 sources, located in regions of both high and low extinction that exhibit ratios distinctly higher than those of other sources in their vicinity (within several arc minutes). These include 33 sources that were visually selected as “green” sources in 3-color images. Their individual color images are shown in Figure 13; the $4.5\mu\text{m}$ excess sources show both extended and compact emission. The ratio also clearly identifies a number of interesting sources that do not stand out in the 3-color images. Our search should be compared with two recent studies. Using an algorithm that finds “green fuzzies,” Chambers et al. (2009) identified excess $4.5\mu\text{m}$ emission by confining to the cores of IRDCs. Another study by Cyganowski et al. (2008) visually identify “EGOs”. Our technique is sensitive to both compact and extended sources with $4.5\mu\text{m}$ excess emission, unlike other searches.

The spatial distribution of the $4.5\mu\text{m}$ excess sources is marked on Figure 14a which displays the ratio image of the region surveyed by IRAC. There are 33 sources that are characterized to have $4.5\mu\text{m}$ excess emission, three of which (g1, g2 and g4) coincide with known planetary nebulae (Jacoby & Van de Steene 2004). Thus, there are 30 sources that are candidate YSOs. It is quite possible that the list of $4.5\mu\text{m}$ excess sources is contaminated by additional PNe, distributed in the crowded region of the Galactic center. Half of the $4.5\mu\text{m}$ excess sources are near Sgr B2, G0.25+0.01, M-0.02-0.07, and Sgr C (G359.5-0.0). The rest appear to be distributed away from the Galactic plane, most likely associated with local objects distributed at negative latitudes. Although there is no bias in the selection of $4.5\mu\text{m}$ excess sources toward IRDCs, Figure 14a shows that most of the $4.5\mu\text{m}$ excess sources are distributed in the vicinity of IRDCs. The highest density of $4.5\mu\text{m}$ excess sources is near Sgr B2.

6.2. Correlation with Methanol Masers

To correlate the position of highly embedded YSO candidates with early sites of massive star formation, as traced by methanol masers, Figure 14b presents the spatial distribution of the known methanol masers on an $8\mu\text{m}$ image. A survey of the inner 2 degrees of the Galactic center showed a total of 23 class II methanol masers at 6.7 GHz (Caswell 1996). We used limited targeted surveys of class I methanol sources. The crosses show the position of class II methanol masers (Caswell 1996). The 6.7 GHz methanol maser observations searched the region along the plane between $|l| < 0.9^\circ$ and $|b| < 0.5^\circ$. Table 5 lists the position of the sources that are found within our IRAC survey. Table 6 shows the positions and fluxes of a subset of $4.5\mu\text{m}$ excess sources that were observed with MIPS at $70\mu\text{m}$.

It is now well established that methanol masers are signposts of ongoing massive star formation throughout the Galaxy. Class II methanol masers are recognized to be radiatively pumped, unlike class I methanol masers, which known to be collisionally pumped (Menten 1991). Tables 7 and 8 show the positions of class I and II methanol masers and their corresponding velocities, respectively. The correlation of methanol masers with the $4.5\mu\text{m}$ excess sources in the surveyed region was first reported by Yusef-Zadeh et al. (2007a). The number of $4.5\mu\text{m}$ excess sources distributed in the Galactic center region is 14 but we detected 6 methanol maser counterparts. Given the limited sensitivity of 1 Jy in the maser survey by Caswell (1996), it is possible that many of the $4.5\mu\text{m}$ excess sources have weak maser counterparts or that they signify different evolutionary phases of massive protostars when compared with the onset of methanol maser emission. A more detailed study of the correlation of 6.7 GHz methanol masers and EGOs with IRDCs in the GLIMPSE data was recently reported by Cyganowski et al. (2008).

6.3. The SEDs of $4.5\mu\text{m}$ Excess Sources

Using 2MASS, IRAC and MIPS point source catalogs as well as 850 and $450\mu\text{m}$ data (Pierce-Price et al. 2000), we constructed the SEDs of individual $4.5\mu\text{m}$ excess sources to be used in model fitting. Due to the lower resolution of the submillimeter data and the excess flux of molecular emission in the $4.5\mu\text{m}$ IRAC band, we show upper limits to the peak flux densities at 4.5, 450 and $850\mu\text{m}$ (Pierce-Price et al. 2000; Ramirez et al. 2008). The distances to many of the $4.5\mu\text{m}$ excess sources are unknown due to the difficulty in estimating the kinematic distances of sources in the direction toward the Galactic center. We assumed that the sources that are distributed at high galactic latitudes are most likely foreground sources whereas the range of distances for low latitude sources galactic latitudes is restricted to $|b| < 10'$ and they are near the Galactic center. The model fitting for foreground sources was restricted to distances ranging between 2 and 6 kpc whereas the the range of distances for low galactic latitudes is between 7.5 and 8.5 kpc. The derived masses and luminosities of the $4.5\mu\text{m}$ excess sources based on the well-fitted SED models are shown in Tables 9 and 10 for Galactic center and foreground sources, respectively. It should be pointed out

that if the fitter finds a low- A_v model to fit a source, that does not mean that the source is not at the Galactic center. The fitter will find models that can fit a range of A_v s even if the source is at the Galactic center by restricting this variable to reasonable values. This restriction allows the underlying YSO models to more appropriate models for fitting that source. We note that for the very young sources that we believe are associated with $4.5\mu\text{m}$ excesses, the YSO mass estimate is the current mass.

Assuming that the sources that are not SED fitted are YSOs, there are currently no available models in the grid to fit these sources. Also, the parameter “nfits” in Table 9 depends on how many datapoints are available. The fewer the datapoints, the more models can fit the data. If there are too many fits to the datapoints, it suggests the source is poorly constrained (which will show up in the standard deviations). On the other hand, if there are too few fits, it suggests the models are wrong (e.g., single source YSO trying to fit a cluster) or the data are bad. We note a strong correlation between the number of data points and χ^2 , as well as an inverse correlation between the number of data points and the number of “acceptable” models. And as the number of acceptable models increases, the (relative) uncertainties also increase, especially for $\langle L_\star \rangle$ and $\langle \dot{M}_{\text{env}} \rangle$. Nevertheless, it is clear that the number of fits and standard deviations allow us to identify well-constrained sources, unlike the CMD technique. We identify ten $4.5\mu\text{m}$ sources in Stage I and four in Stage II and III evolutionary phases. The fraction of Stage I sources is $\sim 70\%$ which is slightly lower than that found in the G359.43+0.02 cluster (78%) and higher than the fraction of 60% found in the region between $|b| = 10'$ and $|l| < 1.3^\circ$. This is consistent with the idea that the $4.5\mu\text{m}$ excess sources are in their early phase of evolution. The Tables presented here give sufficient information for use of the fits in future studies.

The visual extinction levels derived from fitting the SEDs of the sources which are most likely located near the Galactic center range between 5 and 47 magnitudes. Figure 15a shows the fitted SEDs of selected sources with high extinction. The number of good fits, as seen in Figure 15 and Table 9, depends both on the quality of the data, and the number of models that happen to have an SED that looks like the one fitted. We note from Figure 15 that g0, g5, g27, g31 are not well fit by the models as they seem to have narrow peaks at about $4 - 5\mu\text{m}$, dropping down on either side. Thus, unlike the rest, these sources are unlikely to be accreting YSOs. The correlation of $4.5\mu\text{m}$ sources and IRDCs is strong and is consistent with recent analysis by Chambers et al. (2009); we found 11 of the $4.5\mu\text{m}$ sources are correlated with IRDCs, half of them are not extended and six of the 14 sources have methanol maser counterparts. The correlation of the majority of $4.5\mu\text{m}$ excess sources with IRDCs, which are known to lie near the Galactic center, supports our initial choice for placing the low latitude $4.5\mu\text{m}$ excess sources at the distance of the Galactic center.

Appendix 1 describes each of the Galactic center and foreground $4.5\mu\text{m}$ excess sources.

7. Discussion

7.1. Star Formation History of the Nuclear Disk

To better understand the nature of star formation history in the complex region of the nuclear disk, we have used several different measurements. These measurements include $4.5\mu\text{m}$ excess sources, Stage I YSOs, thermal HII regions and diffuse nonthermal radio flux, each of which is described below.

We adopt, as in section 5.3, a standard broken power-law form of the IMF (Whitney et al. 2008; Kroupa 2001) to estimate on going star formation rate based on SED fitted $4.5\mu\text{m}$ excess sources. We believe these excess sources trace the earliest phase of star formation. Given a large uncertainty in the completeness of $4.5\mu\text{m}$ sources, the integrated mass of Stage I sources using Kroupa IMF, as before, is estimated to be $\sim 522 M_{\odot}$. Assuming that typical age of $4.5\mu\text{m}$ excess sources is $\sim 5 \times 10^4$ to 10^5 years, we estimate SFR 0.017 to $0.009 M_{\odot}\text{yr}^{-1}$, respectively. Given the vast amount of dense molecular gas corresponding to $\sim (5) \times 10^7 M_{\odot}$ residing in the Galactic center region, the efficiency of star formation is estimated to be $\sim 1 - 3.4 \times 10^{-10} \text{yr}^{-1}$.

A more robust approach to estimate SFR, as discussed earlier in section 5.3.2, is to use the evidence for a population of Stage I YSO candidates in the nuclear disk and make an estimate of the SFR $\sim 0.14 M_{\odot}\text{yr}^{-1}$ in the last 10^5 years. The star formation rate during this period appears to be an order of magnitude higher than that estimated from $4.5\mu\text{m}$ excess sources. These excess sources are in an earlier phase of their evolution and are younger than 10^5 years.

To estimate the SFR from young stellar objects older than 10^5 years, we used $24\mu\text{m}$ flux density. This flux is representative of the ionizing flux and hence of ages of a few million years. We find a total $24\mu\text{m}$ flux density of $1.17 \times 10^5 \text{ Jy}$ within the central region, $|l| < 1.3^{\circ}$, $|b| < 10'$ (i.e., a radius of 182 pc). The K-band extinction over this region appears to average slightly more than two magnitudes (Dutra et al. 2003) and the observed ratio of $A_{24}/A_K \sim 0.5$ (Chapman et al. 2009). We therefore corrected the observed flux density for 1.1 magnitudes of extinction. For a distance of 8.5 kpc, the resulting $24\mu\text{m}$ luminosity is $\sim 9 \times 10^7 L_{\odot}$. In the formulation of Rieke et al. (2009), this luminosity implies a SFR of $0.07 M_{\odot} \text{yr}^{-1}$, assuming a Kroupa IMF. This estimate implicitly assumes that the SED fitted YSOs did not contribute significantly to the total measured flux at $24\mu\text{m}$.

Lastly, nonthermal radio emission can be used as another proxy to determine SFR. This SFR probably applies to conditions some tens of millions of years ago (Helou & Bica 1993). The flux density of nonthermal emission is estimated to be 800 Jy at 6cm. If we extrapolate this flux to 21cm flux assuming a power law spectral index of 0.8, we derive a luminosity at this wavelength of $61.2 L_{\odot}$. This then yields a SFR of $0.007 M_{\odot} \text{yr}^{-1}$ (Rieke et al. 2009).

Taken together the above estimates provide a reasonable picture of large-scale star formation activity in the nuclear disk. We suggest that the region within ~ 200 pc of the Galactic center

was in a very quiescent state $\sim 10^7$ years ago, and that the SFR has been rising slowly, peaking to a value of $0.14 M_{\odot} \text{ yr}^{-1}$ around 10^5 years ago and then perhaps falling since then to the current value of $\sim 0.01 M_{\odot} \text{ yr}^{-1}$.

7.2. The Schmidt-Kennicutt Law in the Galactic Center

A motivation for this work has been to test the influence of the extreme ISM conditions in the central 400 pc of the Milky Way on the process of star formation. We have found that the behavior of various SFR indicators is consistent with expectations from the global properties of other galaxies. The value of $q_{24} = \log(f_{21cm}/f_{24\mu m}) \sim 2.1$, where f_{21cm} and $f_{24\mu m}$ represent flux densities at 21cm and $24\mu m$, respectively, is at the extreme high end of the range for external galaxies and is larger than is typically observed in the centers of nearby galaxies (Murphy et al. 2006) but can be explained in terms of a relatively low rate of star formation in the past. The properties of the individual forming massive stars also are consistent with those of similar objects elsewhere in the Galaxy.

A less ambiguous test for changes in star forming properties is based on the Schmidt-Kennicutt Law. This law is an empirical power-law relation between the surface densities of the interstellar gas and of star formation (see, e.g., Kennicutt 1998). If this law holds between the disk and center of the Milky Way, it would be strong evidence that the high interstellar gas temperatures in the latter region do not fundamentally alter the manner in which stars form there. Fuchs et al. (2009) have determined the relevant surface densities for the Milky Way disk near the sun and show that this region does indeed behave as expected according to the Schmidt-Kennicutt Law. We now estimate the same parameters for the central 0.8 kpc of the Galaxy. We take the mass in gas from Pierce-Price et al. (2000) to be $5.3 \pm 1.0 \times 10^7 M_{\odot}$. Our estimates of the SFR have a range: $0.007 M_{\odot} \text{ yr}^{-1}$ from the non thermal radio, $0.03 M_{\odot} \text{ yr}^{-1}$ from the youngest forming massive stars; $0.062 M_{\odot} \text{ yr}^{-1}$ from the $24\mu m$ luminosity; and a peak of $0.14 M_{\odot} \text{ yr}^{-1}$ from the $\sim 10^5$ year old YSO candidates. A long term time-averaged value can also be estimated. The enclosed mass in this region is $1.5 \times 10^9 M_{\odot}$ (Haller et al. 1996). Therefore, a strict upper limit on the average SFR over the past 10^{10} years is $0.15 M_{\odot} \text{ yr}^{-1}$; a more plausible average would be 25% to 50% of this value. This average is in good agreement with our measurements of the recent SFR and suggests that the variations represent fluctuations around this average. We take the typical recent SFR to lie between 0.04 and $0.08 M_{\odot} \text{ yr}^{-1}$. In Figure 16, we plot the Galactic center values on Figure 4 of Fuchs et al. (2009). In this figure, different types of Sa, Sb, and Sc galaxies are shown as open triangles, open circles, and filled circles. The red star is the value for the solar neighborhood and the blue cross is that for the Galactic center. The black line has a slope of 1.4, corresponding to the Schmidt-Kennicutt relationship found for external galaxies (Kennicutt 1998). The agreement is excellent, suggesting that to first order the star formation in the Galactic center region is not strongly affected by the environmental differences compared with the disk of the Galaxy.

8. Conclusions

In this paper, we have studied the distribution of interstellar dust clouds and the nature of star formation in the Galactic center region using the $24\mu\text{m}$ *Spitzer* MIPS survey augmented with additional mid-IR, near-IR, submillimeter and radio data. By making use of MSX data in regions where the MIPS data are saturated, we constructed a complete $24\mu\text{m}$ image of the Galactic center region with unprecedented sensitivity and resolution.

The comparison between the $24\mu\text{m}$ and $8\mu\text{m}$ images showed numerous examples of compact regions of $24\mu\text{m}$ emission surrounded by partial shells of $8\mu\text{m}$ emission. These structures are characteristic of H II regions, as seen throughout the Galactic plane, where luminous stars have heated large dust grains thus enhancing $24\mu\text{m}$ emission, and have destroyed PAHs thus suppressing $8\mu\text{m}$ emission.

We noted a number of elongated IRDCs distributed over a wide range of angular scales toward the Galactic center. Many of the IRDCs lie within a “bow-tie” structure, consisting of two layers parallel to the Galactic equator and at both positive and negative longitudes. Molecular line survey studies show counterparts to a large fraction of the IRDC of the bow-tie structure. The darkness of the two coherent IRDC layers provides relative locations of individual clouds with respect to each other. In particular, we note that clouds distributed on the positive longitudes (e.g., Sgr B2 and G0.25+0.01) are closer to us than those on the negative longitudes.

A result of the $24\mu\text{m}$ imaging is the recognition of a population of compact and point sources distributed between the two layers of IRDCs. This population is predominantly found at negative galactic longitudes, and includes a distinct cluster of sources at G359.43+0.02. Many of these sources are YSO candidates. Candidates are selected as particularly red objects in the $24 - 8\mu\text{m}$ color magnitude diagram, and characterized by modeling their SEDs. This led us to estimate the star formation rate of $0.14 M_{\odot}\text{yr}^{-1}$ based on SED fitted Stage I YSO candidates. The preponderance of Stage I YSO candidates implies that massive star formation took place in the nuclear disk about 10^5 years ago. The derived scale heights of the population of YSO candidates ($h \sim 7$ pc) as well as that of the molecular layer ($h \sim 10$ pc) suggest their being dynamically young. These measurements are consistent with a highly efficient burst of high mass star formation in the nuclear disk about 10^5 years ago. This aspect of the study characterizes the unique nature of the Galactic center region, apart from the general Galactic disk. Evidence for large-scale IRDCs throughout the Galactic center is consistent with the idea that massive star formation and massive cluster formation takes place in the central region of the Galaxy. Future study of this region with its steep gravitational potential provides a testing ground for large-scale formation of massive stars and/or star clusters.

Finally, we explored an independent means of identifying YSO candidates by finding sources with excess $4.5\mu\text{m}$ emission, indicating the presence of shocked molecular emission from protostellar sources. This color distinction was used as a proxy to probe the sites of star formation even earlier than 10^5 yrs old. We found 33 sources that show excess $4.5\mu\text{m}$ emission. Those at the lowest

latitudes were presumed to be at the Galactic Center, while those at higher latitudes often shown indication of being more local sources. SED fitting as well as the correlation of $4.5\mu\text{m}$ excess sources with methanol masers and IRDCs indicated the majority of these YSO candidates in Stage I and are likely to be associated with molecular outflows in sites of on-going star formation. Assuming that the $4.5\mu\text{m}$ excess sources provide us with all the sites of on-going star formation and that the SED fitted mass determination of the $4.5\mu\text{m}$ excess sources is applicable to these protostars, then we conclude that the efficiency of on-going star formation is lower than that estimated for the Galactic disk and is consistent with earlier studies of this region (Lis & Carlstrom 1994). The estimated values of SFR over different time scales up to 10^7 years ago suggest that large scale star formation in the nuclear disk is likely to be continuous over a long period. However, mild burst-like activity could increase SFR by an order of magnitude on a 10^5 year time scale.

We acknowledge the use of SCUBA data taken by D. Pierce-Price. This work is partially supported by the NSF under award number AST-0807400 and JPL/Caltech contract 1255094.

REFERENCES

- Adams, F. C., Lada, C. J., & Shu, F. H. 1987, *ApJ*, 312, 788
- Arendt, R. G., Stolovy, S. R., Ramirez, S. V., Sellgren, K., Cotera, A. S., Law, C. J., Yusef-Zadeh, F., Smith, H. A., & Gezari, D. Y. 2008, *ArXiv e-prints*, 804
- Argon, A. L., Reid, M. J., & Menten, K. M. 2000, *ApJS*, 129, 159
- Armstrong, J. T. & Barrett, A. H. 1985, *ApJS*, 57, 535
- Bally, J., Stark, A. A., Wilson, R. W., & Henkel, C. 1988, *ApJ*, 324, 223
- Bania, T. M. 1977, *ApJ*, 216, 381
- Becker, R. H., White, R. L., Helfand, D. J., & Zoonematkermani, S. 1994, *ApJS*, 91, 347
- Beuther, H., Churchwell, E. B., McKee, C. F., & Tan, J. C. 2007, in *Protostars and Planets V*, ed. B. Reipurth, D. Jewitt, & K. Keil, 165–180
- Beuther, H., Sridharan, T. K., & Saito, M. 2005, *ApJ*, 634, L185
- Binney, J., Gerhard, O. E., Stark, A. A., Bally, J., & Uchida, K. I. 1991, *MNRAS*, 252, 210
- Carey, S. J., Feldman, P. A., Redman, R. O., Egan, M. P., MacLeod, J. M., & Price, S. D. 2000, *ApJ*, 543, L157
- Carey, S. J., Noriega-Crespo, A., Mizuno, D. R., Shenoy, S., Paladini, R., Kraemer, K. E., Price, S. D., Flagey, N., Ryan, E., Ingalls, J. G., Kuchar, T. A., Pinheiro Gonçalves, D., Indebetouw, R., Billot, N., Marleau, F. R., Padgett, D. L., Rebull, L. M., Bressert, E., Ali,

- B., Molinari, S., Martin, P. G., Berriman, G. B., Boulanger, F., Latter, W. B., Miville-Deschenes, M. A., Shipman, R., & Testi, L. 2009, *PASP*, 121, 76
- Caswell, J. L. 1996, *MNRAS*, 283, 606
- Chapman, N. L., Mundy, L. G., Lai, S.-P., & Evans, N. J. 2009, *ApJ*, 690, 496
- Churchwell, E., Watson, D. F., Povich, M. S., Taylor, M. G., Babler, B. L., Meade, M. R., Benjamin, R. A., Indebetouw, R., & Whitney, B. A. 2007, *ApJ*, 670, 428
- Condon, J. J. 1992, *ARA&A*, 30, 575
- Cyganowski, C. J., Whitney, B. A., Holden, E., Braden, E., Brogan, C. L., Churchwell, E., Indebetouw, R., Watson, D. F., Babler, B. L., Benjamin, R., Gomez, M., Meade, M. R., Povich, M. S., Robitaille, T. P., & Watson, C. 2008, *AJ*, 136, 2391
- De Pree, C. G., Wilner, D. J., Deblasio, J., Mercer, A. J., & Davis, L. E. 2005, *ApJ*, 624, L101
- Di Francesco, J., Johnstone, D., Kirk, H., MacKenzie, T., & Ledwosinska, E. 2008, *ApJS*, 175, 277
- Dutra, C. M., Ortolani, S., Bica, E., Barbuy, B., Zoccali, M., & Momany, Y. 2003, *A&A*, 408, 127
- Egan, M. P., Shipman, R. F., Price, S. D., Carey, S. J., Clark, F. O., & Cohen, M. 1998, *ApJ*, 494, L199+
- Felli, M., Comoretto, G., Testi, L., Omont, A., & Schuller, F. 2000, *A&A*, 362, 199
- Figer, D. F., Kim, S. S., Morris, M., Serabyn, E., Rich, R. M., & McLean, I. S. 1999, *ApJ*, 525, 750
- Flaherty, K. M., Pipher, J. L., Megeath, S. T., Winston, E. M., Gutermuth, R. A., Muzerolle, J., Allen, L. E., & Fazio, G. G. 2007, *ApJ*, 663, 1069
- Fuerst, E., Reich, W., & Sofue, Y. 1987, *A&AS*, 71, 63
- Gaume, R. A., Claussen, M. J., de Pree, C. G., Goss, W. M., & Mehringer, D. M. 1995, *ApJ*, 449, 663
- Gordon, K. D., Engelbracht, C. W., Fadda, D., Stansberry, J., Wachter, S., Frayer, D. T., Rieke, G., Noriega-Crespo, A., Latter, W. B., Young, E., Neugebauer, G., Balog, Z., Beeman, J. W., Dole, H., Egami, E., Haller, E. E., Hines, D., Kelly, D., Marleau, F., Misselt, K., Morrison, J., Pérez-González, P., Rho, J., & Wheaton, W. A. 2007, *PASP*, 119, 1019
- Güsten, R. & Philipp, S. D. 2004, in *The Dense Interstellar Medium in Galaxies*, ed. S. Pfalzner, C. Kramer, C. Staubmeier, & A. Heithausen, 253–+
- Habing, H. J. 1996, *A&A Rev.*, 7, 97
- Haschick, A. D., Menten, K. M., & Baan, W. A. 1990, *ApJ*, 354, 556

- Herrnstein, R. M. & Ho, P. T. P. 2005, *ApJ*, 620, 287
- Hinz, J. L., Rieke, G. H., Yusef-Zadeh, F., Hewitt, J., Balog, Z., & Block, M. 2009, *ApJS*
- Jacoby, G. H. & Van de Steene, G. 2004, *A&A*, 419, 563
- Jones, P. A., Burton, M. G., Cunningham, M. R., Menten, K. M., Schilke, P., Belloche, A., Leurini, S., Ott, J., & Walsh, A. J. 2008, *MNRAS*, 386, 117
- Kerber, F., Mignani, R. P., Guglielmetti, F., & Wicenc, A. 2003, *A&A*, 408, 1029
- Kroupa, P. 2001, *MNRAS*, 322, 231
- Lada, C. J. 1987, in *IAU Symposium, Vol. 115, Star Forming Regions*, ed. M. Peimbert & J. Jugaku, 1–17
- Lada, C. J. 1999, in *NATO ASIC Proc. 540: The Origin of Stars and Planetary Systems*, ed. C. J. Lada & N. D. Kylafis, 143–+
- Lang, C. C., Morris, M., & Echevarria, L. 1999, *ApJ*, 526, 727
- Law, C. & Yusef-Zadeh, F. 2004, *ApJ*, 611, 858
- Law, C. J., Yusef-Zadeh, F., Cotton, W. D., & Maddalena, R. J. 2008, *ApJS*, 177, 255
- Lee, J.-K., Walsh, A. J., Burton, M. G., & Ashley, M. C. B. 2001, *MNRAS*, 324, 1102
- Li, A. & Draine, B. T. 2001, *ApJ*, 554, 778
- Lindqvist, M., Habing, H. J., & Winnberg, A. 1992, *A&A*, 259, 118
- Lis, D. C. & Carlstrom, J. E. 1994, *ApJ*, 424, 189
- Lis, D. C., Keene, J., Phillips, T. G., Schilke, P., Werner, M. W., & Zmuidzinas, J. 2001, *ApJ*, 561, 823
- Lis, D. C. & Menten, K. M. 1998, *ApJ*, 507, 794
- Loose, H. H., Kruegel, E., & Tutukov, A. 1982, *A&A*, 105, 342
- Lu, J. R., Ghez, A. M., Hornstein, S. D., Morris, M., Matthews, K., Thompson, D. J., & Becklin, E. E. 2006, *Journal of Physics Conference Series*, 54, 279
- Marston, A. P., Reach, W. T., Noriega-Crespo, A., Rho, J., Smith, H. A., Melnick, G., Fazio, G., Rieke, G., Carey, S., Rebull, L., Muzerolle, J., Egami, E., Watson, D. M., Pipher, J. L., Latter, W. B., & Stapelfeldt, K. 2004, *ApJS*, 154, 333
- Martin, C. L., Walsh, W. M., Xiao, K., Lane, A. P., Walker, C. K., & Stark, A. A. 2004, *ApJS*, 150, 239

- Mar Vsáľková, P. 1974, *Ap&SS*, 27, 3
- Mehringner, D. M., Goss, W. M., Lis, D. C., Palmer, P., & Menten, K. M. 1998, *ApJ*, 493, 274
- Menten, K. M. 1991, *ApJ*, 380, L75
- Morris, M. & Serabyn, E. 1996, *ARA&A*, 34, 645
- Morris, M., Uchida, K., & Do, T. 2006, *Nature*, 440, 308
- Nord, M. E., Lazio, T. J. W., Kassim, N. E., Hyman, S. D., LaRosa, T. N., Brogan, C. L., & Duric, N. 2004, *AJ*, 128, 1646
- Noriega-Crespo, A., Moro-Martin, A., Carey, S., Morris, P. W., Padgett, D. L., Latter, W. B., & Muzerolle, J. 2004, *ApJS*, 154, 402
- Oka, T., Geballe, T. R., Goto, M., Usuda, T., & McCall, B. J. 2005, *ApJ*, 632, 882
- Oka, T., Hasegawa, T., Sato, F., Tsuboi, M., & Miyazaki, A. 1998, *ApJS*, 118, 455
- Omont, A. e. a. 2003, *A&A*, 403, 975
- Panagia, N. 1973, *AJ*, 78, 929
- Paumard, T., Genzel, R., Martins, F., Nayakshin, S., Beloborodov, A. M., Levin, Y., Trippe, S., Eisenhauer, F., Ott, T., Gillessen, S., Abuter, R., Cuadra, J., Alexander, T., & Sternberg, A. 2006, *ApJ*, 643, 1011
- Pierce-Price, D., Richer, J. S., Greaves, J. S., Holland, W. S., Jenness, T., Lasenby, A. N., White, G. J., Matthews, H. E., Ward-Thompson, D., Dent, W. R. F., Zylka, R., Mezger, P., Hasegawa, T., Oka, T., Omont, A., & Gilmore, G. 2000, *ApJ*, 545, L121
- Povich, M. S., Stone, J. M., Churchwell, E., Zweibel, E. G., Wolfire, M. G., Babler, B. L., Indebetouw, R., Meade, M. R., & Whitney, B. A. 2007, *ApJ*, 660, 346
- Ramirez, S. V., Arendt, R. G., Sellgren, K., Stolovy, S. R., Cotera, A., Smith, H. A., & Yusef-Zadeh, F. 2008, *ApJS*, 175, 147
- Rathborne, J. M., Jackson, J. M., Chambers, E. T., Simon, R., Shipman, R., & Frieswijk, W. 2005, *ApJ*, 630, L181
- Reach, W. T., Rho, J., Tappe, A., Pannuti, T. G., Brogan, C. L., Churchwell, E. B., Meade, M. R., Babler, B., Indebetouw, R., & Whitney, B. A. 2006, *AJ*, 131, 1479
- Rieke, G. H., Alonso-Herrero, A., Weiner, B. J., Pérez-González, P. G., Blaylock, M., Donley, J. L., & Marcillac, D. 2009, *ApJ*, 692, 556
- Robitaille, T. P., Whitney, B. A., Indebetouw, R., & Wood, K. 2007, *ApJS*, 169, 328

- Robitaille, T. P., Whitney, B. A., Indebetouw, R., Wood, K., & Denzmore, P. 2006, *ApJS*, 167, 256
- Schuller, F., Omont, A., Glass, I. S., Schultheis, M., Egan, M. P., & Price, S. D. 2006, *A&A*, 453, 535
- Sevenster, M. N., Chapman, J. M., Habing, H. J., Killeen, N. E. B., & Lindqvist, M. 1997a, *A&AS*, 122, 79
- . 1997b, *A&AS*, 124, 509
- Sharpless, S. 1959, *ApJS*, 4, 257
- Shiki, S., Ohishi, M., & Deguchi, S. 1997, *ApJ*, 478, 206
- Simon, R., Rathborne, J. M., Shah, R. Y., Jackson, J. M., & Chambers, E. T. 2006, *ApJ*, 653, 1325
- Sjouwerman, L. O., van Langevelde, H. J., Winnberg, A., & Habing, H. J. 1998, *A&AS*, 128, 35
- Skrutskie, M. F., Schneider, S. E., Stiening, R., Strom, S. E., Weinberg, M. D., Beichman, C., Chester, T., Cutri, R., Lonsdale, C., Elias, J., Elston, R., Capps, R., Carpenter, J., Huchra, J., Liebert, J., Monet, D., Price, S., & Seitzer, P. 1997, in *Astrophysics and Space Science Library*, Vol. 210, *The Impact of Large Scale Near-IR Sky Surveys*, ed. F. Garzon, N. Epchtein, A. Omont, B. Burton, & P. Persi, 25–+
- Smith, H. A., Hora, J. L., Marengo, M., & Pipher, J. L. 2006, *ApJ*, 645, 1264
- Stark, A. A., Bally, J., Gerhard, O. E., & Binney, J. 1991, *MNRAS*, 248, 14P
- Stolovy, S., Ramirez, S., Arendt, R. G., Cotera, A., Yusef-Zadeh, F., Law, C., Gezari, D., Sellgren, K., Karr, J., Moseley, H., & Smith, H. A. 2006, *Journal of Physics Conference Series*, 54, 176
- Taylor, G. B., Morris, M., & Schulman, E. 1993, *AJ*, 106, 1978
- Tilley, D. A., Balsara, D. S., & Howk, J. C. 2006, *MNRAS*, 371, 1106
- Tsuboi, M., Handa, T., & Ukita, N. 1999, *ApJS*, 120, 1
- Tutukov, A. & Kruegel, E. 1978, *A&A*, 67, 437
- Uchida, K., Morris, M., & Serabyn, E. 1990, *ApJ*, 351, 443
- Vacca, W. D., Garmany, C. D., & Shull, J. M. 1996, *ApJ*, 460, 914
- Val'tts, I. E., Ellingsen, S. P., Slysh, V. I., Kalenskii, S. V., Otrupcek, R., & Larionov, G. M. 2000, *MNRAS*, 317, 315
- Van de Steene, G. C. & Jacoby, G. H. 2001, *A&A*, 373, 536

- Wardle, M. & Yusef-Zadeh, F. 2008, ArXiv e-prints, 805
- Watson, C., Povich, M. S., Churchwell, E. B., Babler, B. L., Chunev, G., Hoare, M., Indebetouw, R., Meade, M. R., Robitaille, T. P., & Whitney, B. A. 2008, ApJ, 681, 1341
- Whitney, B. A., Sewilo, M., Indebetouw, R., Robitaille, T. P., Meixner, M., Gordon, K., Meade, M. R., Babler, B. L., Harris, J., Hora, J. L., Bracker, S., Povich, M. S., Churchwell, E. B., Engelbracht, C. W., For, B.-Q., Block, M., Misselt, K., Vijn, U., Leitherer, C., Kawamura, A., Blum, R. D., Cohen, M., Fukui, Y., Mizuno, A., Mizuno, N., Srinivasan, S., Tielens, A. G. G. M., Volk, K., Bernard, J.-P., Boulanger, F., Frogel, J. A., Gallagher, J., Gorjian, V., Kelly, D., Latter, W. B., Madden, S., Kemper, F., Mould, J. R., Nota, A., Oey, M. S., Olsen, K. A., Onishi, T., Paladini, R., Panagia, N., Perez-Gonzalez, P., Reach, W., Shibai, H., Sato, S., Smith, L. J., Staveley-Smith, L., Ueta, T., Van Dyk, S., Werner, M., Wolff, M., & Zaritsky, D. 2008, AJ, 136, 18
- Whitney, B. A., Wood, K., Bjorkman, J. E., & Cohen, M. 2003a, ApJ, 598, 1079
- Whitney, B. A., Wood, K., Bjorkman, J. E., & Wolff, M. J. 2003b, ApJ, 591, 1049
- Yusef-Zadeh, F., Goss, W. M., Roberts, D. A., Robinson, B., & Frail, D. A. 1999, ApJ, 527, 172
- Yusef-Zadeh, F., Hewitt, J. W., & Cotton, W. 2004, ApJS, 155, 421
- Yusef-Zadeh, F. & Morris, M. 1987, AJ, 94, 1178
- Yusef-Zadeh, F., Morris, M., & Chance, D. 1984, Nature, 310, 557
- Yusef-Zadeh, F., Wardle, M., Munro, M., Law, C., & Pound, M. 2005, Advances in Space Research, 35, 1074
- Zhao, J.-H., Desai, K., Goss, W. M., & Yusef-Zadeh, F. 1993, ApJ, 418, 235
- Zoonematkermani, S., Helfand, D. J., Becker, R. H., White, R. L., & Perley, R. A. 1990, ApJS, 74, 181
- Zylka, R., Mezger, P. G., & Wink, J. E. 1990, A&A, 234, 133

9. Appendix

We assumed that the sources that are distributed at high galactic latitudes are most likely foreground sources whereas the low latitude sources ($|b| < 10'$) are near the Galactic center. We

first describe $4.5\mu\text{m}$ excess sources which are most likely located in the Galactic center region followed by foreground sources. In all the figures presented below, the circles mark the position of the $4.5\mu\text{m}$ excess sources. For extended $4.5\mu\text{m}$ sources, the peak of the excess emission is used to identify the closest point sources in the IRAC and MIPS catalogs by Ramirez et al. (2008) and Hinz et al. (2009), respectively.

The squares represent sources that were observed at $70\mu\text{m}$. The distribution of class I and II methanol masers are also drawn on these figures as plus(+) and cross (x) signs, respectively.

9.1. Galactic Center $4.5\mu\text{m}$ Excess Sources

G1.041-0.072 (g0)

This source lies at the eastern edge of the ridge of IRDCs and is not well fit as it shows a narrow peak in its SED, thus it is unlikely to be at an early phase of a YSO. The fitted SED gives a protostellar source with a mass of $\sim 10 M_{\odot}$. This $4.5\mu\text{m}$ excess source has a $24\mu\text{m}$ counterpart, as shown in Figure 17a and lies within an arc-minute of an extended $8\mu\text{m}$ and $24\mu\text{m}$ HII source G1.05-0.071 at $l=1^{\circ} 3' 4''$, $b=-4' 15''$. This extended source is also shown in the 3-color image, as presented in Figure 13. Figure 17b shows contours of $850\mu\text{m}$ emission that trace the elongated east-west IRDC. The strongest $850\mu\text{m}$ emission coincides with G1.05-0.071.

G0.826-0.211(g3)

This $4.5\mu\text{m}$ excess source is embedded in the IRDC associated with Sgr B2. The distribution of the IRDC ridge at the location of g3 widens in a plume-like structure pointed southward of the Galactic plane. Figure 17c,d show contours of 450 and $850\mu\text{m}$ emission from this prominent IRDC. A $24\mu\text{m}$ and $8\mu\text{m}$ source coincides with g3, which is shown as a circle in Figure 17. This $4.5\mu\text{m}$ excess source was also observed at $70\mu\text{m}$, as shown by a square sign in Figures 17c,d, but was not detected (see Table 6). Most of the well-known ultracompact HII regions associated with Sgr B2 are located to the northwest of g3, as shown in Figure 14a. The SED fit to this source gives a mass of $13.7 M_{\odot}$. This $4.5\mu\text{m}$ excess source is located within $20''$ of SiO 17452-2819 with a radial velocity of 90 km s^{-1} (Shiki et al. 1997). The location of this maser source with respect to g3 supports the idea that this SiO maser is associated with the Sgr B2 star forming region and is a counterpart to a young stellar object. The correlation of submillimeter emission, IRDC, $24\mu\text{m}$ point source and excess $4.5\mu\text{m}$ emission is consistent with g3 being a massive YSO associated with an active core.

Sgr B2 (g6-g10)

The largest concentration of $4.5\mu\text{m}$ excess sources is located in Sgr B2, which is one of the most massive star forming sites in the Galaxy. SED fits to the five $4.5\mu\text{m}$ excess sources g6 to g10 give the highest protostellar masses among the $4.5\mu\text{m}$ excess sources, ranging between 8 and $22 M_{\odot}$. Figure 18a,b shows contours of 450 and $850\mu\text{m}$ emission that are superimposed on $8\mu\text{m}$ and

20cm images of Sgr B2, respectively. It is clear that the IRDC associated with Sgr B2 is traced remarkably well by submillimeter and molecular line emission from several active molecular cores (Jones et al. 2008). The distribution of compact HII regions, as shown best at 20cm wavelength, indicates that they lie at the southern edge of the dark cloud. The distribution of UC HII regions as well as $24\mu\text{m}$ sources suggests a later phase of massive star formation at the southern edge of IRDC where UC HII regions are concentrated. However, the distribution of methanol sources are seen silhouetted against the middle of the infrared dark cloud. Figure 18c makes this point even clearer by showing that most of the methanol sources are displaced with respect to $24\mu\text{m}$ sources heated by UC HII regions lie at the edge of the IRDC. The high column density of Sgr B2 and the saturation of the brighter $24\mu\text{m}$ sources are likely responsible for a lack of additional detection of $4.5\mu\text{m}$ excess sources and YSO candidates in Sgr B2. Nevertheless, the projected displacement between $24\mu\text{m}$ sources and methanol sources is consistent with a picture that star formation in the IRDC associated with Sgr B2 has taken place from outside in.

Figure 18d shows contours of emission from one of the $4.5\mu\text{m}$ excess sources, g6, that shows extended emission at $4.5\mu\text{m}$. Three of the five $4.5\mu\text{m}$ excess sources, g6, g8 and g9, coincide with ultracompact HII regions Sgr B2 R, I and F (Gaume et al. 1995). We note that Sgr B2-F itself breaks up into multiple radio components that are considered to be members of a cluster of massive ultracompact HII regions (De Pree et al. 2005). The parameters of the SED fit to g9 should be considered with caution, given that multiple sources could contribute to the SED. Fortunately, the flux from a cluster of massive stars is likely to be dominated by the most massive star as luminosity is a steep power of mass and thus the assumption of all the luminosity arising from a single cluster member is reasonable.

G0.376+0.04 (g16)

The $4.5\mu\text{m}$ excess source associated with g16 is detected against the IRDC ridge at G0.376+0.04. This source coincides with one of the string of submillimeter emitting clouds, known as the dust ridge in Figure 1c (Lis & Menten 1998). g16 coincides with a class II methanol maser at a velocity of 37 km s^{-1} that is listed as source 8 in Table 8. Molecular line studies of the ridge of IRDCs are dominated by velocities ranging between 20 and 30 km s^{-1} (Oka et al. 2005). Figures 19a,b show contours of $450\mu\text{m}$ and $850\mu\text{m}$ emission and are superimposed on grayscale $24\mu\text{m}$ and 20cm images of this cloud. This is the first evidence that this cloud shows a signature of massive star formation as the fitted SED indicates $10 M_{\odot}$ for this YSO, the first evidence that this cloud is a site of massive star formation (Argon et al. 2000). Following the definition of active and quiescent cores by Chambers et al. (2009), the eastern half of the IRDC ridge is in its quiescent phase of star formation whereas the western half is forming massive YSOs. The $4.5\mu\text{m}$ excess source also lies in the vicinity of a nonthermal radio filament that appears to terminate in the IRDC and about $1'$ east of g16, as shown in Figure 19b. Figure 19c shows contours of $4.5\mu\text{m}$ emission from G0.376+0.04.

G359.932-0.063 (g23)

This $4.5\mu\text{m}$ excess source lies at the edge of the 50 km s^{-1} molecular cloud M-0.13-0.08 (Herrnstein

& Ho 2005; Armstrong & Barrett 1985). Figures 20a,b show contours of submillimeter emission from two prominent 50 km s^{-1} and 20 km s^{-1} molecular clouds, known to be the closest clouds to the Galactic center. Contours of $450\mu\text{m}$ and $850\mu\text{m}$ emission from these clouds are superimposed on the $8\mu\text{m}$ and 20cm images of the Sgr A region, respectively. The 50 km s^{-1} cloud is known to be interacting with the Sgr A E East SNR G0.0+0.0 (Zylka et al. 1990) and several OH masers at 1720 MHz have trace the interaction site (Yusef-Zadeh et al. 1999). The shell-like Sgr A East supernova remnant is shown in Figure 20b. The position of g23 lies within five arcseconds of OH(1720 MHz) maser H at a velocity of 49 km s^{-1} . The excess $4.5\mu\text{m}$ emission at this position could be associated with the supernova shock interaction. $4.5\mu\text{m}$ excess emission has been seen toward a number of supernova remnants (Reach et al. 2006). However, the parameters of the SED of this source suggest that G359.23-0.063 is associated with a $11 M_{\odot}$ protostar (see Table 9). If so, the protostar presents the earliest phase of massive star formation in the 50 km s^{-1} cloud, perhaps triggered by the interaction with the expanding Sgr A East supernova remnant. A chain of ultracompact HII regions $\sim 2'$ northeast of g23 may trace massive star formation at a later phase than that shown by g23. Figure 20c shows a $24\mu\text{m}$ image of IRDC associated with the 50 km s^{-1} and clearly shows the IRDC toward the region where g23 is detected. The evidence for collisionally excited methanol emission has also been reported toward the 50 km s^{-1} ((Haschick et al. 1990), see source 2 in Table 7). This result supports the presence of massive star formation in this region. Figure 20d shows contours of $4.5\mu\text{m}$ emission from g23.

The 20 km s^{-1} and 50 km s^{-1} IRDCs are also located in a region where 19 radio filaments (A1-A19) have been detected at 20cm (Yusef-Zadeh et al. 2004). Two of these nonthermal radio filaments RF-A3 and RF-A9 are labeled in Figure 20b. The nonthermal filaments (e.g., G359.90-0.07 and G359.88-0.07) may be interacting with the 20 km s^{-1} molecular cloud (Yusef-Zadeh et al. 2005).

G359.841-0.080 (g25)

G359.841-0.08 is another $4.5\mu\text{m}$ excess source that is found at the western edge of the 20 km s^{-1} molecular cloud M-0.02-0.07 (Herrnstein & Ho 2005; Armstrong & Barrett 1985), which is traced by the prominent IRDC at $24\mu\text{m}$, as presented in Figure 20c. Evidence for a signature of star formation is supported by the presence of star formation by a class I methanol maser and a HII region toward the eastern half of the cloud. The methanol maser source is detected at a velocity of 21 km s^{-1} (Haschick et al. 1990; Val'tts et al. 2000). Additional observations are needed to confirm the association of this $4.5\mu\text{m}$ excess source with the 20 km s^{-1} cloud. Contours of $4.5\mu\text{m}$ emission are shown in Figure 20d. The peak of submillimeter emission from the 20 km s^{-1} IRDC shows no signs of star formation, thus, is considered to be a quiescent core.

G359.599-0.032 (g27)

This $4.5\mu\text{m}$ excess source is projected against the IRDC ridge, on the negative longitude side of the Galactic center. Figure 21a,b shows a $24\mu\text{m}$ and 6cm continuum images of this source, respectively, and the contours of $4.5\mu\text{m}$ emission are shown in Figure 21c. The parameters of the fit to this source

suggests a $14.5 \pm 3.5 M_{\odot}$ protostar. However, g27 shows a narrow peak in its SED and is not fitted well by the models. This source is located about $35''$ north of an HII region and a shell-like structure with a diameter of $30''$ centered at G359.61-0.045. The shell-like structure is best seen at $24\mu\text{m}$ in Figure 21a.

G359.437-0.102 (g29)

Figure 22a,b shows contours of $450\mu\text{m}$ and $850\mu\text{m}$ emission superimposed on $8\mu\text{m}$ and 20cm continuum images of the Sgr C HII region, respectively. This well-known HII region is one of the brightest extended HII regions in the Galactic center region. The Sgr C HII region was saturated at $24\mu\text{m}$, so we combined the image with the MSX image at the same wavelength band. The Sgr C IRDC is elongated and runs roughly along the Galactic plane. It is detected at both $8\mu\text{m}$ and $24\mu\text{m}$, as shown in Figure 22c. This IRDC is traced by submillimeter emission showing several cores along its elongated structure. The peak emission at $24\mu\text{m}$ coincides with the peak HII emission at 20cm and suggests that warm grains are being heated by the central O4 star.

The $4.5\mu\text{m}$ excess source g29 lies at the peak of the submillimeter emission and is shown as a circle in Figure 22a,b,c. The crosses show the positions of class II methanol masers with velocities of -52 and -53 km s^{-1} . The masers are listed as sources number 1 and 2 in Table 8. Radio recombination line measurements of the Sgr C HII region show a radial velocity of $\sim -65 \text{ km s}^{-1}$ (Liszt 1992; Liszt and Spiker 1995). Figure 22d shows contours of the extended $4.5\mu\text{m}$ excess emission. The corresponding color image of the $4.5\mu\text{m}$ excess source can be seen in Figure 13. The modeled SED of the $4.5\mu\text{m}$ excess source G359.436-0.102 in Sgr C indicates that the central protostellar candidate coincides with the northern maser source. Figure 15a shows the best fitted models to the data using 2MASS, IRAC, MIPS and SCUBA data accounting for 22 magnitudes of visual extinction. This SED fit is consistent with the identification of the $4.5\mu\text{m}$ excess source with a massive $14 M_{\odot}$ protostellar source (see Table 9) associated with the methanol masers.

The region surrounding $4.5\mu\text{m}$ excess source (g29) is complex. The emission at 4.5 and $5.8\mu\text{m}$ is extended whereas the emission at $8\mu\text{m}$ has a point-like structure and does not appear to have a counterpart at shorter wavelengths. The $8\mu\text{m}$ source is $\sim 6''$ away from the center of the $4.5\mu\text{m}$ emission. There are three other nearby compact sources; higher resolution study is needed to clarify the nature of these $8\mu\text{m}$ sources. However, it is most likely that the extended emission from the region close to the $4.5\mu\text{m}$ excess source represents shocked molecular outflow from the YSO candidate. This is consistent with the presence of submillimeter core, methanol masers, IRDC and $4.5\mu\text{m}$ excess, all of which suggest an active phase of massive star formation at the northwestern edge of Sgr C. The southeastern half of the IRDC shows no signs of active star formation.

There is a puzzling feature at the northeastern boundary of Sgr C IRDC, a lack of strong free-free radio continuum and submillimeter emission $l=-34'10''$, $b=-5'45''$. This implies that there is a cavity in the ionized gas and emission by dust at the interface between the submillimeter core and the Sgr C HII region. However, it is possible that the appearance of the cavity results from poor sensitivity in the submillimeter.

At 20cm, there is a compact bright continuum source at $l = -34'29''.19$, $b = -6'38''.15$ which is about $1'$ or 2.4 pc (the Galactic center distance of 8.5 kpc) from the positions of the methanol masers. The flux density of this source is 20 ± 1.8 mJy. The most prominent nonthermal radio filaments of Sgr C, as shown in Figure 22b, becomes quite faint inside the HII complex. The long nonthermal filaments appear to lie at eastern edge of the Sgr C cavity and the HII region. Like other filaments described in the Sgr A and Sgr B clouds, the prominent nonthermal filament appears to terminate at the Sgr C IRDC.

G359.30+0.033 (g30)

This $4.5\mu\text{m}$ excess source is detected at the edge of an elongated and narrow IRDC at $l=40'$, $b=2'$. This feature appears to widen in the direction away from the Galactic plane, resembling the vertical molecular Clumps 1 and 2 that are found at $l=355^0$ and $l=3^0$ and $b=0^0$ (Bania 1977). Figures 23a,b show an $8\mu\text{m}$ and $24\mu\text{m}$ images of this remarkable filamentary dark cloud. The cloud is drawn schematically in Figure 1c. The brightness of this cloud in the ratio map shown in Figure 3b suggests that it is likely to be on the front side of the Galactic center. Contours of $4.5\mu\text{m}$ emission from the region where excess emission is detected at this wavelength are shown in Figure 23c. The fit to the SED of this source suggests a $8.9 M_{\odot}$ protostar (see Table 9).

G359.199+0.041 (g31)

This $4.5\mu\text{m}$ excess source is projected against an east-west elongated IRDC. Figures 24a,b show $24\mu\text{m}$ and 20cm continuum images of this source. A methanol maser source and a 20cm continuum source lie in its vicinity, $4'$ away from the $4.5\mu\text{m}$ excess source. If the methanol source is associated with the same IRDC toward which the $4.5\mu\text{m}$ excess source is detected, then the IRDC is a site of massive star formation. Contours of $4.5\mu\text{m}$ emission from this cloud are shown in Figure 24c. The fit to the SED of this source suggests a $14.4 M_{\odot}$ protostar (see Table 9). However, the SED is not fitted well by the models because of the narrow peak at mid-IR wavelengths.

G358.980+0.084 (g32)

The $4.5\mu\text{m}$ excess source 32 is projected at the center of an IRDC which has a spidery appearance. Figures 25a,b show $24\mu\text{m}$ and $8\mu\text{m}$ images of this source. There is no evidence of a compact radio counterpart at 20cm to the $4.5\mu\text{m}$ excess source, though, a compact source is detected about $1'$ southwest of it. The methanol maser coincident with the position of the $4.5\mu\text{m}$ excess source supports the presence of on-going massive star formation in this dark cloud. The SED fit to the source identified by its excess $4.5\mu\text{m}$ emission gives a $7.6 M_{\odot}$ protostar. Figure 25d presents contours of $4.5\mu\text{m}$ emission from this source.

9.2. Foreground $4.5\mu\text{m}$ Excess Sources

Figure 15b and Table 10 show the SEDs of individual foreground sources and list the physical characteristics derived from the fits, respectively. The estimated A_v range between 4 and 33 magnitudes. Due to the distance uncertainty, the mass estimate is not well constrained. We note that with the exception of three sources, all the $4.5\mu\text{m}$ excess sources appear to be extended. In addition, with the exception of one, all the SED fitted sources appear to be in Stage I suggesting their early evolutionary phase.

0.955-0.786 (g1), 0.868-0.697 (g2) and 0.780-0.740 (g4)

All the three $4.5\mu\text{m}$ excess sources g1, g2 and g4 are located at the edge of the region surveyed with IRAC. Source g1, g4 and g2 coincide with the positions of three planetary nebulae JaST 76 and JaST 70 in (Van de Steene & Jacoby 2001) and PN G0.8-0.6 in (Kerber et al. 2003), respectively. The SEDs of these sources are shown in Figure 16b. The successful fitting of these PNe shows that SED fitting can not be used to distinguish them from other source types. Additional compact $4.5\mu\text{m}$ excess sources may be PNe that are misidentified as YSOs.

G0.708+0.408 (g5)

This source is projected against an IRDC observed with the MIPS and IRAC data. Figures 26a,b show a $24\mu\text{m}$ image and a $4.5\mu\text{m}$ contour of the $4.5\mu\text{m}$ excess source. The SED fit to this source suggests a $6 M_\odot$ protostar (see Table 10) as shown in Figure 16b. However, the SED is not fit well because of its narrow peak.

$4.5\mu\text{m}$ Excess Sources Associated with Sh20 (g11-g15, g12-g14)

Several $4.5\mu\text{m}$ excess sources associated with Sh20, are distributed at negative latitudes where several prominent optical emission nebulae have been identified. The $4.5\mu\text{m}$ excess sources g11, g12, g13, g14 and g15 are most likely associated Sh20 (Sharpless 20) centered at $l=0.5^\circ$, $b=-0.3^\circ$ with an extent of $10'$ (Mar Vřálková 1974). The SED fitting to these $4.5\mu\text{m}$ excess sources give masses in the range between 2 and $14 M_\odot$ (see Table 10).

Figures 27a,b show $24\mu\text{m}$ and $8\mu\text{m}$ images of G0.542-0.476 where $4.5\mu\text{m}$ excess source g11 is detected. The $4.5\mu\text{m}$ excess source appears to be projected against a dearth of emission at $8\mu\text{m}$ in the vicinity of an elongated IRDC with an extent of $2'$. A sharp linear feature with an extent of $\sim 1'$ lies to the north. The lack of a counterpart at $24\mu\text{m}$ and/or at radio wavelengths suggests that this linear feature is likely to arise from PAH emission. Figure 27c shows a radio continuum image of the region where g11 is detected and Figure 27d shows a $4.5\mu\text{m}$ contour map of g11.

Other $4.5\mu\text{m}$ excess sources that appear to be associated with Sharpless 20 are G0.517-0.657 (g12), G0.483-0.701 (g13) and G0.477-0.727 (g14). Figures 28a,b,c show $24\mu\text{m}$, $8\mu\text{m}$ and 20cm grayscale images of the region where these $4.5\mu\text{m}$ excess sources are detected. The $4.5\mu\text{m}$ emission contours for g12, g13 and g14 are shown in Figures 28d,e,f, respectively. It is clear that this is a

region of massive star formation where sharp extended shell-like structures and a compact radio continuum source coincident with g14 are seen at $24\mu\text{m}$ and 20cm. No $8\mu\text{m}$ counterparts are found.

Another HII structure with the appearance of a “question mark” is a component of Sharpless 20. The $4.5\mu\text{m}$ excess source g15 lies at the center of this HII region. Figures 29a,b,c show grayscale images at $24\mu\text{m}$, $8\mu\text{m}$, and 20cm, respectively, where as a contour map of g15 at $4.5\mu\text{m}$ is shown in Figure 29d.

G0.315-0.21 (g17)

This $4.5\mu\text{m}$ excess source lies in the vicinity of two stellar cluster candidates that are located within one arc-minute of each other and within the Sh2-20 HII region (Sharpless 1959; Dutra et al. 2003). This cluster also has variable X-ray emission, indicating very young stars (Law & Yusef-Zadeh 2004). Figures 30a,b show contours at $450\mu\text{m}$ and $850\mu\text{m}$ superimposed on a grayscale $24\mu\text{m}$ and 20cm images of this HII region. Two sources in the $24\mu\text{m}$ and 20cm images lie in the vicinity of a submillimeter peak. Contours of $4.5\mu\text{m}$ emission from both the northern and southern sources are shown in Figure 30c. The $4.5\mu\text{m}$ excess source coincides with the southern component of the emission shown in these figures. The presence of methanol masers coincident with the $4.5\mu\text{m}$ excess source and a bright submillimeter peak provide strong evidence for massive star formation in this region. The fit to the SED of the $4.5\mu\text{m}$ excess source is also consistent with $12.8 M_{\odot}$ protostar.

G0.167-0.445 (g18), G0.091-0.663 (g19) & G0.084-0.642 (g20)

The $4.5\mu\text{m}$ excess sources g18, g19 and g20 are projected toward the HII region RCW 141, which is centered near $l=0.3^{\circ}$, $b=-0.2^{\circ}$ with an extent of $6' \times 4'$. Figures 31a,b show $8\mu\text{m}$ and 20cm grayscale images of g18, respectively. The two $8\mu\text{m}$ sources appear to be embedded within an IRDC. However, the one indicated by a cross shows strong excess emission at $4.5\mu\text{m}$. A nonthermal radio filament that runs perpendicular to the Galactic plane is projected against the $4.5\mu\text{m}$ excess source. Figures 32a,b show grayscale $24\mu\text{m}$ and $8\mu\text{m}$ images of g19 and g20, respectively. It is clear that the southern source g19 is embedded in an IRDC. Figure 32c shows that neither of these $4.5\mu\text{m}$ excess sources has 20cm continuum counterparts. Figures 32d,e show contours of $4.5\mu\text{m}$ emission from g19 and g20, respectively.

G359.939+0.170 (g22)

The $4.5\mu\text{m}$ excess source g22 is located in an HII complex with an IRDC and a prominent $8\mu\text{m}$ nebulosity. Figures 33a,b show contours of $850\mu\text{m}$ emission superimposed on grayscale images at $24\mu\text{m}$ and 20cm, respectively. The $850\mu\text{m}$ emission and the IRDC at $24\mu\text{m}$ appear to lie at the edge of the nonthermal filament, as seen in Figure 33b. A large-scale view of the dark cloud and the extensive $8\mu\text{m}$ emission to its eastern edge are shown in Figure 33c. Contours of the source responsible for excess $4.5\mu\text{m}$ emission are shown in Figure 33d.

G359.972-0.459 (g21), G359.907-0.303 (g24) & G359.618-0.245 (g26)

The $4.5\mu\text{m}$ excess sources g21, g24 and g26 are distributed in the vicinity of RCW 137 which

is roughly centered close to $l=0.1^\circ$, $b=-0.3^\circ$ with an extent of $2' \times 2'$. The most interesting of these $4.5\mu\text{m}$ excess sources is g26, which is embedded in a prominent submillimeter core tracing an IRDC. Figures 34a,b show contours of $450\mu\text{m}$ and $850\mu\text{m}$ emission superimposed on $8\mu\text{m}$ and 20cm grayscale images of the IRDC associated with g26. The submillimeter cone-shaped structure peaks where methanol maser emission is detected. The closeness of methanol masers, the $4.5\mu\text{m}$ excess source and the submillimeter core support the evidence for massive star formation in this cloud. Figure 34c shows contours of $4.5\mu\text{m}$ emission from g26, which has an estimated $7 M_\odot$ protostar (see Table 10).

G359.57-0.27 (g28)

The $4.5\mu\text{m}$ excess source g28 lies at the edge of an IRDC that extends for $2'$. Images of the region at 24 and $8\mu\text{m}$ are shown in Figures 35a,b. g28 is located in the darkest area of the IR dark cloud, which shows an east-west elongation. The source was also detected at $70\mu\text{m}$, which allows us to constrain the mass of the YSO candidate to be $4 M_\odot$ assuming an $\langle A_v \rangle = 4$. Contours of $4.5\mu\text{m}$ emission are shown Figure 35c.

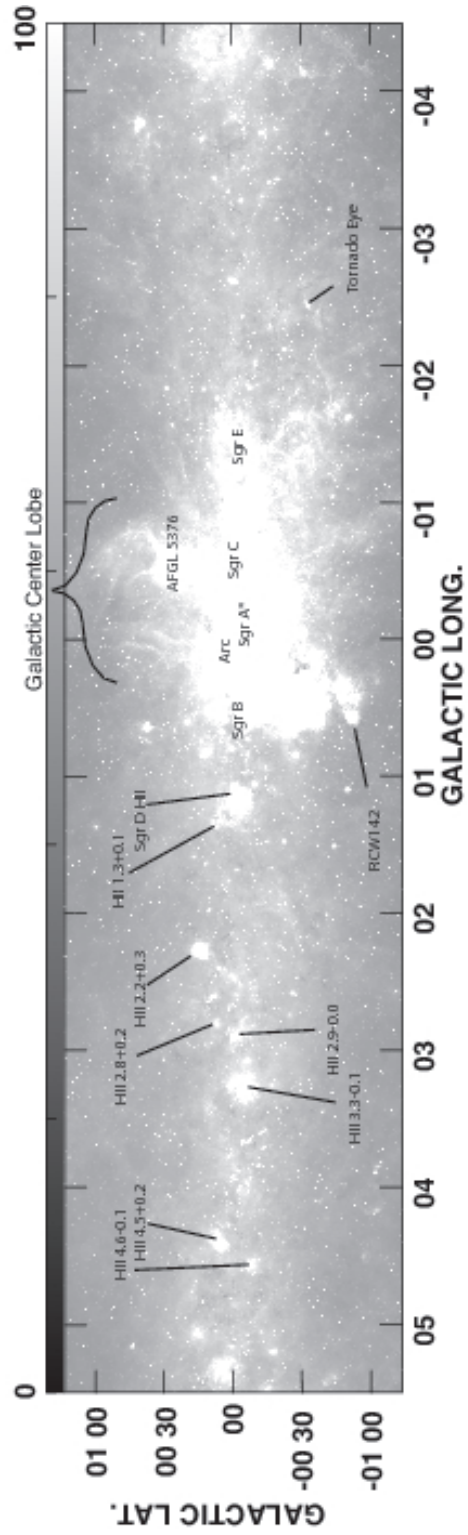


Fig. 1.— (a) A $24\mu\text{m}$ image of the inner $\sim 10^0 \times 2.5^0 (l \times b)$ of the central region of the Galaxy based on combining MIPS and MSX data.

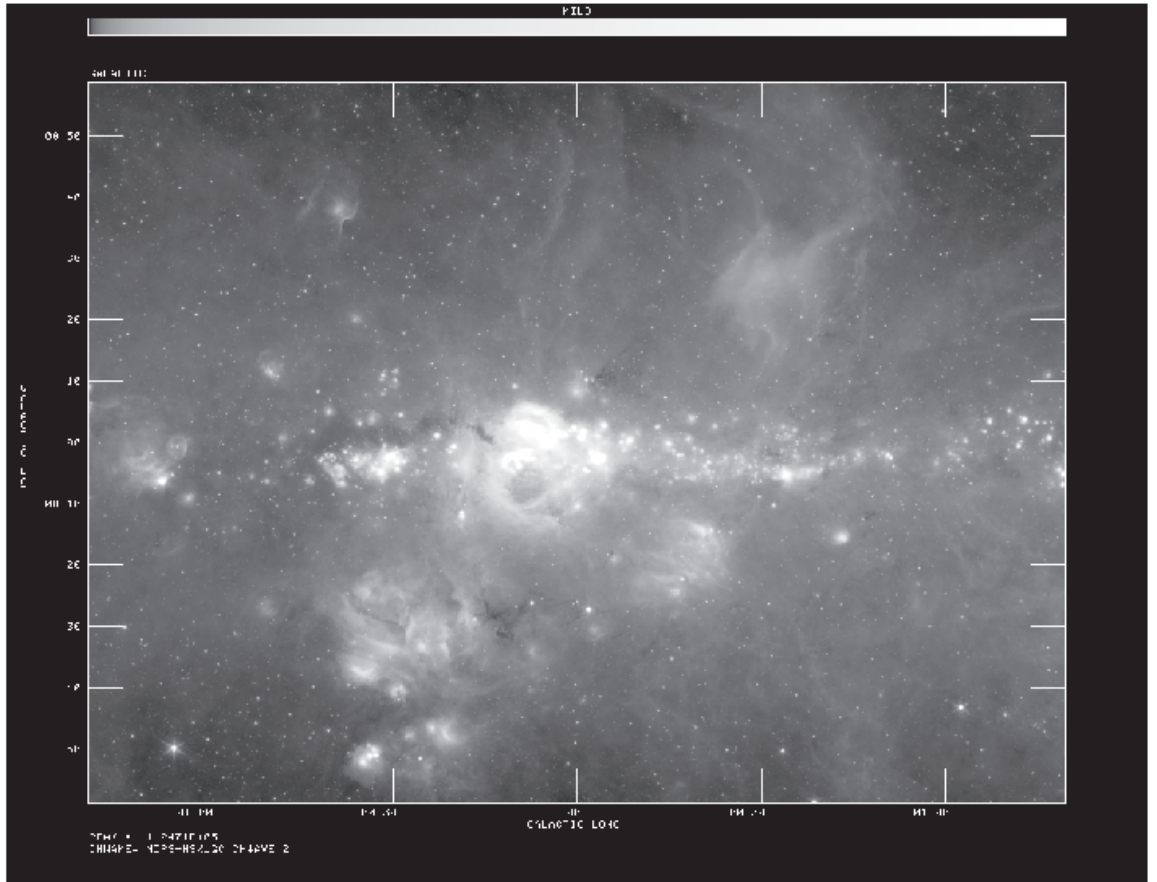


Fig. 1.— (b) A close-up view of the central $2.5^{\circ} \times 2^{\circ}$ showing the prominent HII complexes (Sgr A – E) at $24\mu\text{m}$,

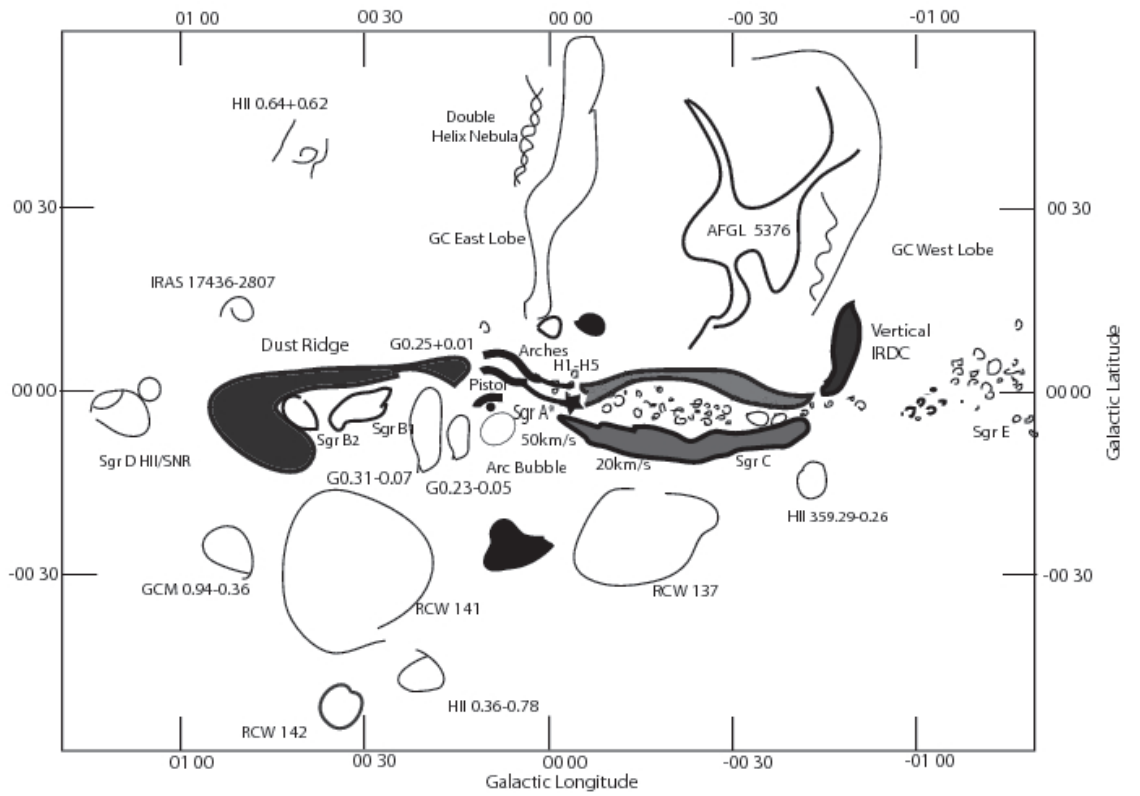


Fig. 1.— (c) A schematic diagram of prominent features detected at $24\mu\text{m}$ from the region shown in (b).

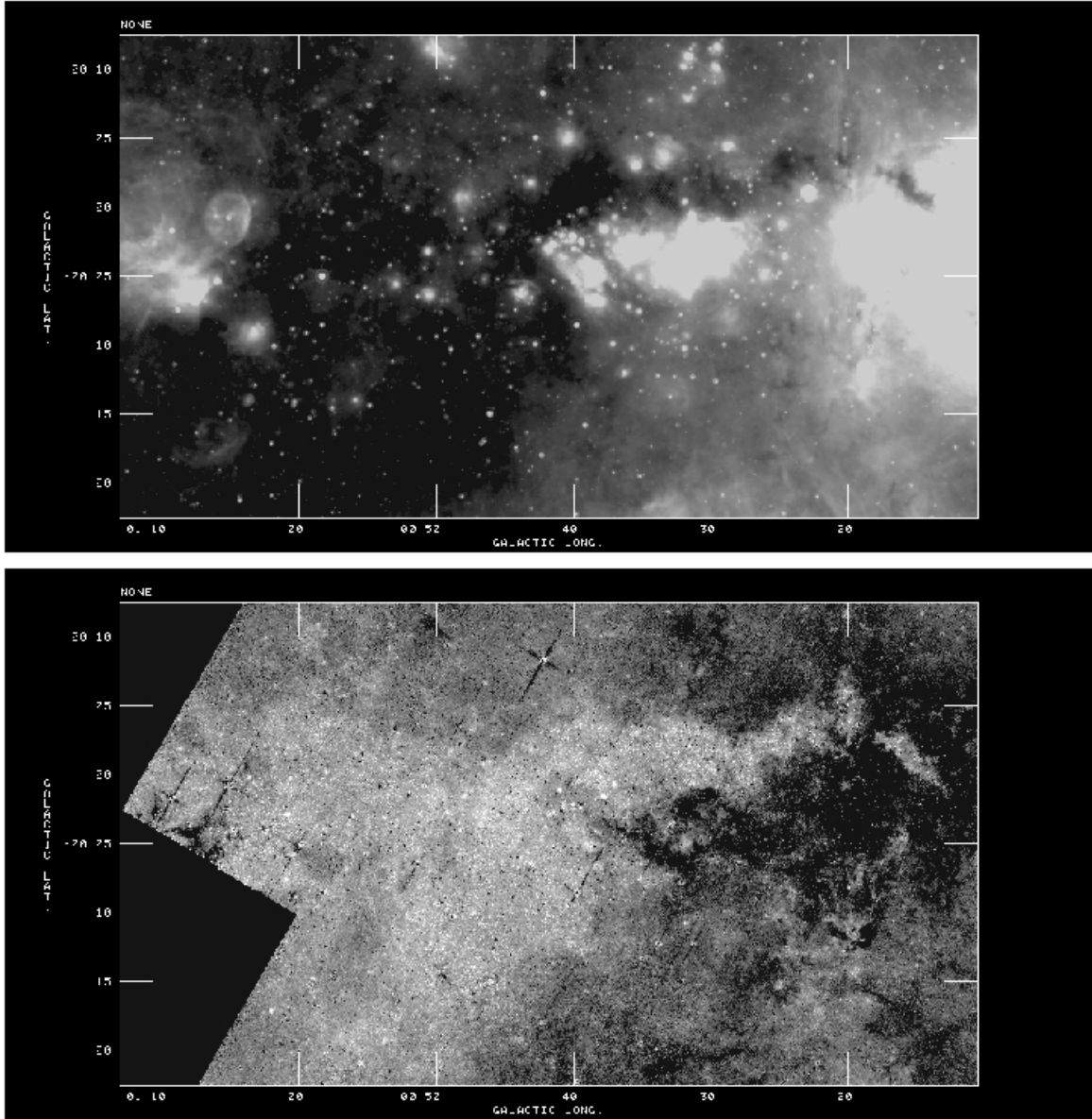


Fig. 2.—: (a - Top) $24\mu\text{m}$ emission from prominent chain of IRDCs on the positive longitude side of the Galactic center. The thickest cloud surrounds Sgr B2 to the left near $l=0.7^\circ$. (b - Bottom) Identical to (a) except that the ratio of IRAC images is displayed. Positive values of this ratio are shown in light color which reveals low contrast features of the IRDCs. The ratio image is constructed by $I(4.5)/[I(3.6)^{1.4} * I(5.8)]^{0.5}$.

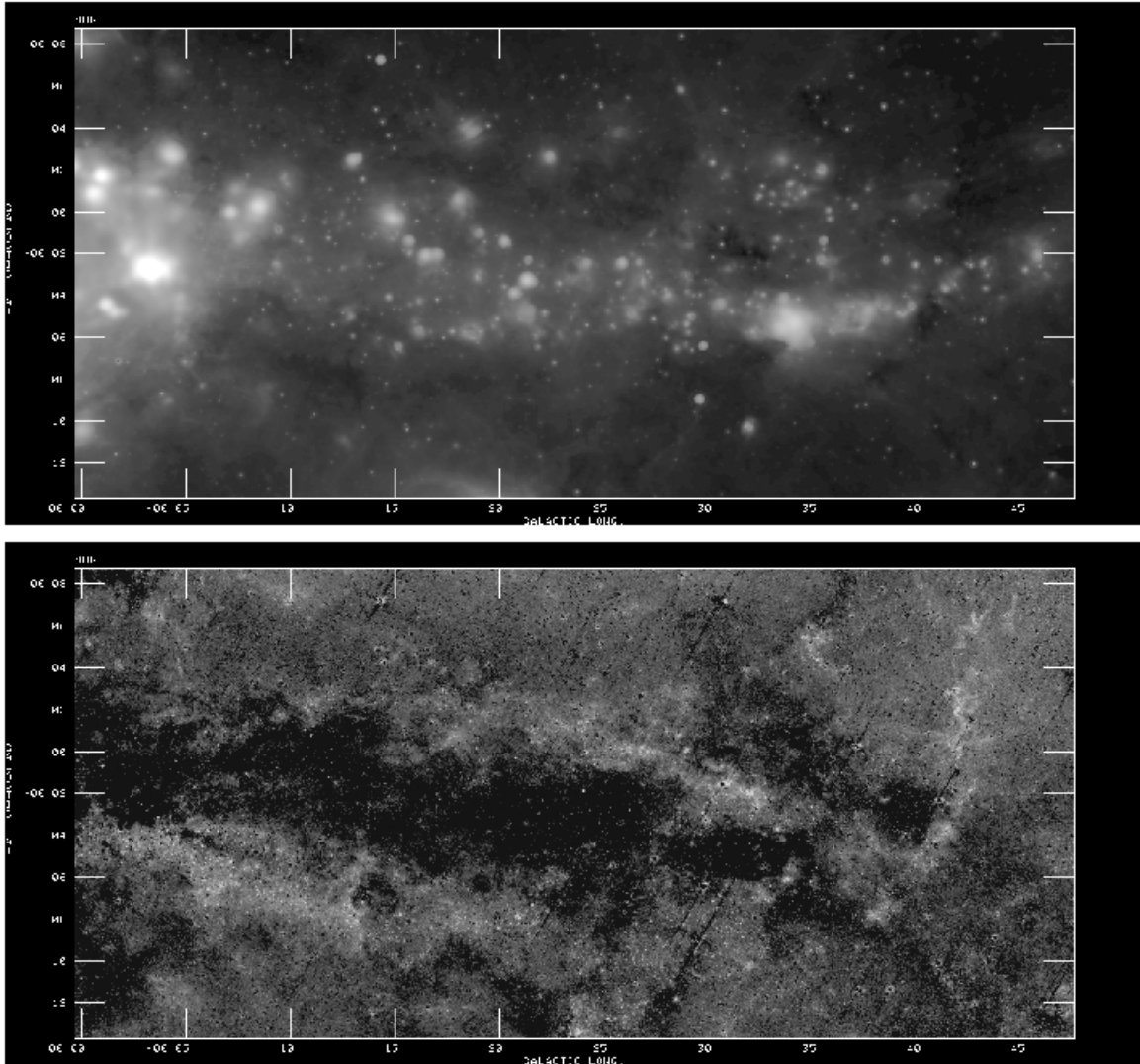


Fig. 3.— (*a - Top*) Similar to Figure 2a except that $24\mu\text{m}$ distribution from the negative longitude side is selected. Note the distribution of stellar objects along the Galactic plane. (*b - Bottom*) As in Figure 2b regions with higher intensity ratios reveal details in the structure of IRDCs. Most of the stellar sources seen in (a) are mainly distributed between the two extended IRDCs running parallel to the Galactic plane.

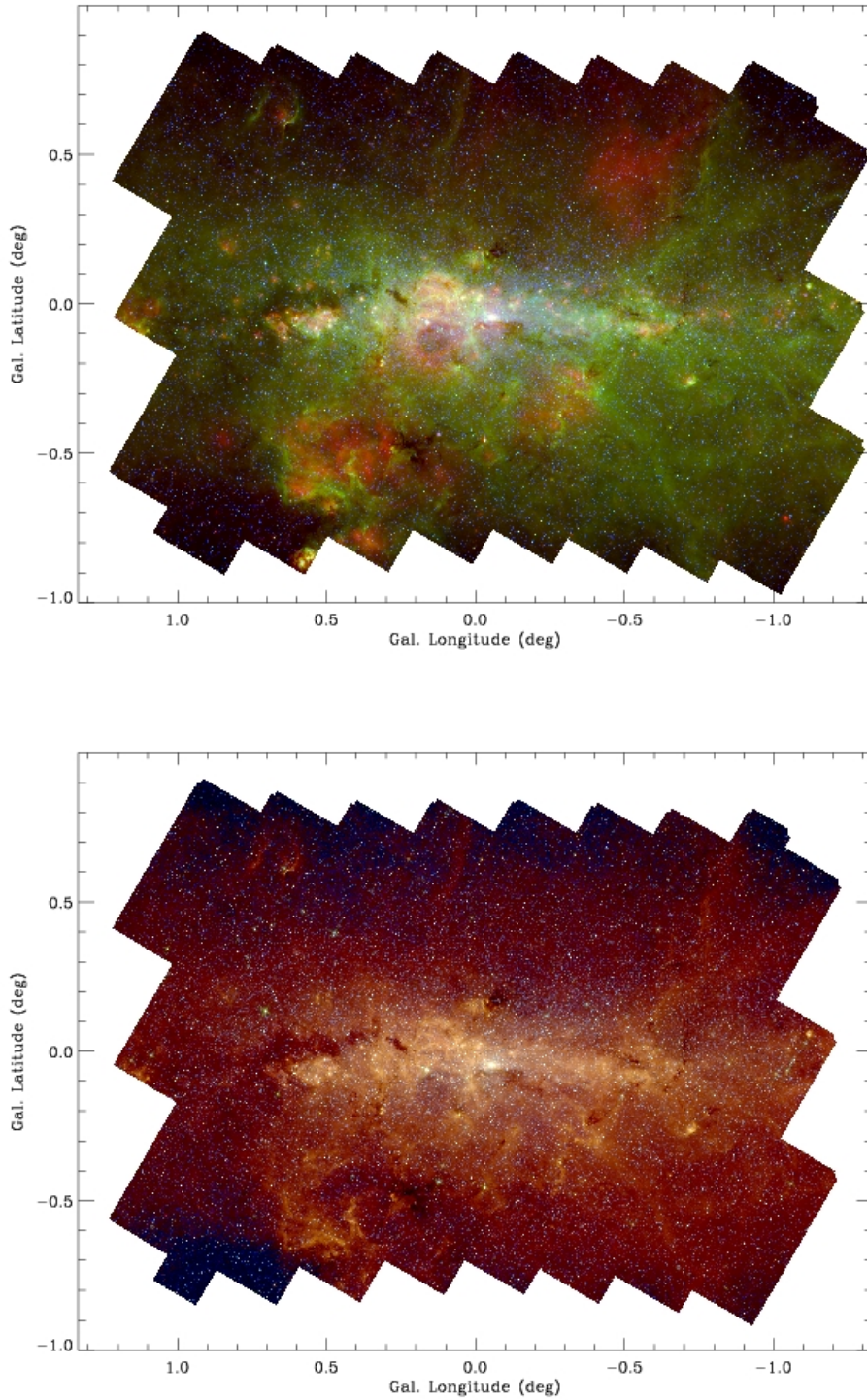


Fig. 4.— (a - Top) Color images of the 24, 8 and $3.6\mu\text{m}$ emission from the central $2^0 \times 1.4^0$ are shown in red, green and blue colors, respectively. The diffuse clouds peaking at $24\mu\text{m}$ are centrally heated whereas the emission in green color is mainly due to PAHs in photodissociation regions. (b - Bottom) Similar to (a) except that the 4.5, 5.8 and $8\mu\text{m}$ images are shown in blue, green and red colors, respectively.

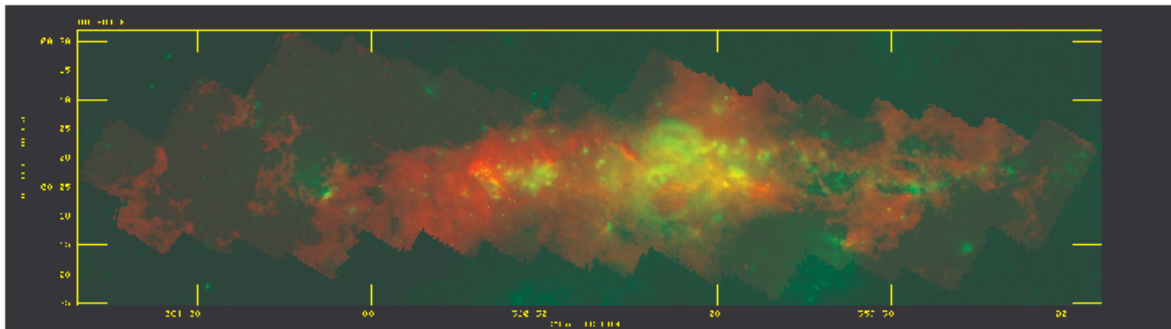
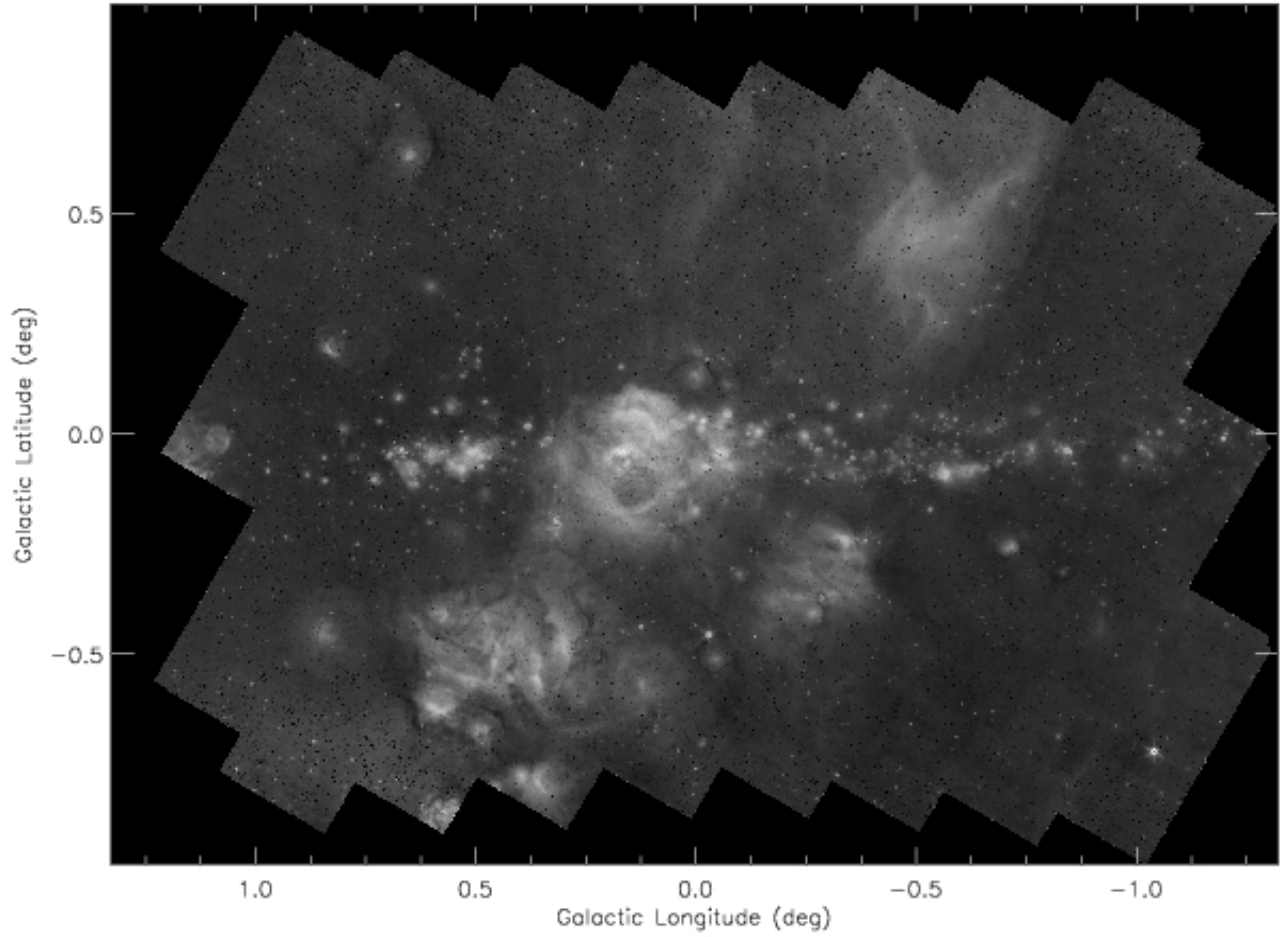


Fig. 5.— (a - Top) A large-scale grayscale ratio image $I(24\mu\text{m})/I(8\mu\text{m})$ shows the bright region to be mainly due to $24\mu\text{m}$ emission whereas dark region shows the region dominated by $8\mu\text{m}$ emission. Note that the dark regions in this ratio image do *not* represent the IRDCs. (b - Bottom) The distribution of $24\mu\text{m}$ emission in green color is shown against the distribution of $450\mu\text{m}$ emission (Pierce-Price et al. 2000) in red color.

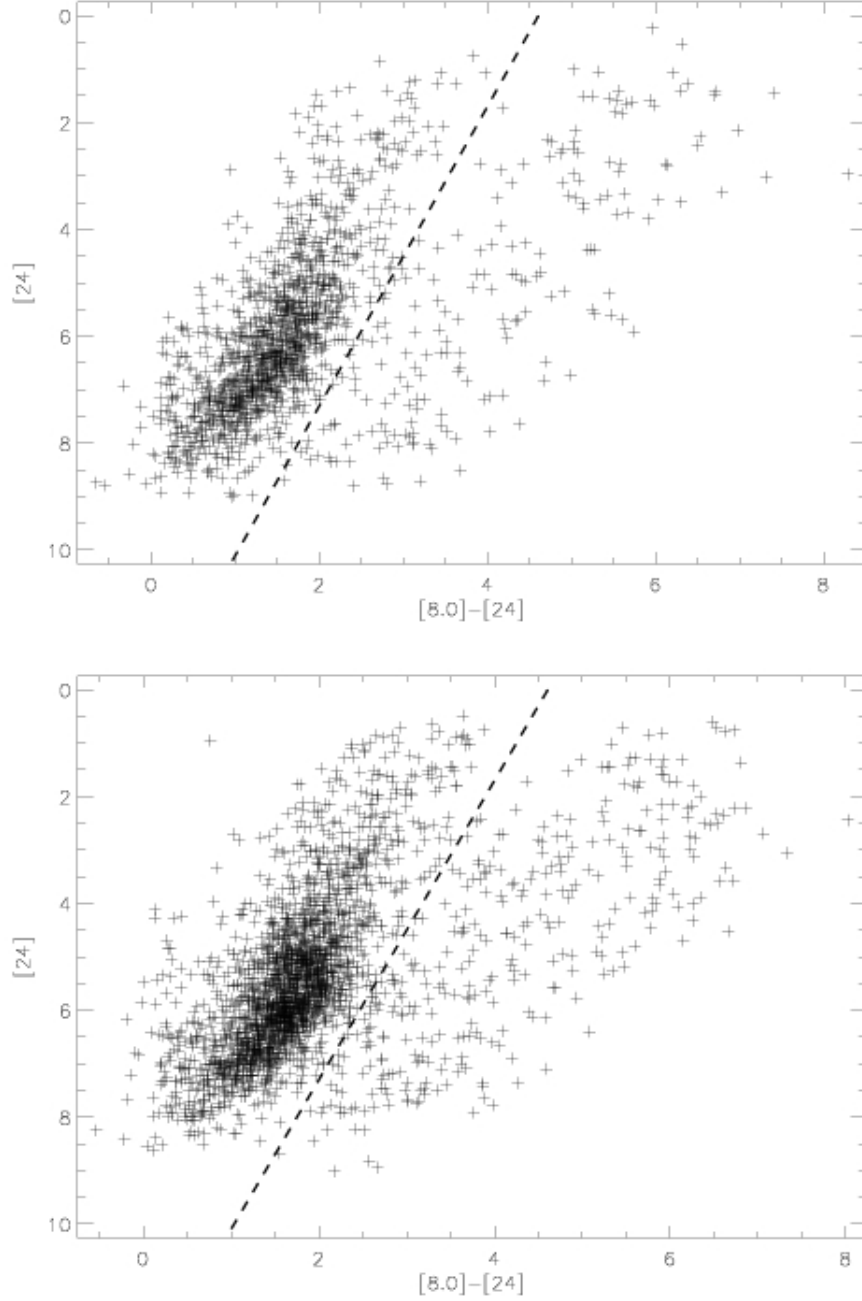


Fig. 6.—: (a - Top) The color magnitude diagram of $24\mu\text{m}$ sources covers the region $b \pm 10'$ and $0 < l < 1.4^\circ$. The dashed line is an empirical separator between evolved AGB stars (to the left) and candidate YSOs to the right. (b - Bottom) Similar to (a) except that the search area includes $-1.4^\circ < l < 0$.

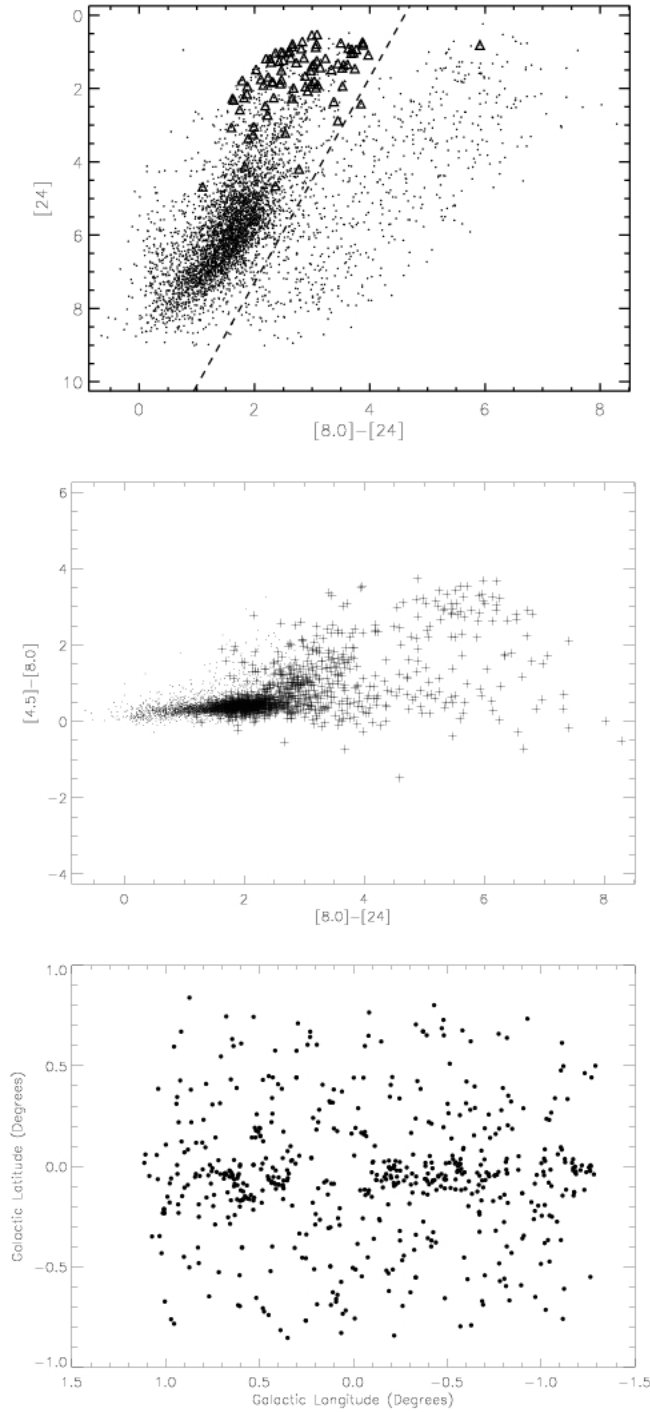


Fig. 7.—: (*a - Top*) The color magnitude diagram of the region covering $-10' < b < 10'$ and $-1.4^\circ < l < 1.4^\circ$. The triangles show the locations of known OH/IR stars within the region. The dashed line is drawn to separate the OH/IR stars from candidate YSOs with redder colors. A total of 4,541 sources is plotted as dots in the CMD. (*b - Middle*) Color color magnitude diagram of the region covered in (a). The crosses show the location of candidate YSOs identified in (a). (*c - Bottom*) The spatial distribution of $24\mu\text{m}$ sources. The central hole centered on Sgr A is due to MIPS saturation at this wavelength.

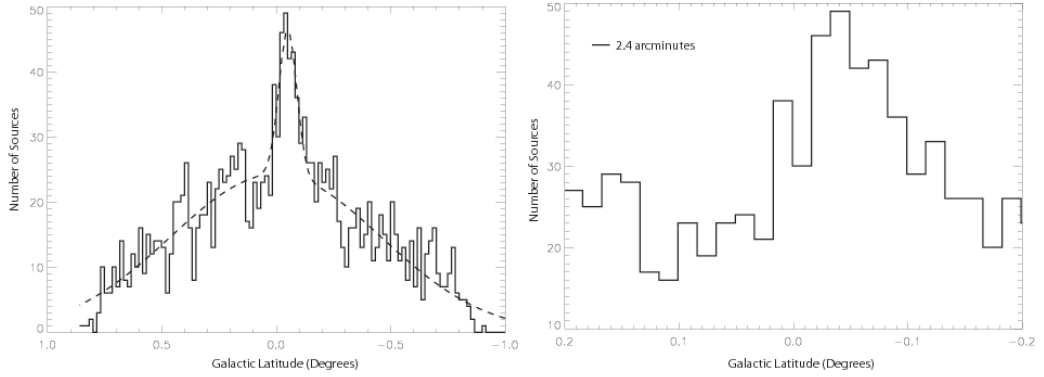


Fig. 8.—: (a - Left) The histogram of YSO candidates as a function of latitude for the central $|l| < 1.3^\circ$ shows two components, which were fit by Gaussians. The broad component is centered near $b \sim 0.0^\circ$ with a FWHM of $64'$ whereas the narrow component is centered at $b = -3'$ with a FWHM of $\sim 5.5'$. Each bin is $1'$. (b - Right) The distribution of YSOs with Galactic latitude for the same region as (a) but over the region $|b| < 0.2^\circ$. The units of latitude are degrees. The latitude of Sgr A* is $b = -2'46.2''$.

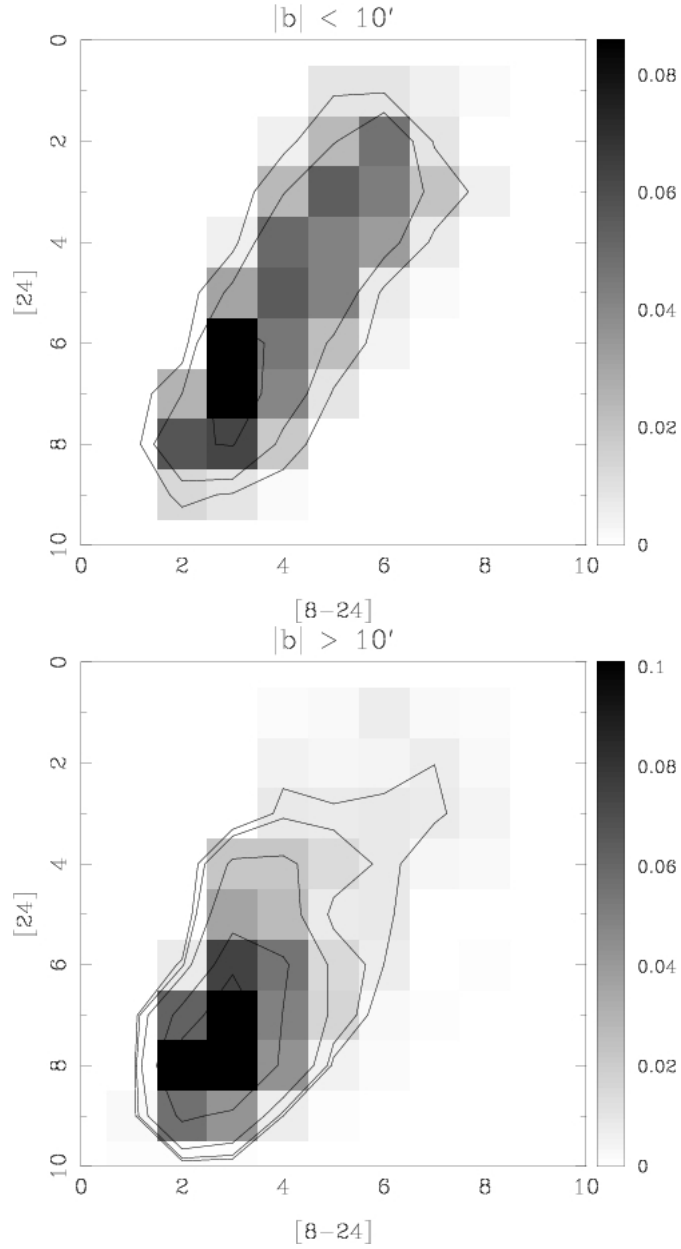


Fig. 8.— The YSO candidates for the inner region (*c - Top*) and the outer region (*d Bottom*) binned the sources in both $[8]-[24]$ color and $[24]$ magnitude with a bin size of 1 magnitude. The number of YSO candidates in each bin is then divided by the total number of YSO candidates in the region to give a measure of the color-magnitude properties of the YSO candidates. Contour levels of 0.1, 0.25 and 0.6 for (c) and 0.007, 0.01, 0.05 and 0.08 for (d) are also drawn. It is clear that there is a higher fraction of brighter, redder YSO candidates in the innermost region of the Galactic center when compared to outside sources.

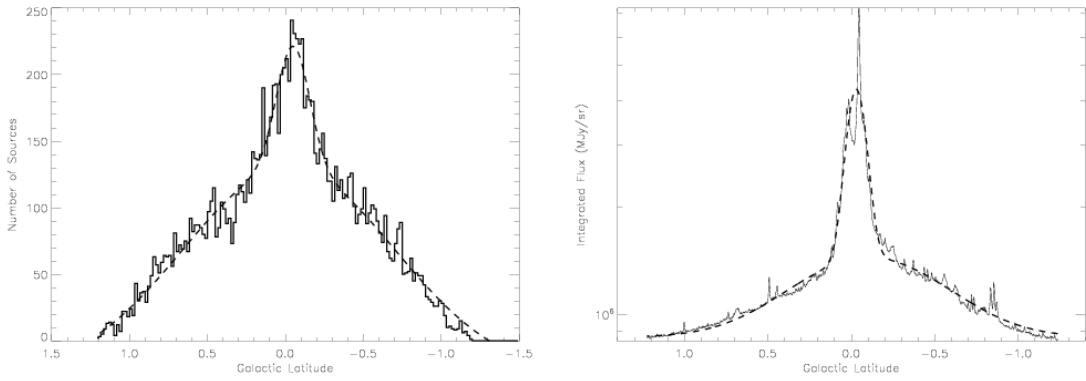


Fig. 9.—: (a - Left) The distribution of unsaturated MIPS $24\mu\text{m}$ point sources brighter than 5 magnitudes, binned as a function of Galactic latitude. Each bin is $0.1'$. The distribution can be decomposed into two Gaussian components, a narrow and a broad component with FWHM of $15'$ and $96'$, respectively. (b - Right) The total brightness distribution of $24\mu\text{m}$ emission as a function of latitude based on the combined MIPS and MSX image using $|l| < 4^\circ$. The units of latitude are degrees.

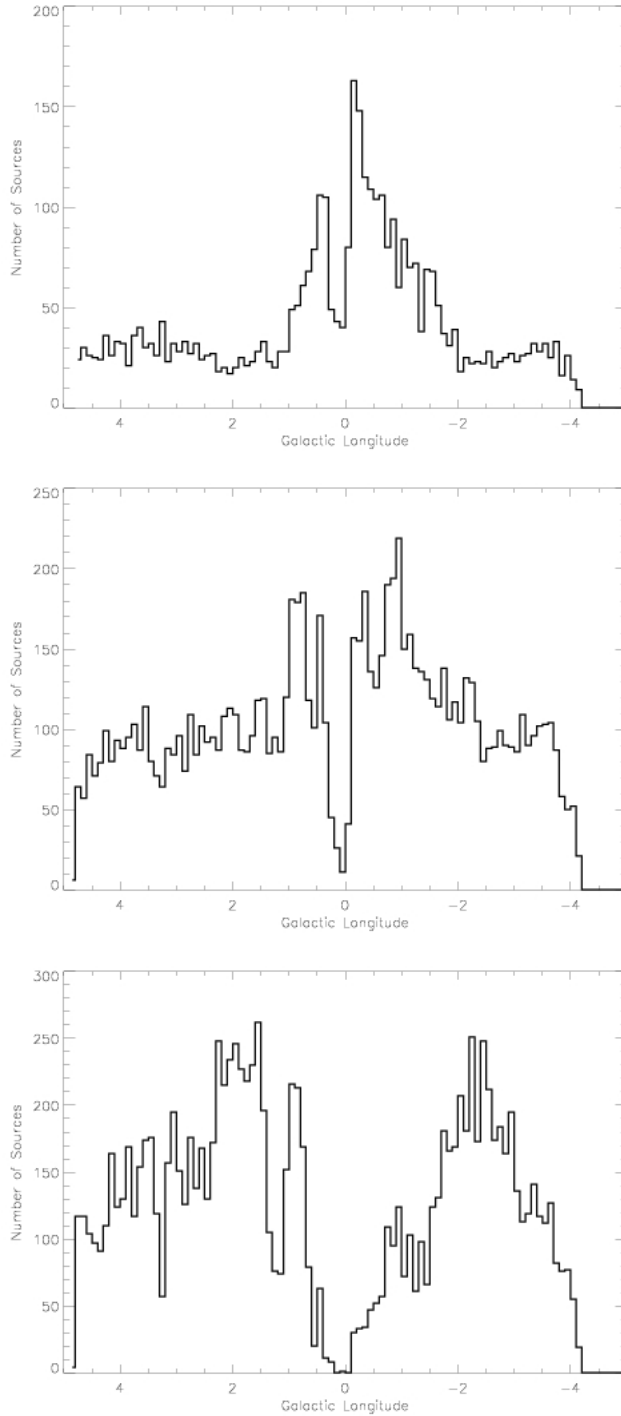


Fig. 10.—: (a - Top) The brightness distribution of $24\mu\text{m}$ point sources as a function of longitudes in shown for $24\mu\text{m}$ sources ranging between 0 and 5 magnitudes. (b - Middle) The middle panel shows the distribution of point sources with intermediate brightness between 5 and 7 magnitudes. (c - Bottom) Similar to the middle panel except for faint sources between 7 and 10 magnitudes. All the plots have used the entire region of the $24\mu\text{m}$ survey but restricted the latitudes to within $b=\pm 10'$. The dips in the distribution near $l = 0^\circ$ are largely caused by the inability to detect faint sources in regions where $24\mu\text{m}$ emission is extremely bright. The units of longitude are degrees.

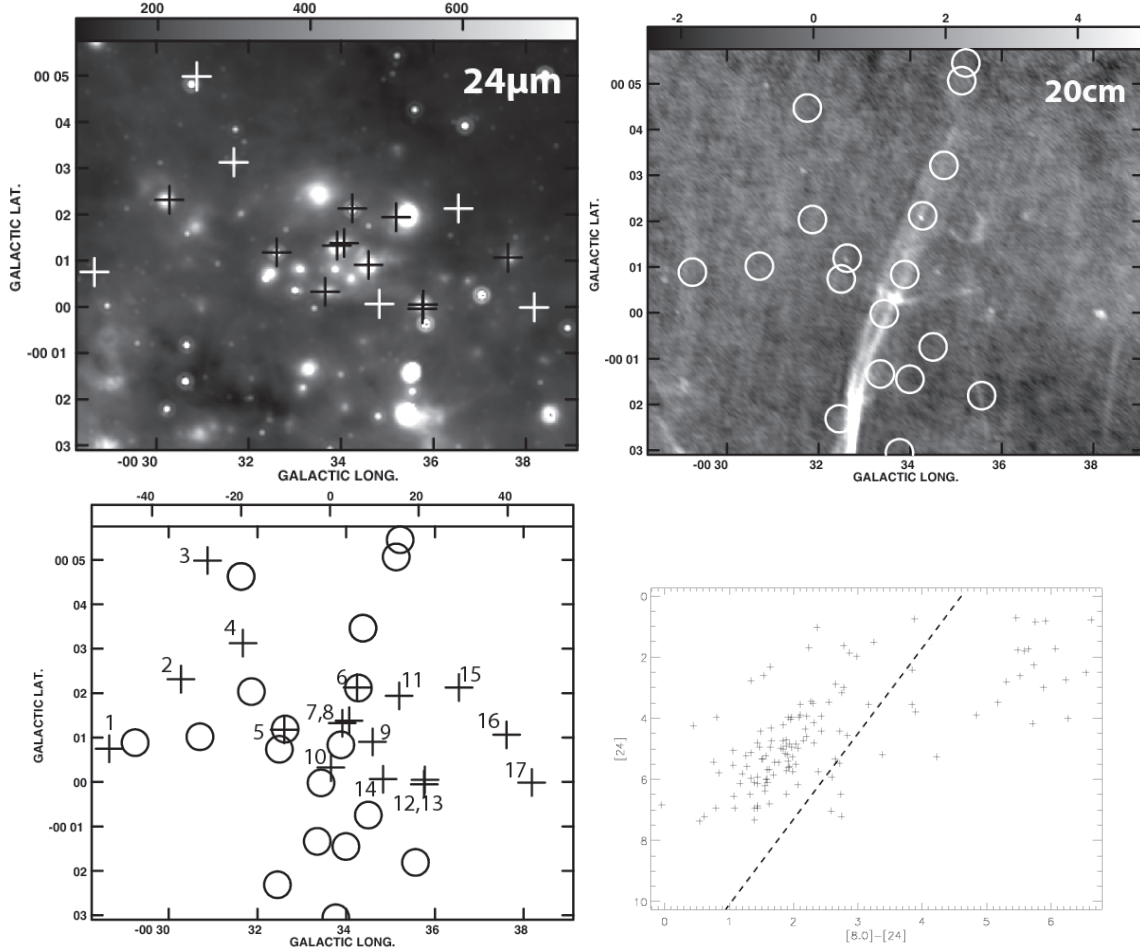


Fig. 11.—: (a - Top Left) A grayscale $24\mu\text{m}$ image of the G359.43+0.02 stellar cluster. (b - Top Right) A grayscale 20cm continuum image with a resolution of $12'' \times 12''$ with an identical size to that shown in (a). (c - Bottom Left) A finding chart of YSO candidate sources and radio continuum sources in the region shown in (a) and (b). (d - Bottom Right) A plot of the CMD of the infrared sources found in (a). A total of 18 candidate YSOs are selected from the area to the right of the plot. The crosses present the position of the compact radio sources as listed in Table 1 whereas the circles coincide with the position of unsaturated $24\mu\text{m}$ YSO candidate sources, as listed in Table 2.

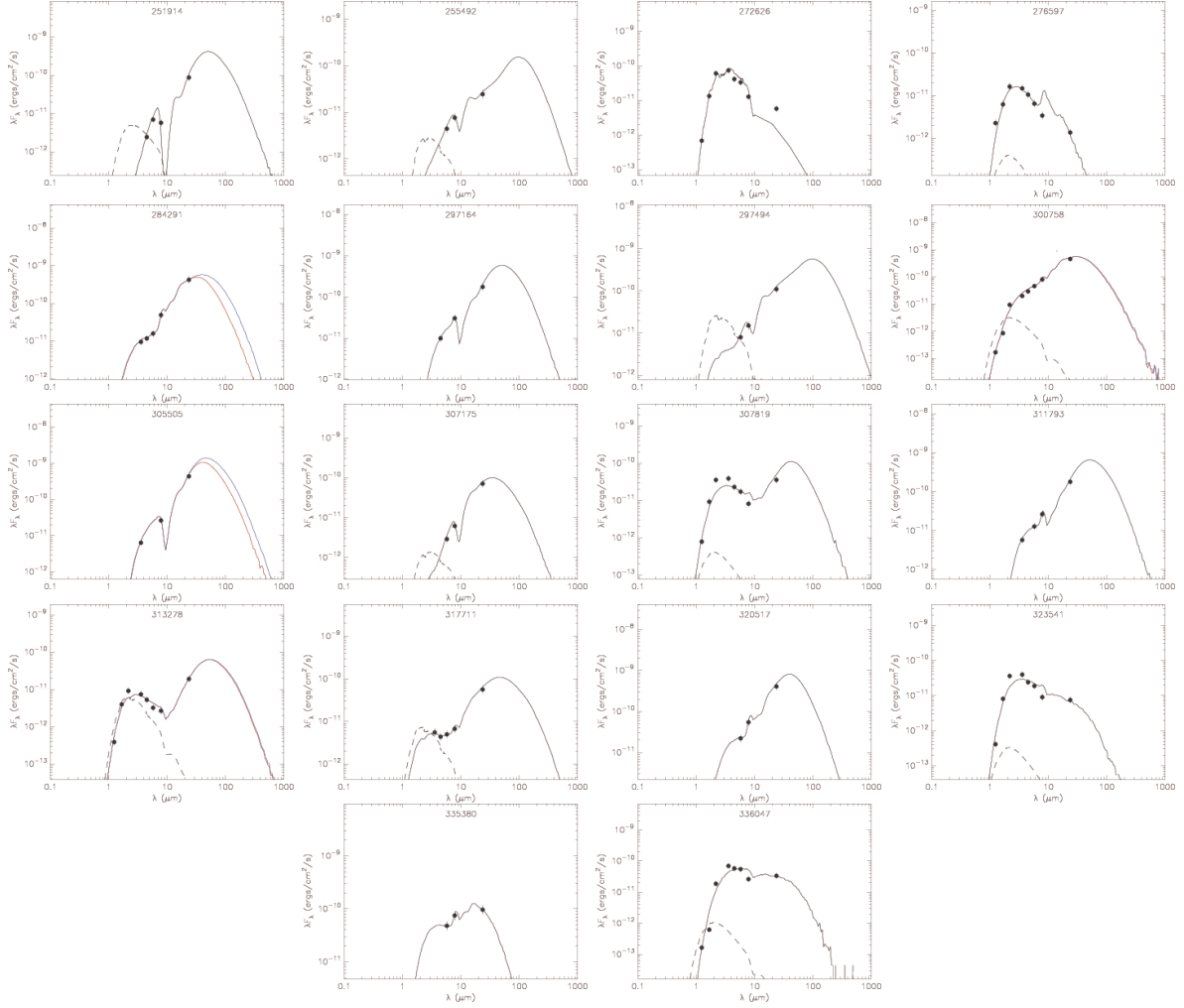


Fig. 12.—: (a) The SED fitted plots of 18 candidate YSOs found in the G359.43+0.02 cluster. The parameters of the fits are shown in Table 2.

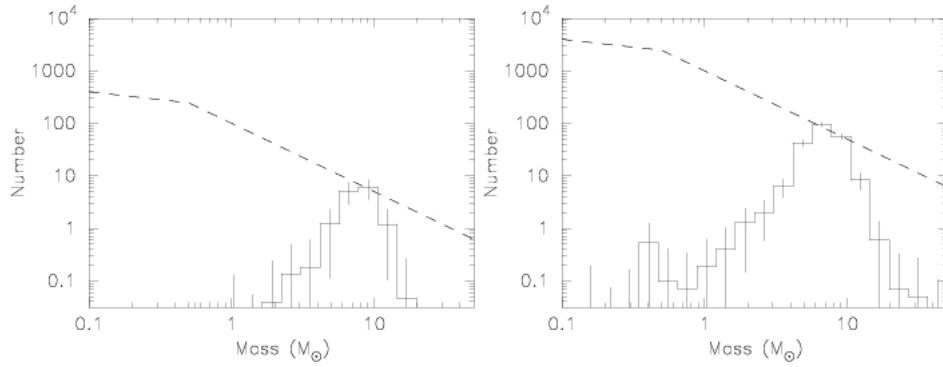


Fig. 12.—: (b *Left*) The histogram of the mass of YSO candidates for the cluster G359.43+0.02. (c *Right*) Similar to (b) except for all the YSO candidates distributed within the Galactic disk restricted to $|b| = 10'$ and $|l| < 1.3^{\circ}$. “Number” in both (a) and (b) represent all the good fits for a given source in the distribution and is normalized so that the sum equals the average mass which is given in Tables 2 to 4. Each source is represented by a distribution of well-fit masses. The broken power-law form is fitted to the data and is shown as dashed line in both (b) and (c).

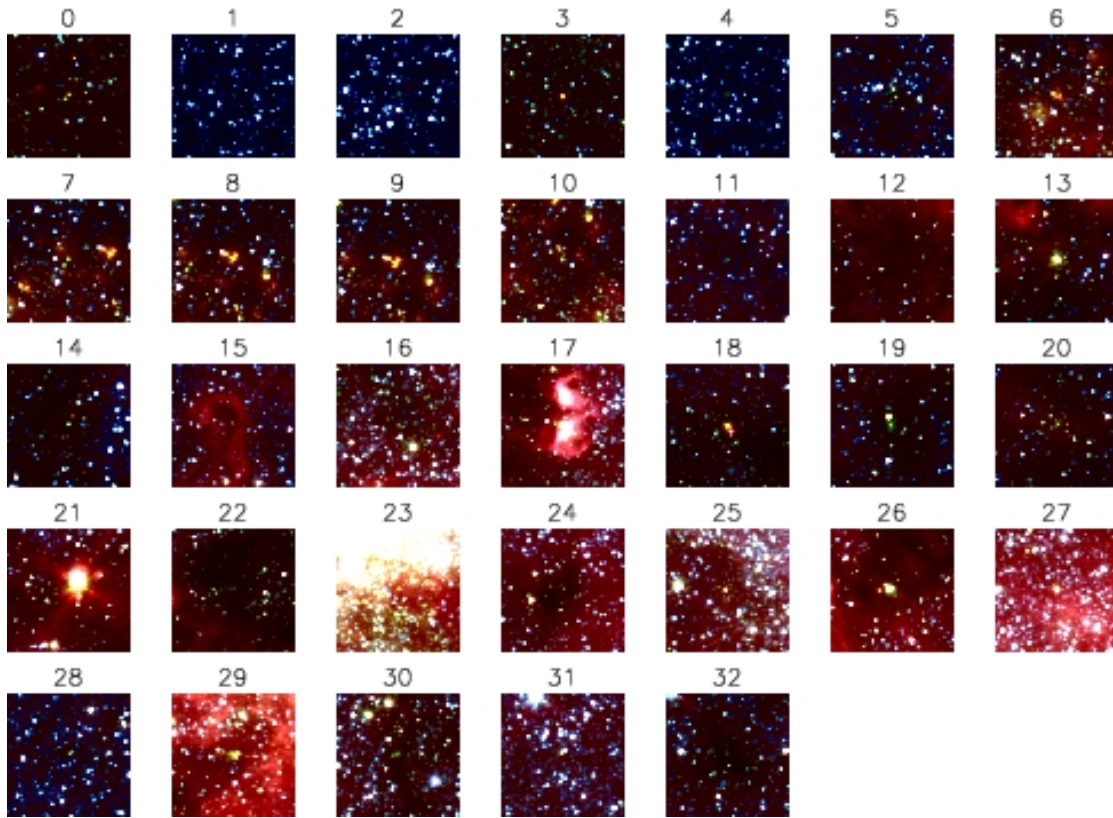


Fig. 13.— Color images of all the $4.5\ \mu\text{m}$ sources found in the IRAC survey region. Red, green, and blue colors denote 8, 4.5, and $3.6\ \mu\text{m}$ emission respectively. Each image shows a region of $7.5' \times 7.5'$ centered on the $4.5\ \mu\text{m}$ excess sources.

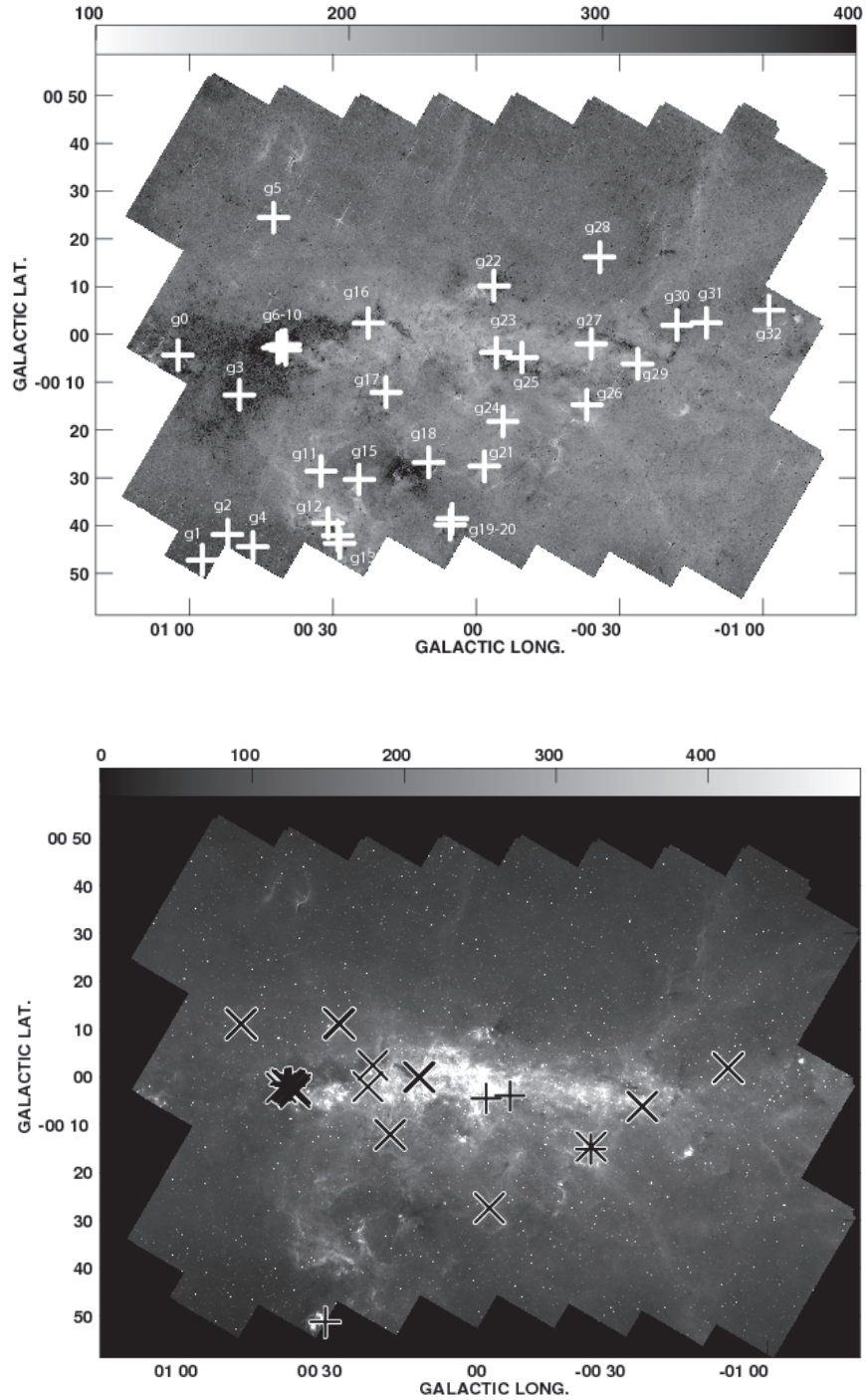


Fig. 14.—: (a - Top) The distribution of $4.5\mu\text{m}$ excess sources, presented as crosses, is superimposed on a ratio image constructed from $I(4.5)/[I(3.6)^{1.2} * I(5.8)]^{0.5}$. (b - Bottom) The distribution of class I and II methanol masers, shown as "+" and "x" signs, respectively is superimposed on an $8\mu\text{m}$ image.

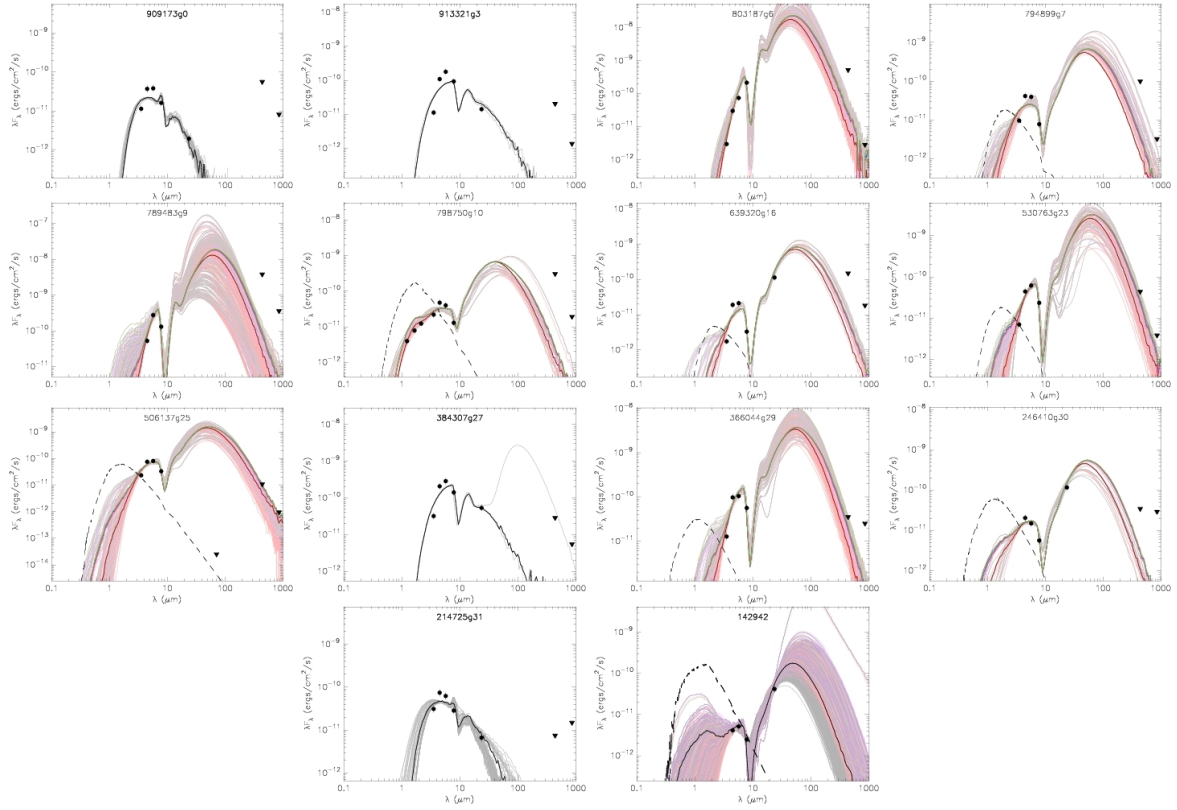


Fig. 15.—: (a) SED Fits to $4.5\mu\text{m}$ excess sources toward the Galactic center. The colored lines (reddish) correspond to fits made from different apertures. The grey lines are for IRAC sizes, and pink for $24\mu\text{m}$.

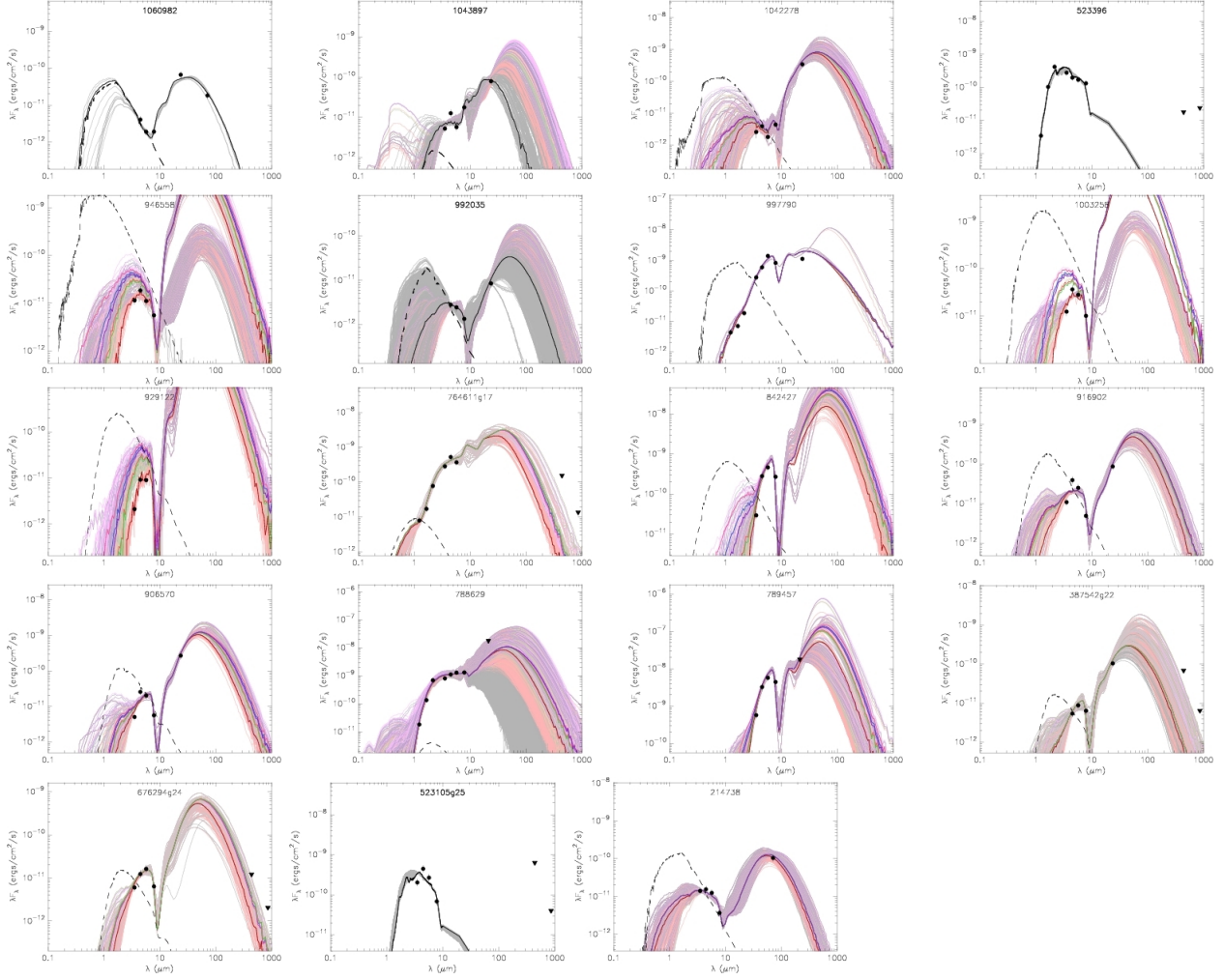


Fig. 15.— (b) SED Fits to foreground $4.5\mu\text{m}$ Excess Sources

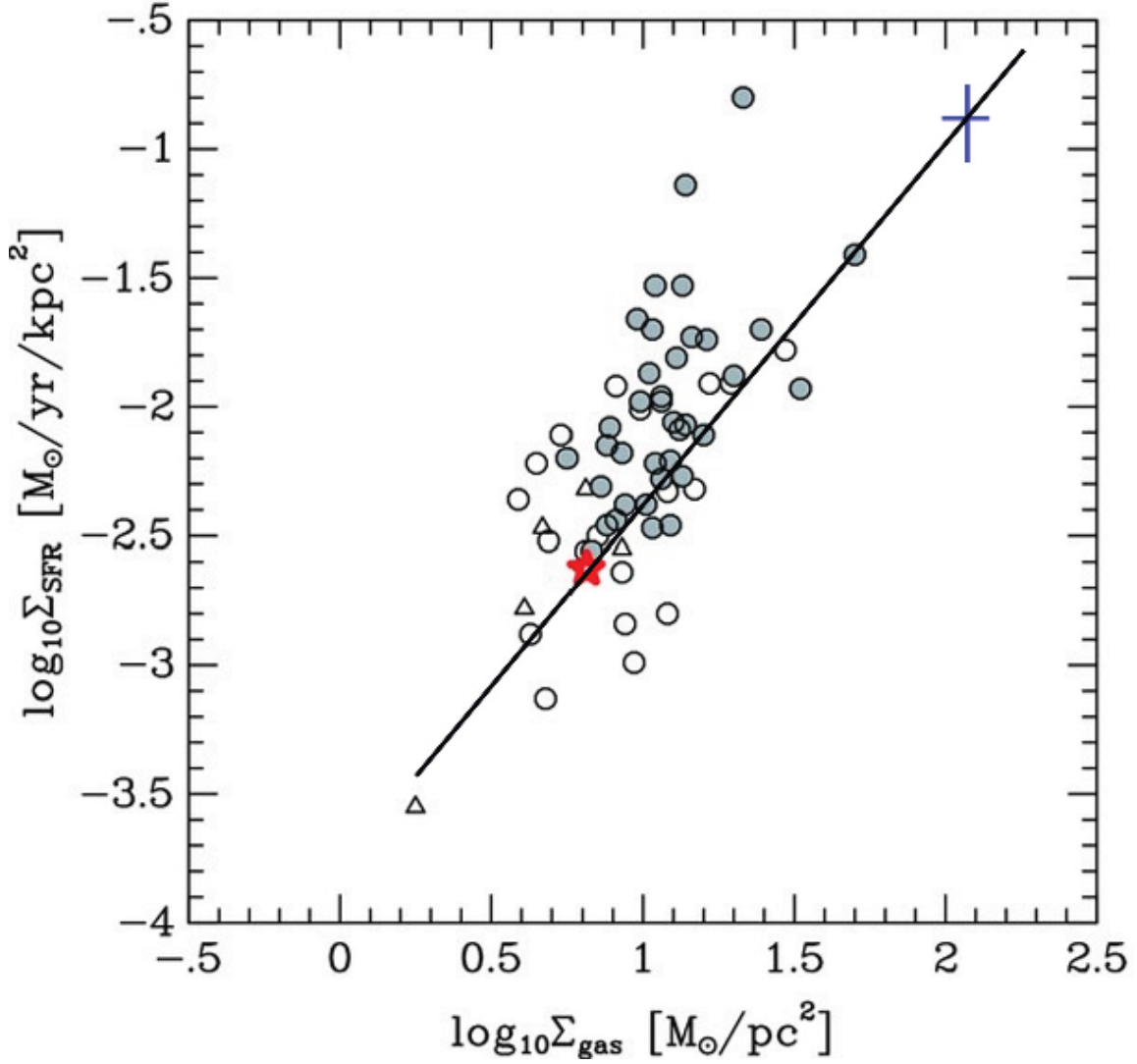


Fig. 16.—: The correlation of the SFR with the gas surface density (Fuchs et al. 2009; Kennicutt 1998). Sa-Sb galaxies are shown as open triangles, Sb-Sc as open circles, and Sc-Sd as filled circles. The red star is the value for the solar neighborhood and the blue cross is that for the Galactic center. The black line has a slope of 1.4, corresponding to the Schmidt-Kennicutt relationship found for external galaxies (Kennicutt 1998).

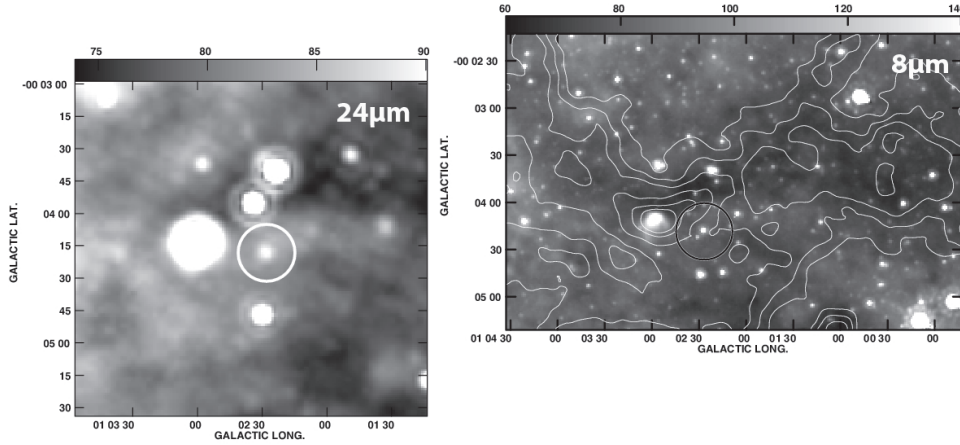


Fig. 17.—: (a - Left) A $24\mu\text{m}$ image of the $4.5\mu\text{m}$ excess source G1.041-0.072 (g0). The circle represents the position of the $4.5\mu\text{m}$ excess source which coincides with a $24\mu\text{m}$ source. (b - Right) Similar to (a) except that this $8\mu\text{m}$ image shows an segment of an IRDC ridge and g0. Contours of $850\mu\text{m}$ based on SCUBA observations are also superimposed on the figure. Levels are at 1.750, 2, 2.25, 2.5, 2.75, 3 and 4 Jy/beam. The circle marks the position of the $4.5\mu\text{m}$ excess sources whereas the square represents sources that are observed at $70\mu\text{m}$. The distribution of class I and II methanol masers are also drawn on these figures as plus(+) and cross (X) signs, respectively. These symbols apply for Figures 16-35.

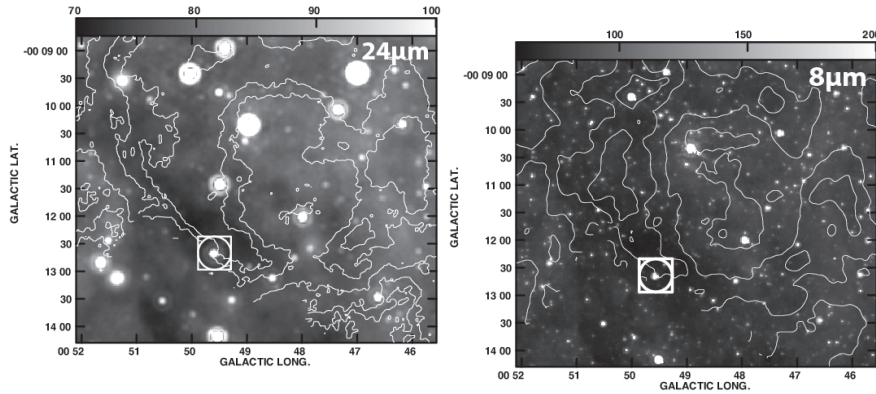


Fig. 17.—: (c - Left) Contours of $450\mu\text{m}$ emission are superimposed on a $24\mu\text{m}$ image of g3. The location of g3 is shown by a circle whereas the square sign shows the location at which $70\mu\text{m}$ observation was made. Levels at 6, 7, 9, 12, 14 and 20 Jy/beam. (d - Right) Similar to (a) except that contours of $850\mu\text{m}$ emission are superimposed on an $8\mu\text{m}$ image of g3. Levels at 2, 2.5, 3, 3.5, 4, 4.5 Jy/beam.

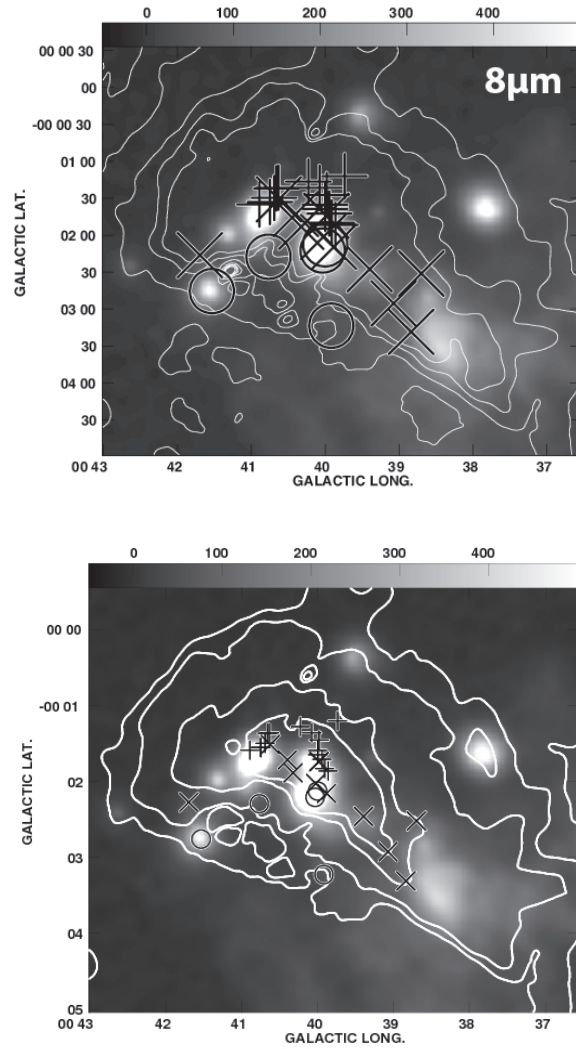


Fig. 18.—: (a - Top) Contours of $450\mu\text{m}$ emission superimposed on an $8\mu\text{m}$ image of Sgr B2. sources. Levels are at 35, 40, 50, 100, 200 and 400 Jy/beam. (b - Bottom) Similar to (a) except that $850\mu\text{m}$ contours are superimposed on a 20cm radio continuum image. Levels are at 6, 7.5, 15 and 25 Jy/beam. Symbols are as defined in Figure 17.

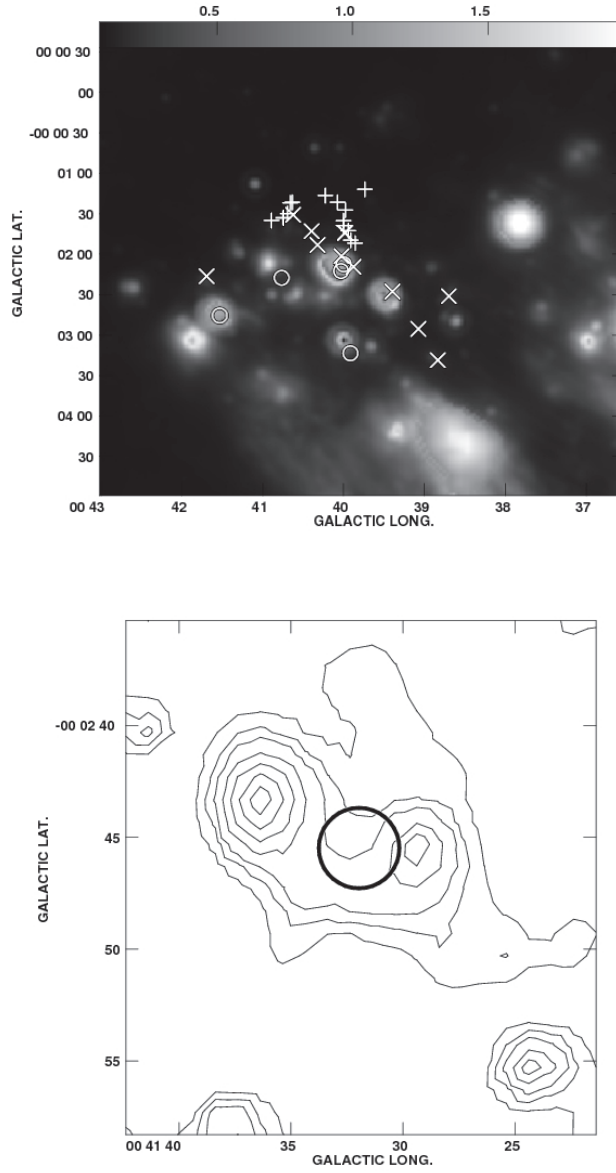


Fig. 18.—: (*c - Top*) A $24\mu\text{m}$ grayscale image of Sgr B2. (*d - Bottom*) Contours of $4.5\mu\text{m}$ emission from the $4.5\mu\text{m}$ excess source g6. Levels are at 25, 35, 50, 75, 100, 125 MJy sr^{-1} . Symbols are as defined in Figure 17.

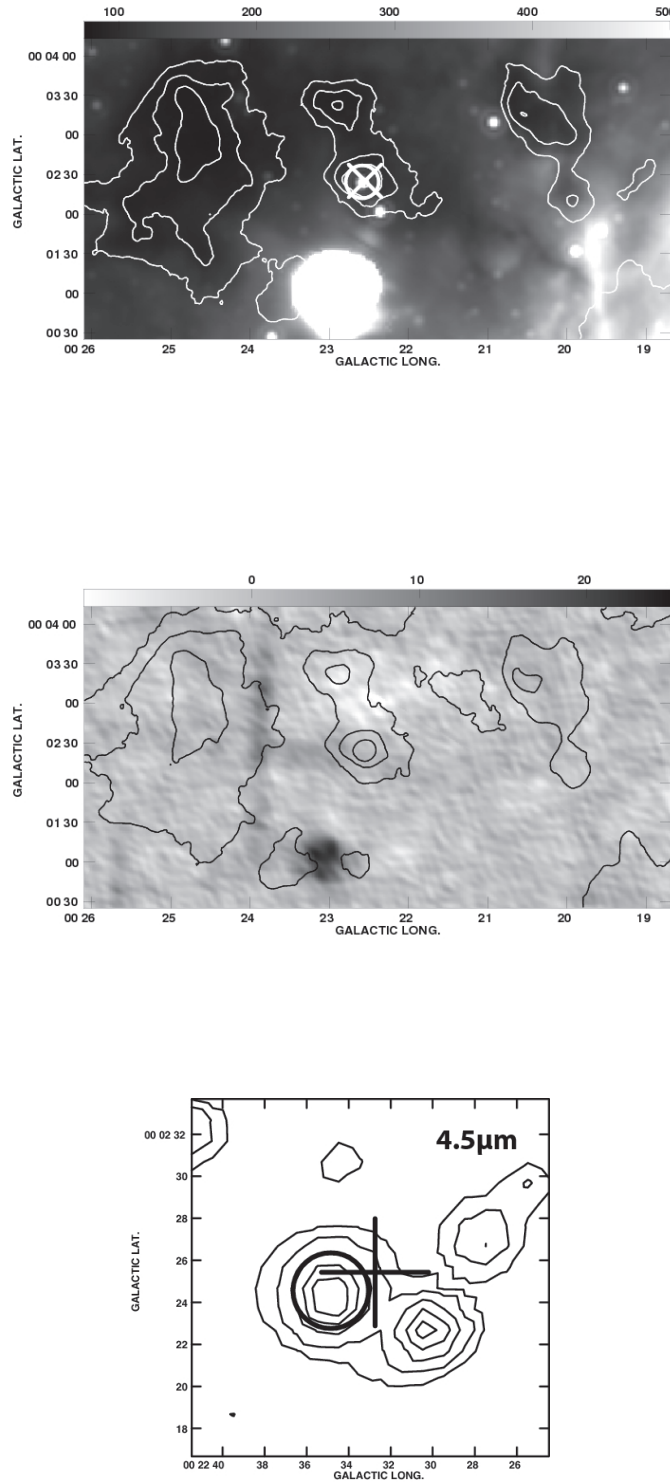


Fig. 19.—: (a - Top) Contours of 450 μm emission around g16 are superimposed on a 24 μm grayscale image. Levels are at 3, 4, 5.5 and 8 Jy/beam. (b - Middle) Similar to (a) except that contours of 850 μm emission are superimposed on a grayscale 90cm image. Levels are at 15, 20, 27.5 and 40 Jy/beam. (c - Bottom) A 4.5 μm contours of emission from the region where g16 is identified. Levels are at 20, 30, 50, 70, 90 and 110 MJy/sr. Symbols are as defined in Figure 17.

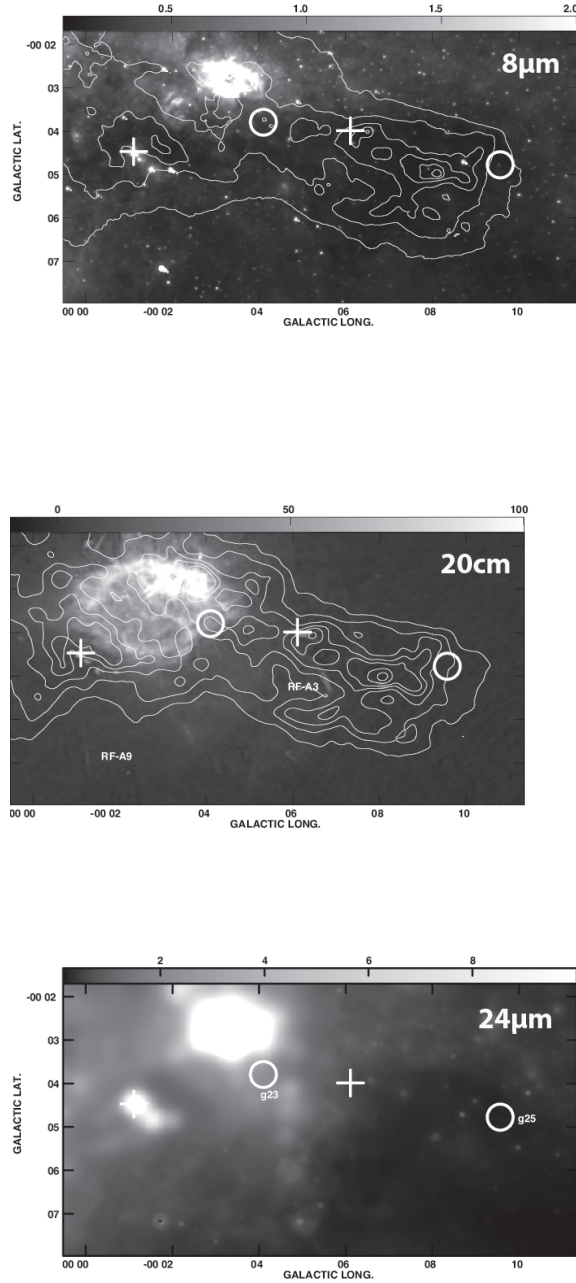


Fig. 20.—: (a *Top*) Contours of $450\mu\text{m}$ emission from the 50 and 20 km s^{-1} molecular clouds are superimposed on an $8\mu\text{m}$ image of this region. The circles show the positions of $4.5\mu\text{m}$ excess sources g23 and g25, projected toward the 50 km s^{-1} and 20 km s^{-1} molecular clouds, respectively. The plus signs shown the position of class I methanol sources in this region. (b - *Middle*) Similar to (a) except that contours of $850\mu\text{m}$ emission are superimposed on a radio continuum image at 20cm . Levels are at 4, 5, 6, 7, 8, 10, 12 and 14 Jy/beam (c - *Bottom*) A $24\mu\text{m}$ image of the Sgr A region based mainly on the saturated MIPS data that are replaced by MSX data. The IRDCs associated with the 50 and 20 km s^{-1} are best represented in this figure. Symbols are as defined in

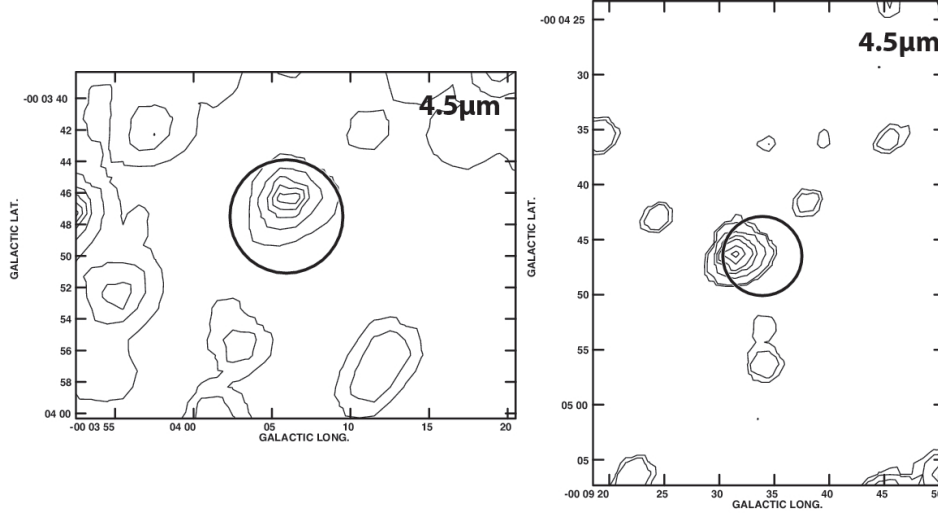


Fig. 20.—: (*d - Left*) Contours of $4.5\mu\text{m}$ emission from g23 at levels of 50, 100, 200, 300, 400, 500, 600 and 700 MJy/sr. (*e - Right*) Contours of $4.5\mu\text{m}$ emission from g25 at levels of 40, 50, 100, 200, 300, 500, 700 MJy/sr. Symbols are as defined in Figure 17.

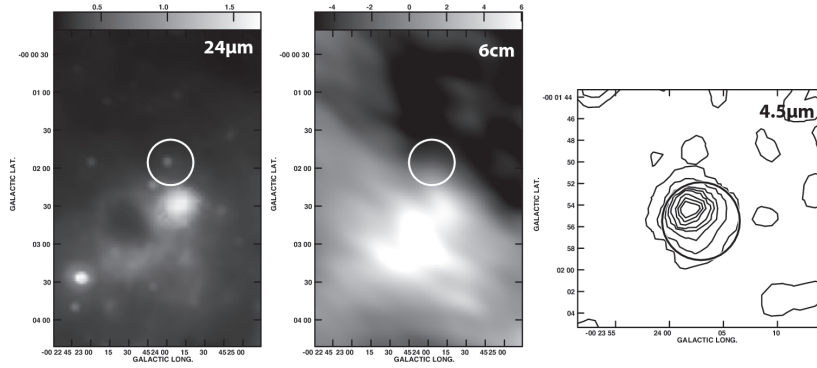


Fig. 21.—: (*a - Left*) A $24\mu\text{m}$ image of G359.6-0.03 or g27 as presented by a circle where $4.5\mu\text{m}$ excess emission is detected. (*b - Middle*) A 20cm continuum image of (a). (*c - Right*) contours of emission from the source associated with g27 at $4.5\mu\text{m}$ at levels of 50, 100, 200, 300, 400, 600, 800 and 1000 MJy/sr. Symbols are as defined in Figure 17.

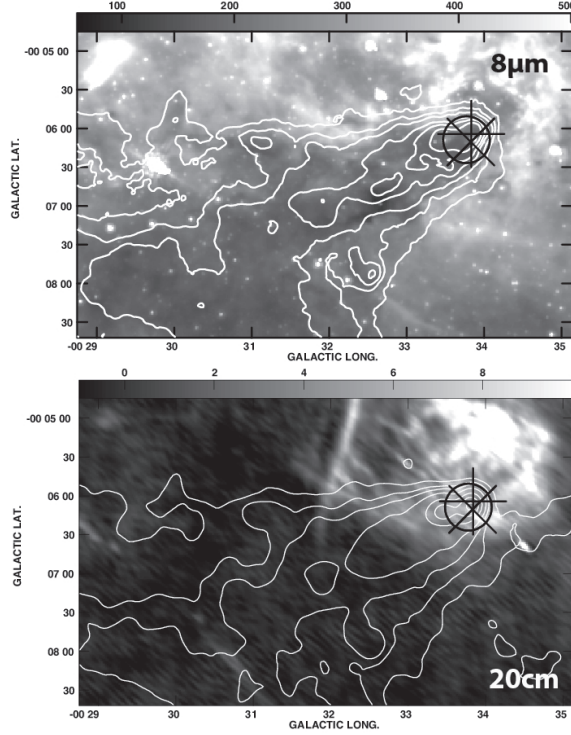


Fig. 22.—: (a Top) Contours of $450\mu\text{m}$ emission from Sgr C with a resolution $8''$ are superimposed on a grayscale $8\mu\text{m}$ image. Levels are at 5, 7.5, 10, 15, 20 and 30 Jy/beam. (b Bottom) Contours of $450\mu\text{m}$ emission from Sgr C are superimposed on a grayscale 20cm image with a spatial resolution of $12.8'' \times 12.8''$. Levels are at 2, 2.5, 3, 4, 6, 8, and 10 Jy/beam. Symbols are as defined in Figure 17.

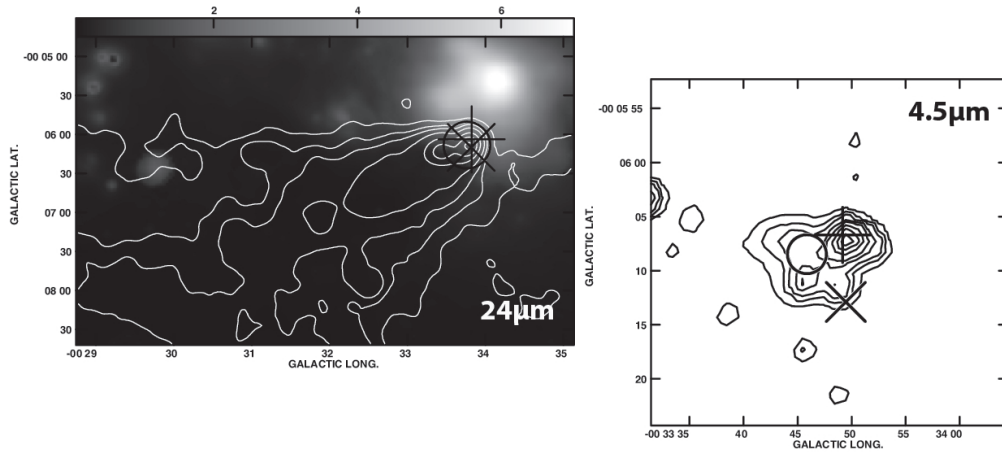


Fig. 22.—: (c Top) A MIPS image of the region shown in (a) at $24\mu\text{m}$. (d Bottom) Contours of $4.5\mu\text{m}$ emission from the $4.5\mu\text{m}$ excess source g29, as identified by a circle. Levels are at 50, 75, 100, 150, 200 and 300 MJy/sr. Symbols are as defined in Figure 17.

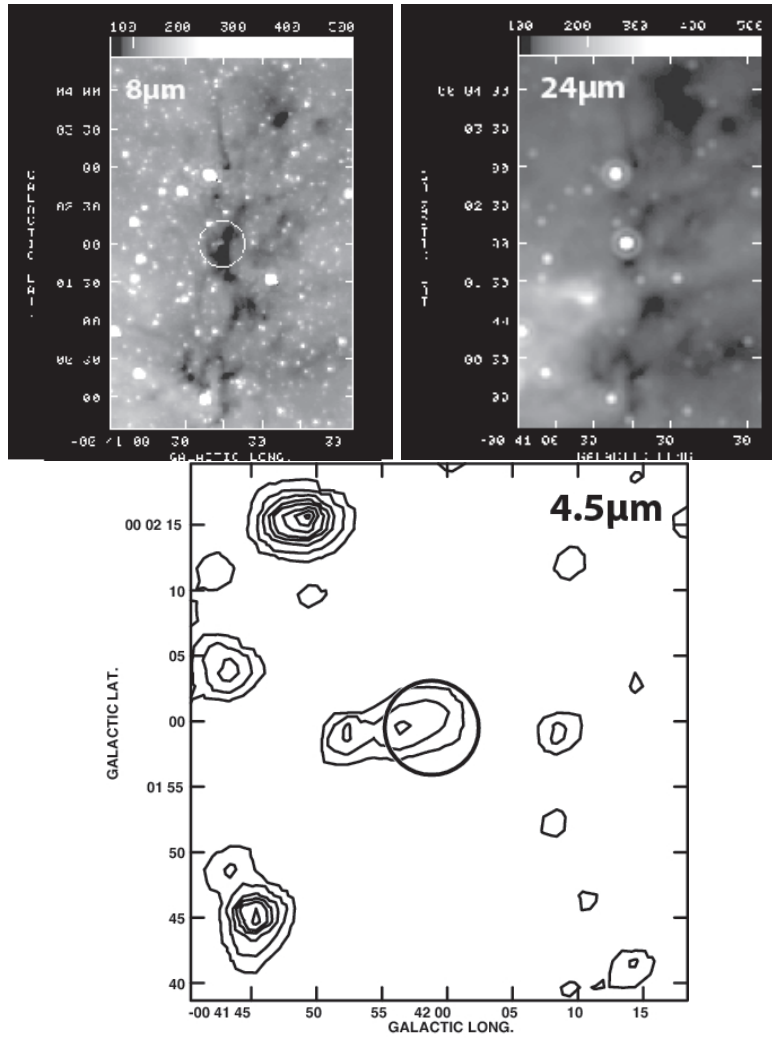


Fig. 23.—: (a - Top Left) A grayscale $8\mu\text{m}$ image of the $4.5\mu\text{m}$ excess source g30. The position of the $4.5\mu\text{m}$ excess source is shown by a circle. (b - Top Right) Similar to (a) except at $24\mu\text{m}$. (c - Bottom) Contours of $4.5\mu\text{m}$ emission from G359.30+0.033 at levels of 25, 50, 100, 150, 200, 300, 400 and 500 MJy/sr. Symbols are as defined in Figure 17.

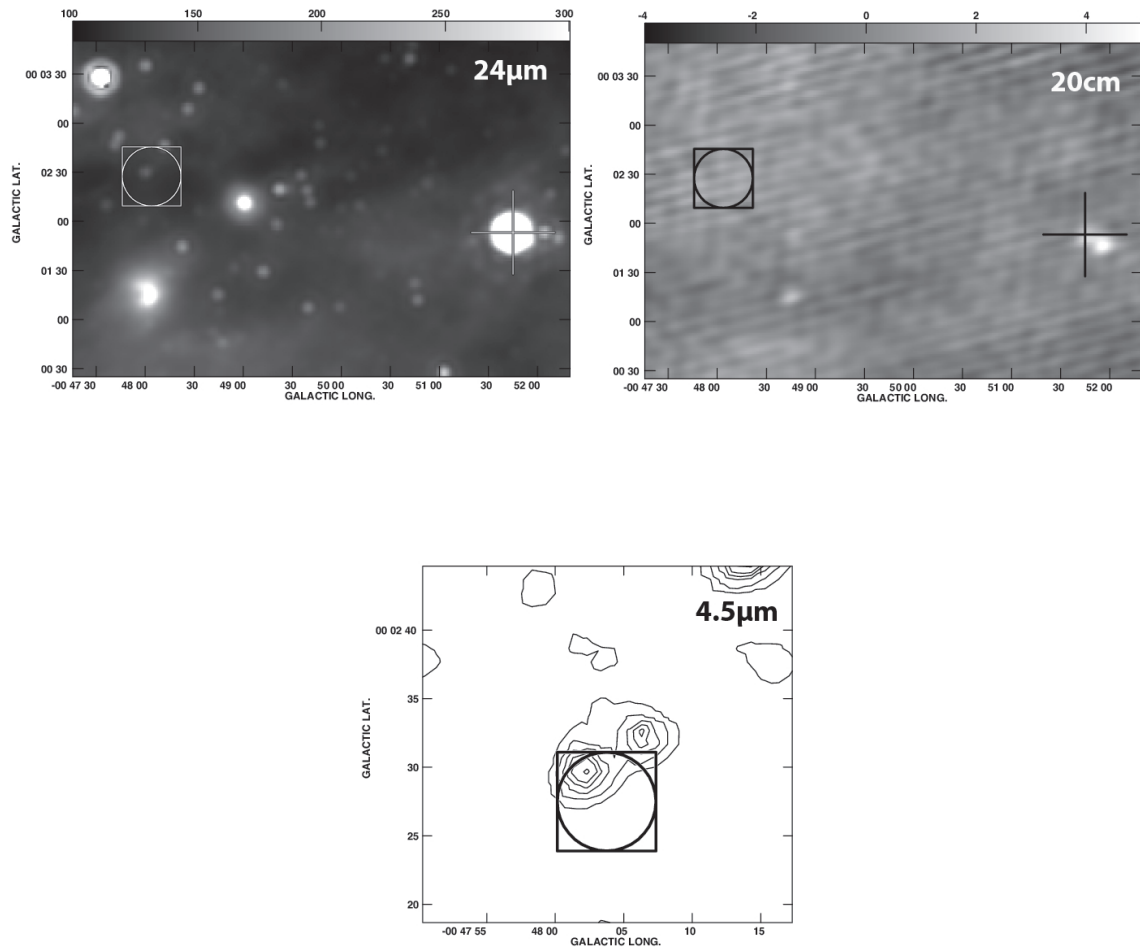


Fig. 24.—: (a - Top Left) A grayscale $24\mu\text{m}$ image of the $4.5\mu\text{m}$ excess source g31. (b - Top Right) Similar to (a) except that the image is shown at 20cm. (c - Bottom) Contours of $4.5\mu\text{m}$ emission from G359.199+0.041 at levels of 50, 100, 200, 300, 400, 600, 800 and 1000 MJy/sr. Symbols are as defined in Figure 17.

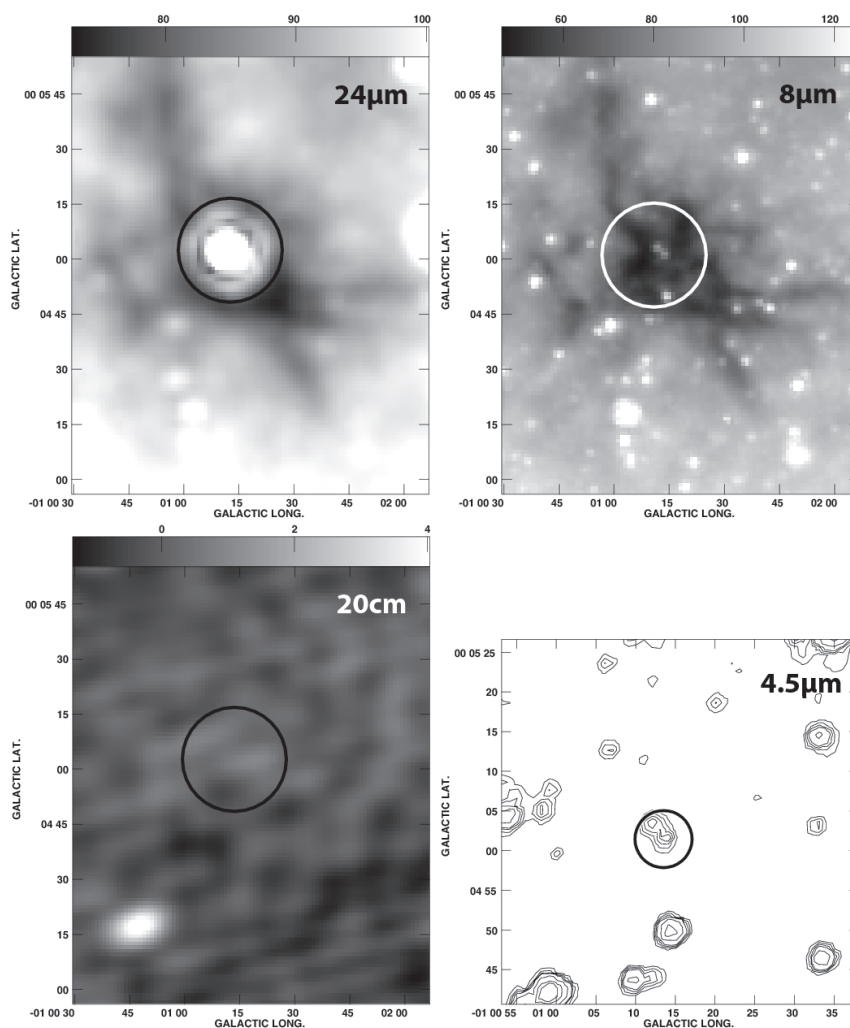


Fig. 25.—: (a - Top Left) A grayscale $24\mu\text{m}$ image of the $4.5\mu\text{m}$ excess source g32 from 73 MJy/sr . (b - Top Right) Similar to (a) except at $8\mu\text{m}$ from 47 to 125 MJy/sr . (c - Bottom Left) Similar to (a) except at 20cm from range = -1.3 to 4 mJy/beam . (d - Bottom Right) Contours of $4.5\mu\text{m}$ emission from $\text{G}359.30+0.033$ at levels of $15, 20, 25, 30, 50, 100, 150$ and 300 MJy/sr . The position of the $4.5\mu\text{m}$ excess source is shown by a circle. Symbols are as defined in Figure 17.

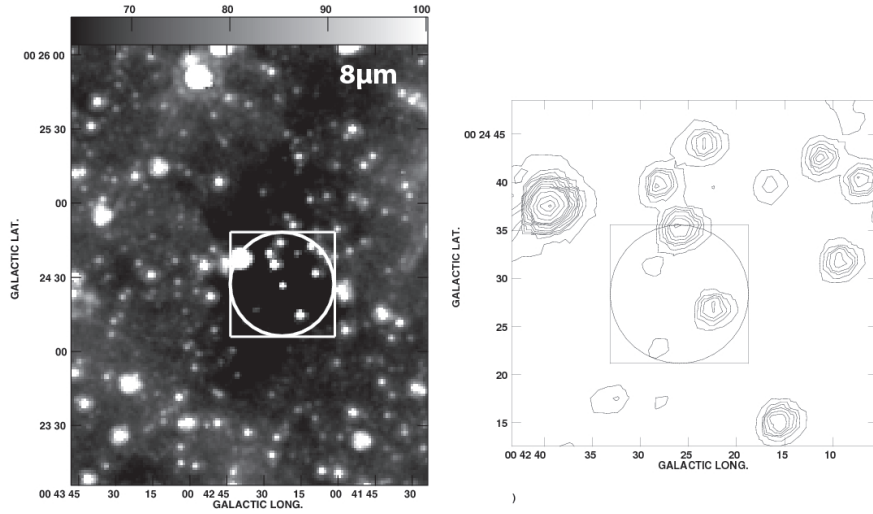


Fig. 26.—: (a - *Left*) An $8\mu\text{m}$ image from 64 to 100 MJy/sr of the $4.5\mu\text{m}$ excess source g5, G0.708+0.408, projected in the middle of an IR dark cloud. (b - *Right*) Contours of $4.5\mu\text{m}$ emission from the $4.5\mu\text{m}$ excess source g5 that shows excess emission at this wavelength. Levels are at 25 50 75 100 150 200 300 400 500 600 1000 2000 2500 MJy/sr. Symbols are as defined in Figure 17.

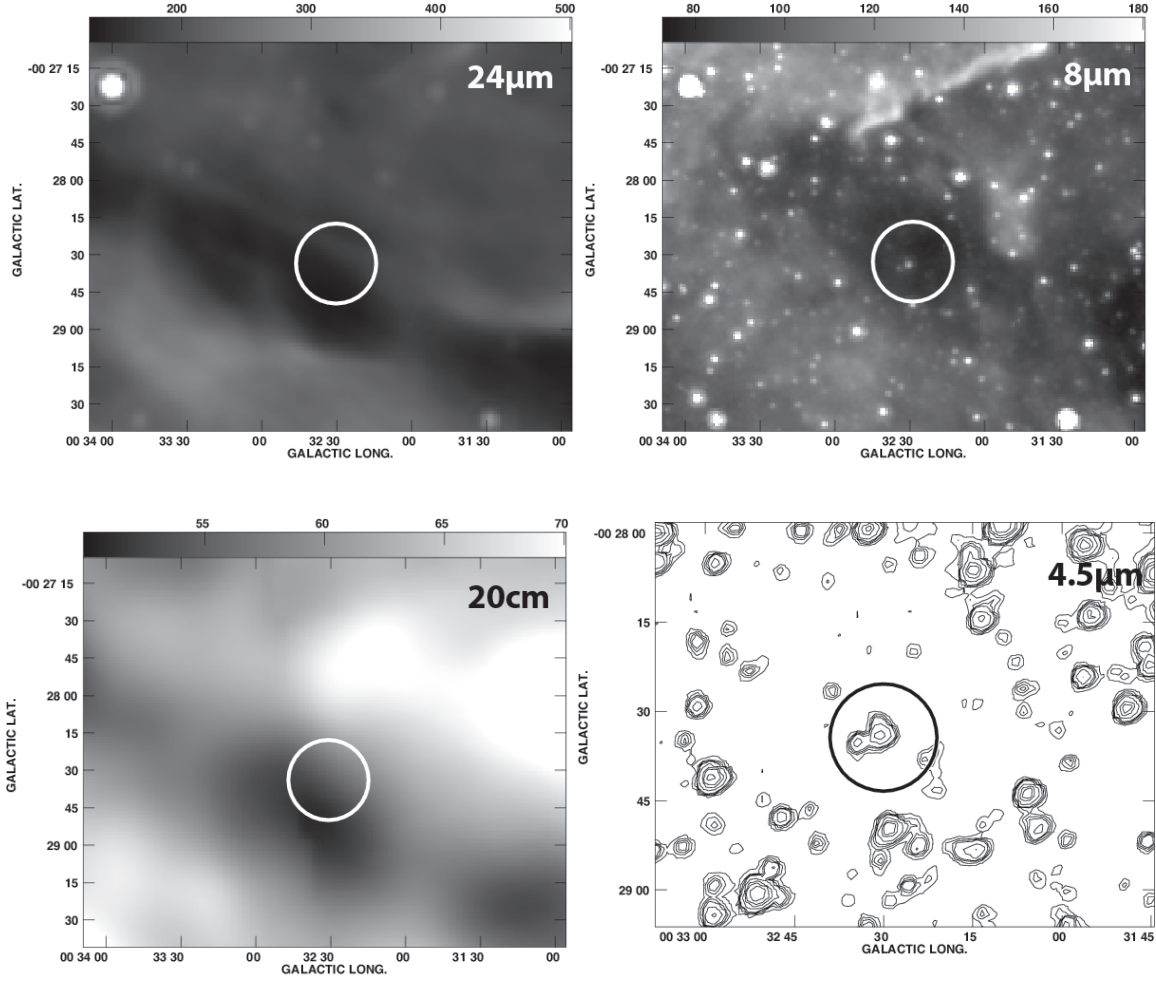


Fig. 27.—: (a - Top Left) A grayscale image of g11 at $24\mu\text{m}$ with a flux range between 130 and 500 MJy Sr^{-1} . (b - Top Right) Similar to (a) except at $8\mu\text{m}$ with a flux range between 73 and 180 MJy sr^{-1} . (c - Bottom Left) A 20cm continuum image with a flux range between 50 and 80 mJy beam^{-1} . (d - Bottom Right) Contours of $4.5\mu\text{m}$ emission from g11 with contours at levels of 15, 20, 25, 30, 50, 100, 150 and 300 MJy sr^{-1} . Symbols are as defined in Figure 17.

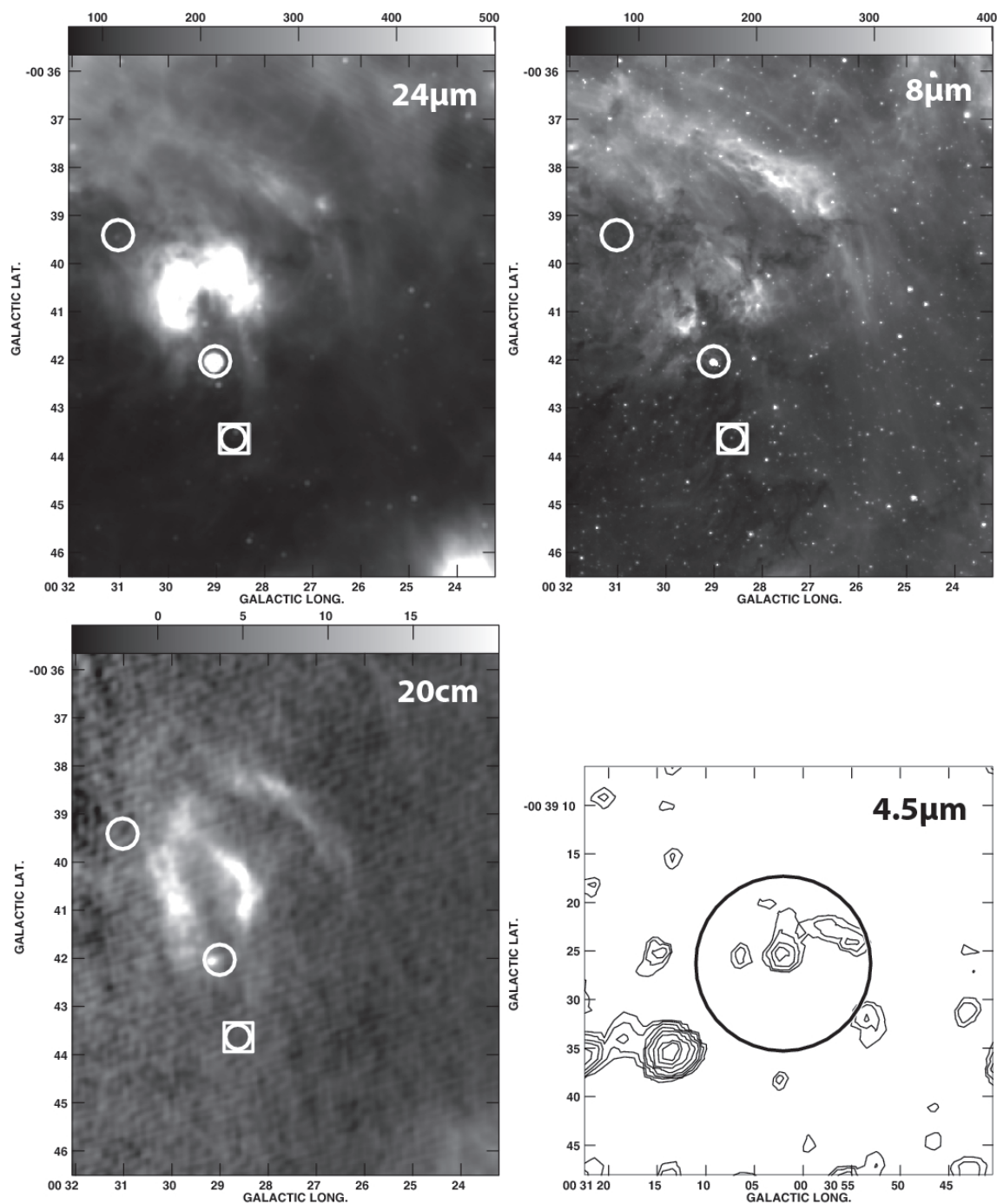


Fig. 28.—: (a - Top Left) Greyscale image of g12, g13, g14 at $24\mu\text{m}$ with a flux range between 66 and 500 MJy sr^{-1} . (b - Top Right) Similar to (a) except at $8\mu\text{m}$ with a flux range between 39 and 400 MJy sr^{-1} . (c - Bottom Left) Similar to (a) except at 20cm with a flux range between -5 and 20 mJy beam^{-1} . (d - Bottom Right) Contours of $4.5\mu\text{m}$ emission from g12 at 9, 11, 15, 20, 30, 50, 100, 150, 300 and 500 MJy sr^{-1} . Symbols are as defined in Figure 17.

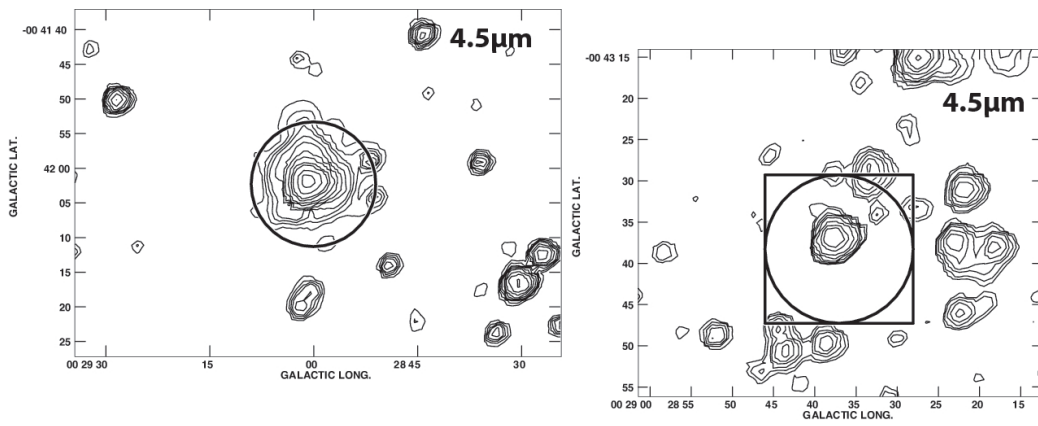


Fig. 28.—: (*e - Left*) Contours of $4.5\mu\text{m}$ emission from g13 with the same levels as those of (d). (*f - Right*) Contours of $4.5\mu\text{m}$ emission from g14 with the same levels as those of (d). Symbols are as defined in Figure 17.

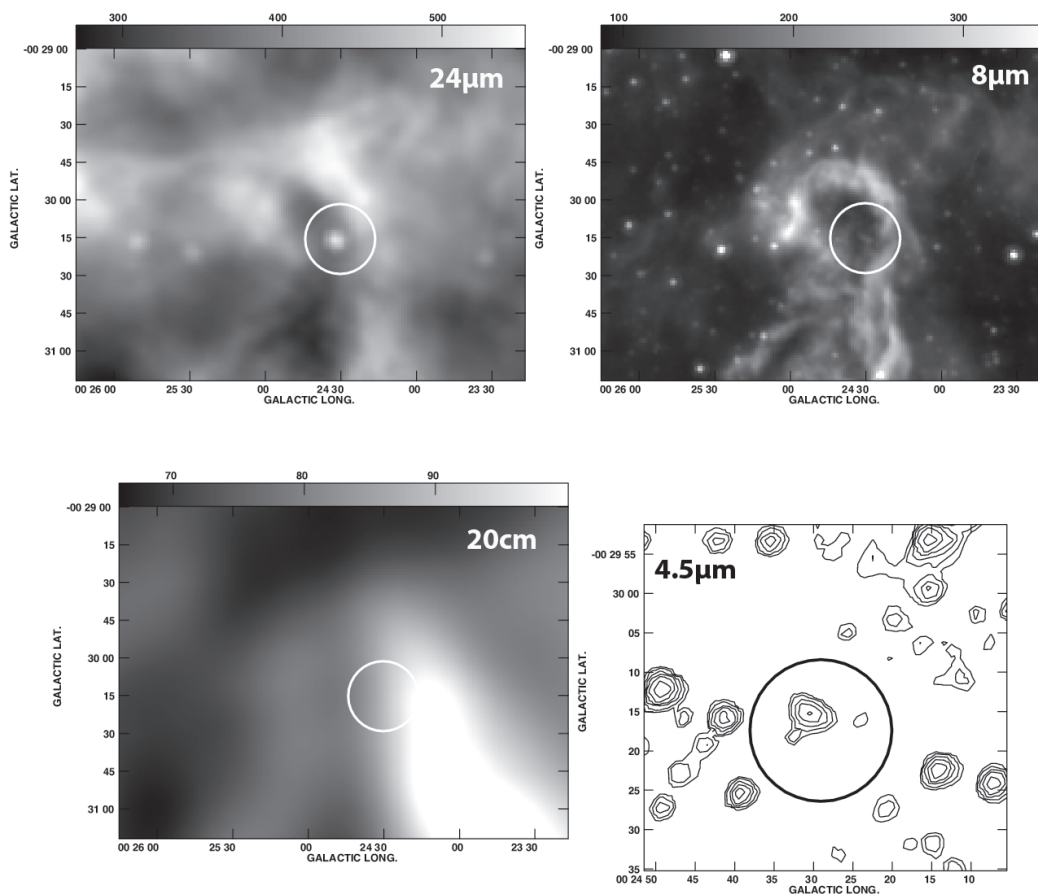


Fig. 29.—: (a - *Top Left*) A grayscale image of g15 at $24\mu\text{m}$ with a flux range between 272 and 551 MJy sr^{-1} . (b - *Top Right*) Similar to (a) except at $8\mu\text{m}$ with a flux range between 88 and 350 MJy sr^{-1} . (c - *Bottom Left*) A 20cm continuum image with a flux range between 66 and $100 \text{ mJy beam}^{-1}$. (d - *Bottom Right*) Contours of $4.5\mu\text{m}$ emission from g15 with contours at levels of 9, 11, 15, 20, 30, 50, 100, 150, 300 and 500 MJy sr^{-1} . Symbols are as defined in Figure 17.

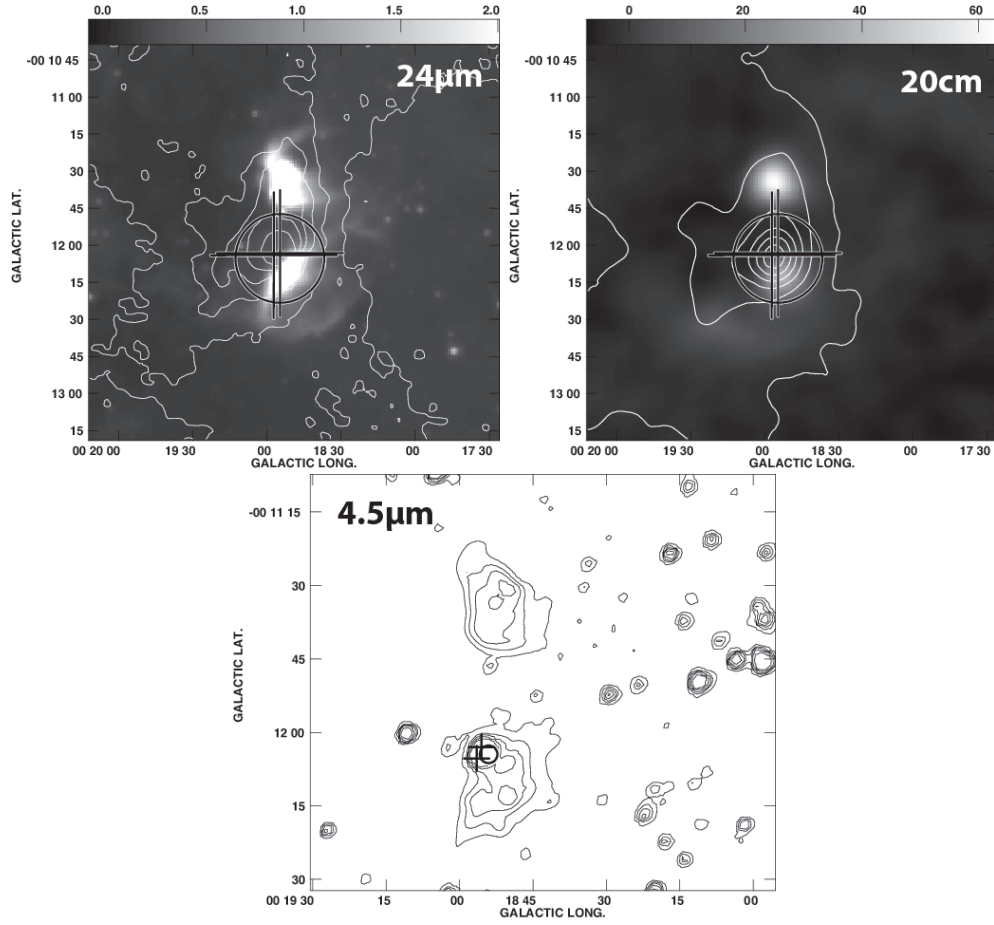


Fig. 30.—: (a -*Top Left*) Contours of $450\mu\text{m}$ emission from g17 at 8, 10, 13, 16, 19, 25 Jy/beam are superimposed on a $8\mu\text{m}$ image. (b - *Top Right*) Contours of $850\mu\text{m}$ emission from g17 at 0.5, 1, 2, 3, 4, 5, 6, 7 Jy beam $^{-1}$ are superimposed on a 20cm continuum image. (c - *Bottom*) Contours of $4.5\mu\text{m}$ emission from g17 at levels of 60, 100, 140, 200 and 300 MJy sr $^{-1}$. Symbols are as defined in Figure 17.

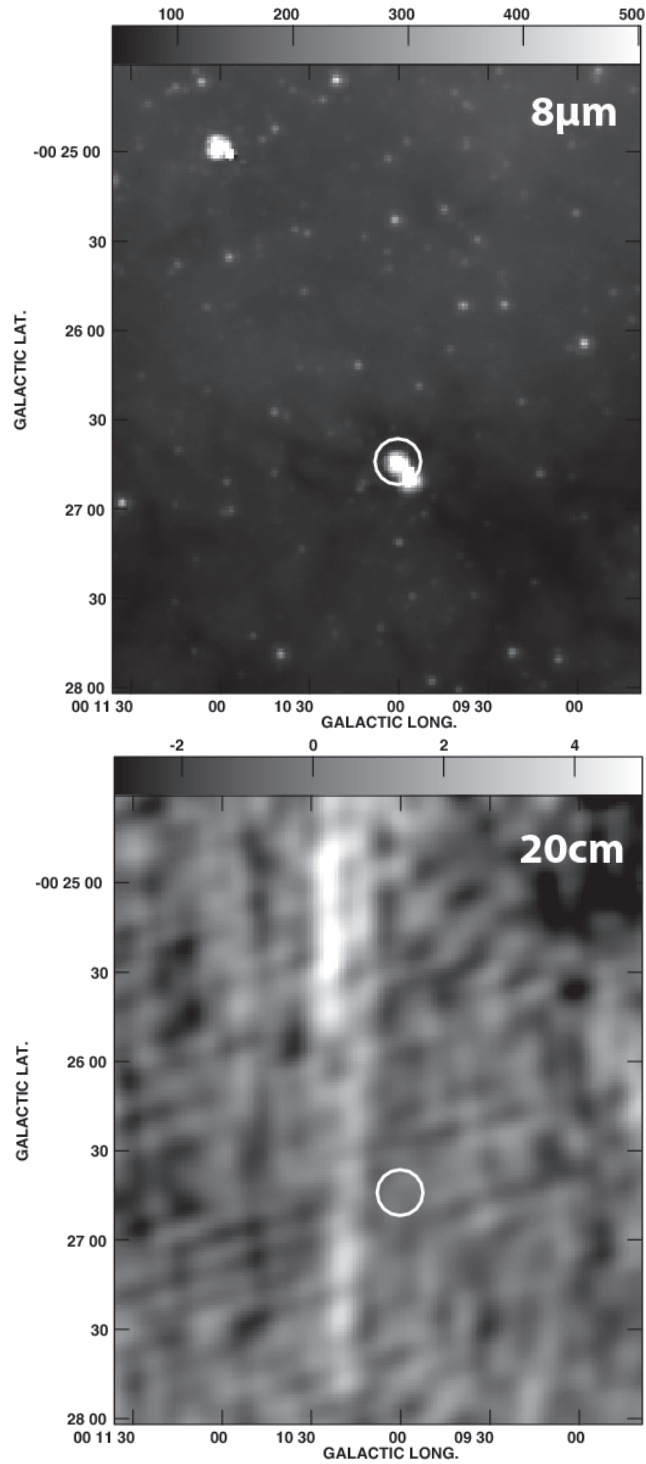


Fig. 31.—: (*a - Top*) A greyscale $8\mu\text{m}$ image of the region toward g18 with flux range between 45 and 500 MJy sr^{-1} (*b - Bottom*) A greyscale 20cm continuum image toward g18 with flux range between -3 and 5 mJy beam^{-1} . Symbols are as defined in Figure 17.

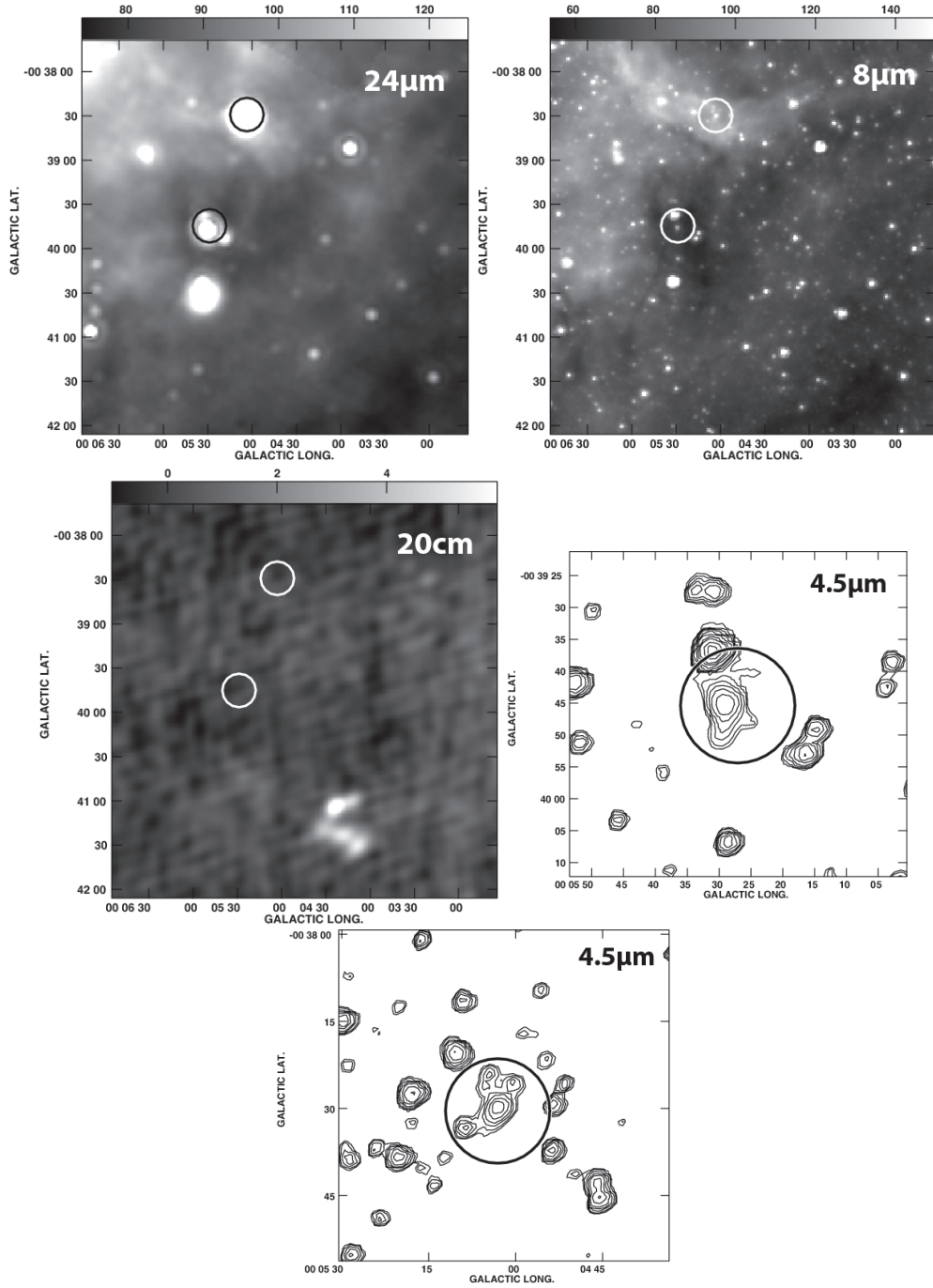


Fig. 32.—: (a - Top Left) A greyscale $24\mu\text{m}$ image of g19 and g20 with flux range between 74 and 125 MJy sr^{-1} . (b - Top Right) A greyscale $8\mu\text{m}$ image of g19 and g20 with flux range between 54 and 150 MJy sr^{-1} . (c - Middle Left) A greyscale 20cm continuum image of g19 and g20 with flux range between -1 and 6 mJy beam^{-1} . (d - Middle Right) Contours of $4.5\mu\text{m}$ emission from g19 at $18, 22, 30, 40, 60, 100, 200, 300, 600$ and 1000 MJy sr^{-1} . (e - Bottom) Contours of $4.5\mu\text{m}$ emission from g20 at $18, 22, 30, 40, 60, 100, 200, 300, 600$ and 1000 MJy sr^{-1} . Symbols are as defined in Figure 17.

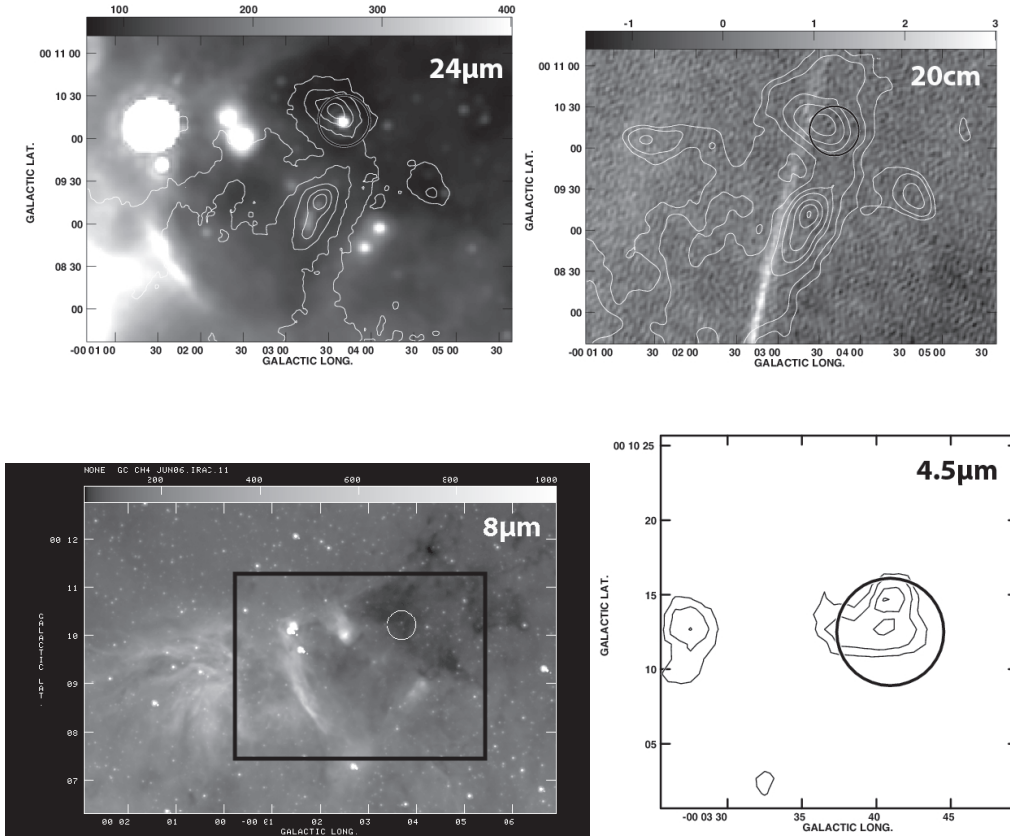


Fig. 33.—: (a - Top Left) Contours of $450\mu\text{m}$ emission from g22 at 2.5, 3, 3.5, 4, 5, 6 and 7 Jy beam^{-1} are superimposed on a $24\mu\text{m}$ continuum image. (b - Top Right) Contours of $850\mu\text{m}$ emission from g22 at 2.5, 3, 3.5, 4, 5, 6 and 7 Jy beam^{-1} are superimposed on a 20cm continuum image. (c - Bottom Left) A greyscale $8\mu\text{m}$ image of a large region presenting the distribution of PAH emission in the vicinity of g22. The rectangular box drawn on this figure corresponds to the area shown in (a) and (b). (d - Bottom Right) Contours of $4.5\mu\text{m}$ emission from g22 is shown at 15, 20, 30, 40, 50, 60 MJy sr^{-1} . Symbols are as defined in Figure 17.

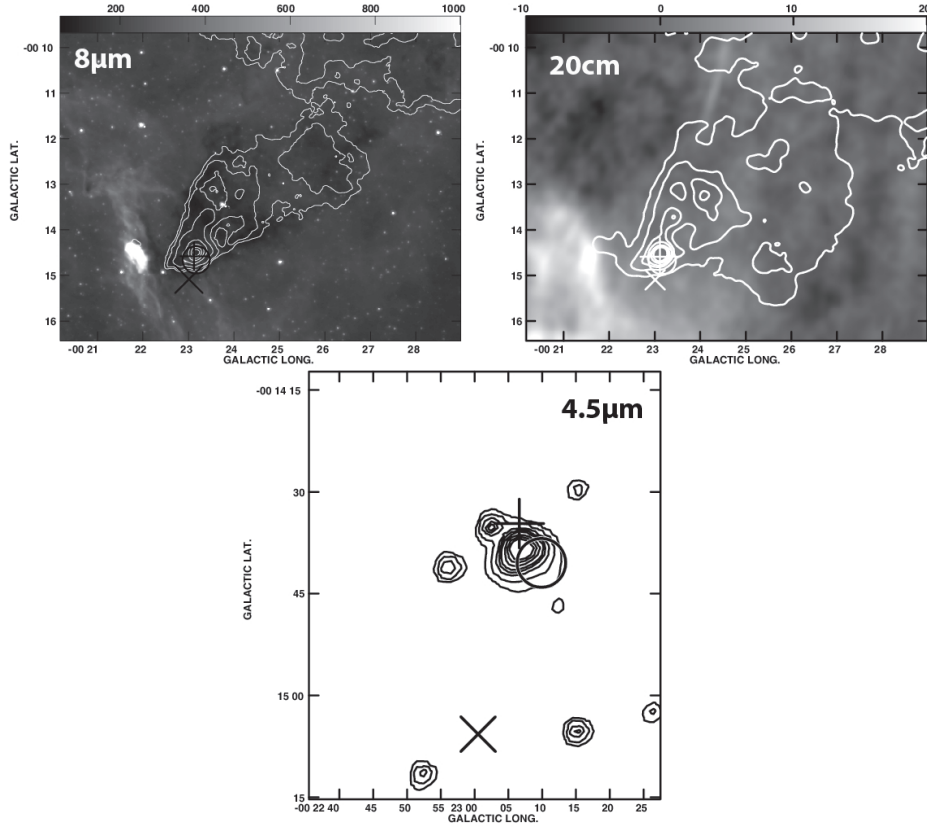


Fig. 34.—: (a - Top Left) Contours of $450\mu\text{m}$ emission from g26 at 3, 4.5, 8, 15, 25, 40 and 60 Jy beam^{-1} are superimposed on a $8\mu\text{m}$ continuum image. (b - Top Right) Contours of $850\mu\text{m}$ emission from g26 at 2, 3, 4, 5, 7 and 9 Jy beam^{-1} are superimposed on a grayscale 20cm continuum image. (c - Bottom) Contours of $4.5\mu\text{m}$ emission from g26 is shown at 50, 100, 200, 300, 400, 600, 800 and 1000 MJy sr^{-1} . Symbols are as defined in Figure 17.

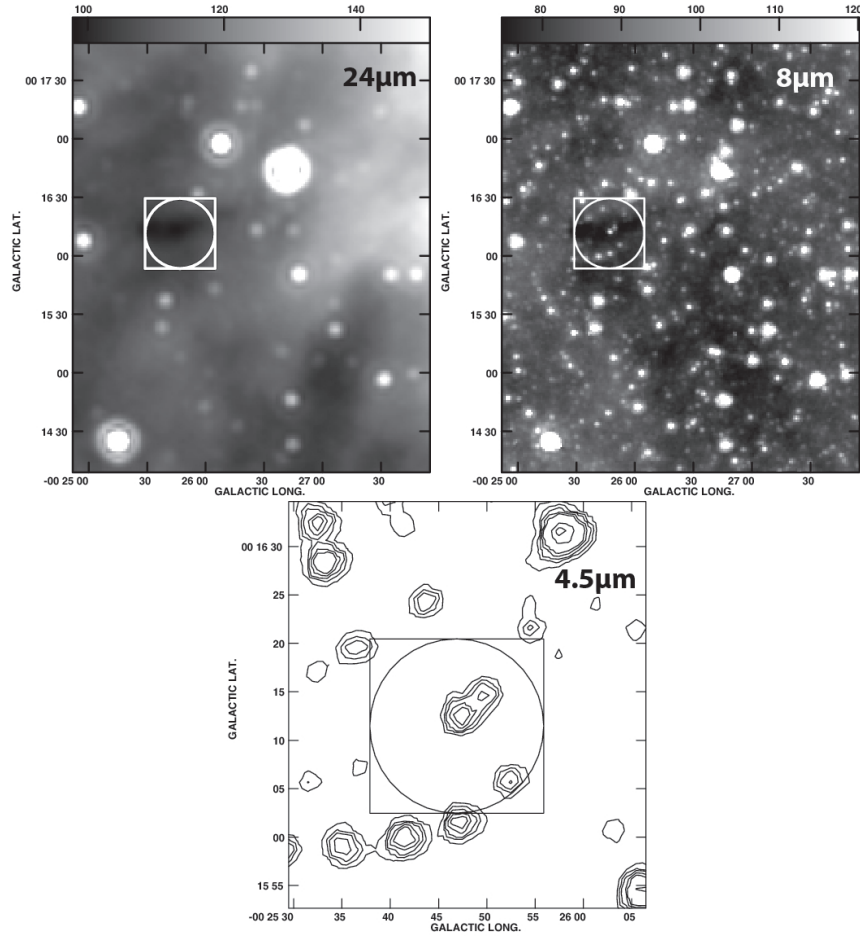


Fig. 35.—: (a - Top Left) A $24\mu\text{m}$ greyscale image of the region in the vicinity of g28 which lies at the center of the circle and square symbols. The flux range is between 98 and 150 MJy sr^{-1} . (b - Top Right) Similar to (a) except that the emission is seen at $8\mu\text{m}$. The flux range is between 75 and 120 MJy sr^{-1} (c - Bottom) Contour levels of emission at $4.5\mu\text{m}$ are set at $25, 35, 50, 75, 100, 300$ and 500 MJy sr^{-1} . Symbols are as defined in Figure 17.

Table 1. The Galactic coordinates and flux density of sources in G359.43+0.02

#	GLON	GLAT	$S_{6cm} \pm \sigma$	$S_{20cm} \pm \sigma$	θ_{maj}''	θ_{min}''
1	359.522356	0.012511	6.5±1.6	4.1±2.2	8.8	2.0
2	359.495378	0.038569	5.2±2.4	—	12.9	10.2
3	359.485425	0.083103	6.5±3.6	3.0±1.8	7.9	3.8
4	359.472092	0.052111	5.7±2.2	5.3±2.4	6.9	0.4
5 ^b	359.456575	0.019586	3.6±1	2.8±1.7	4.2	—
6 ^a	359.429236	0.035489	3.4±1.2	4.4±0.9	5.8	—
7	359.434825	0.022075	12.6±3.4	—	19	11
8	359.432242	0.022986	14.4±4	—	21.3	11.1
9	359.423431	0.015069	6.9±1.7	4.8±2.5	11	7
10	359.439063	0.005402	76.0	96±9	—	900'' ²
11 ^c	359.413464	0.032297	1.4±1.7	1.3±2	11.1	—
11e ^c	—	—	49±20	40.3±12	1472'' ²	—
12	359.403742	0.000797	13.8±2.8	6.0±2.3	13.4	11.6
13	359.404019	-0.000811	9.5±8.6	9.7±5.2	11.4	9.6
14	359.419481	0.001042	—	—	—	—
15	359.390961	0.035469	4.3±1.3	9.5±4.2	8.4	5.9
16	359.373078	0.017686	—	—	9.0	8.2
17	359.363663	-0.000190	25±3.2	30.8±5.6	—	—

^c source 11 has a central compact source and an extended component

^bInfrared counterpart 300758

^aInfrared counterpart 284291

Table 2. The Parameters of the SED Fits to Candidate YSOs in G359.43+0.02

SST GC #	l	b	χ^2_{min}	nfits	$\langle A_v \rangle$	$\langle M_\star \rangle$	$\langle L_\star \rangle$	$\langle \dot{M}_{env} \rangle$	$\langle \text{Stage} \rangle$
251914	359.4130	0.09095	0.03	310	32.1	8.0±1.3	1.4±1.2E+03	2.7± 4.3E-04	I
255492	359.4145	0.08451	0.00	736	31.6	5.0±1.6	6.5±7.8E+02	1.1± 3.5E-04	I
272626	359.4288	0.05876	4.57	240	18.8	10.1±0.7	6.5±1.2E+03	0.0±0.0E+00	II
276597	359.4709	0.07663	5.97	52	15.0	7.5±0.5	2.3±0.7E+03	0.0±0.0E+00	III
284291 ^a	359.4287	0.03534	0.07	204	37.6	9.5±1.0	5.2±1.9E+03	0.8±3.8E-04	I
297164	359.4352	0.01400	0.00	739	36.2	8.4±0.9	2.4±1.2E+03	1.3±3.5E-04	I
297494	359.4688	0.03400	0.00	703	34.9	7.5±0.9	1.7±1.0E+03	1.7±4.6E-04	I
300758 ^b	359.4562	0.01993	1.66	59	17.6	8.8±1.1	3.3±1.6E+03	5.1±5.2E-05	I
305505	359.4583	0.01236	0.00	837	38.0	10.1±1.4	5.7±2.2E+03	2.2±5.1E-04	I
307175	359.4427	0.02637	0.00	443	36.1	6.9±1.0	1.2±0.9E+03	2.2±5.5E-04	I
307819	359.4249	0.01234	4.18	20	15.0	6.2±0.6	1.1±0.1E+03	1.0±4.7E-04	I
311793	359.4072	0.03009	0.00	453	40.8	8.3±0.8	2.8±1.2E+03	1.0±3.4E-04	I
313278	359.4882	0.01704	1.28	18	16.8	6.3±0.7	2.9±0.8E+02	1.8±2.3E-04	I
317711	359.4334	0.02412	0.08	450	24.7	6.5±0.8	8.8±5.9E+02	1.0±2.9E-04	I
320517	359.4441	0.02219	0.00	784	39.2	9.6±1.1	5.1±1.8E+03	1.4±6.3E-04	I
323541	359.5125	0.01483	5.03	55	16.6	7.0±1.0	2.0±0.8E+03	0.0±0.0E+00	II
335380	359.4371	0.05085	0.00	346	30.2	9.5±2.4	5.8±4.6E+03	2.3±9.5E-04	I
336047	359.4591	0.03848	7.85	6	17.0	11.7±0.8	1.0±0.2E+04	0.0±0.0E+00	II

^aRadio counterpart 6

^bRadio counterpart 5

Table 3. The Parameters of the SED Fits to Candidate YSOs in $l < 0^\circ$

SST GC #	l	b	χ^2_{min}	nfits	$\langle A_V \rangle$	$\langle M_\star \rangle$	$\langle L_\star \rangle$	$\langle \dot{M}_{env} \rangle$	$\langle \text{Stage} \rangle$
116907	358.7362	0.0045	0.80	13	16.3	7.7±0.5	1.2±0.3E+03	7.0±9.5E-04	I
119577	358.8940	0.0943	18.80	3	15.0	7.0±0.0	4.7±0.1E+02	2.6±3.5E-04	I
119780	358.8605	0.0729	0.07	471	29.7	4.7±0.8	4.2±3.3E+02	0.2±1.8E-04	I
121566	358.8108	0.0369	5.64	10	15.5	6.9±0.0	1.5±0.0E+03	0.0±0.0E-00	III
122375	358.7448	-0.0062	0.00	1072	28.1	4.1±1.6	2.5±2.7E+02	0.7±1.7E-04	I
126327	358.8288	0.0347	7.12	6	15.0	7.0±0.1	4.9±0.4E+02	3.1±3.3E-04	I
127127	358.7587	-0.0108	0.00	485	34.7	5.1±1.5	0.8±1.0E+03	0.3±2.8E-09	II
127297	358.7373	-0.0245	0.00	1537	38.9	8.9±1.0	3.4±1.4E+03	1.1±3.0E-04	I
131902	358.9174	0.0747	17.20	12	15.0	9.5±0.4	5.3±0.8E+03	0.0±0.0E-00	III
132101	358.9409	0.0887	0.23	71	39.4	12.6±3.1	1.0±0.5E+04	0.9±1.7E-03	I
134327	358.9658	0.0982	0.07	84	15.7	5.0±0.5	3.5±0.9E+02	1.2±4.2E-05	I
136092	358.9102	0.0592	0.22	126	18.1	8.5±1.2	4.0±1.8E+03	3.2±9.4E-05	I
136259	358.8728	0.0356	1.05	84	15.9	7.1±1.0	1.6±1.3E+03	1.2±4.1E-04	I
137737	358.8181	-0.0020	11.70	5	15.0	6.5±0.2	2.9±0.4E+02	1.3±0.5E-04	I
142082	358.8714	0.0194	7.02	4	15.0	6.8±0.1	3.6±0.4E+02	2.3±3.0E-04	I
142930	358.8283	-0.0094	5.72	5	15.0	6.6±0.0	4.6±0.0E+02	1.7±0.0E-00	I
142942	358.9795	0.0840	0.11	58	21.9	7.6±0.6	7.3±3.4E+02	2.5±2.7E-04	I
146060	358.8148	-0.0260	0.00	646	37.5	5.4±1.9	1.0±1.4E+03	5.2±2.3E-04	I
147176	358.7761	-0.0527	10.72	2	15.0	6.3±0.0	2.5±0.0E+02	1.8±0.0E-04	I
147584	358.8293	-0.0210	0.00	790	28.9	7.4±1.5	2.2±1.5E+03	0.6±2.4E-04	I
147743	358.7765	-0.0540	12.29	2	15.0	6.3±0.0	2.5±0.0E+02	1.8±0.0E-04	I
150660	358.8131	-0.0391	1.65	18	15.5	5.6±0.2	2.1±0.3E+02	1.1±1.0E-05	I
153970	358.8569	-0.0206	5.57	27	15.0	8.3±0.7	3.3±1.0E+03	0.0±0.0E-00	III
158032	358.8088	-0.0607	4.76	50	15.0	4.4±0.3	3.2±0.9E+02	0.0±0.0E-00	II
158837	358.8657	-0.0277	0.38	174	17.0	4.2±0.4	2.7±0.9E+02	0.3±3.4E-08	II
161727	358.9833	0.0373	0.00	415	37.9	9.0±1.3	3.5±1.8E+03	2.6±8.1E-04	I
165041	358.9781	0.0254	15.11	3	15.0	6.7±0.2	4.5±4.0E+02	2.6±3.5E-04	I
166903	358.8068	-0.0850	0.00	683	34.7	6.5±1.8	1.8±2.1E+03	0.7±3.5E-04	I
168737	359.0166	0.0399	6.03	507	15.0	9.7±0.5	5.7±1.0E+03	0.0±0.0E-00	III
170621	358.7689	-0.1181	5.02	3	15.0	5.5±0.0	1.5±0.0E+02	7.1±0.0E-05	I
173766	358.9977	0.0149	2.62	101	15.5	3.7±0.9	7.3±2.2E+01	0.7±1.0E-04	I
175663	359.2416	0.1607	8.10	19	17.1	7.0±0.7	7.0±2.3E+02	1.2±2.0E-04	I
179253	359.2140	0.1343	1.73	55	15.5	5.3±0.5	6.7±2.4E+02	0.0±0.0E-00	II
180155	358.8542	-0.0901	0.00	727	27.2	4.1±0.7	2.3±1.6E+02	0.7±4.1E-05	I
187849	358.8233	-0.1286	6.13	10	15.0	5.7±0.4	1.8±0.4E+02	2.7±2.6E-04	I
188031	358.9874	-0.0278	7.34	5	15.0	8.2±0.2	9.9±1.9E+02	5.9±8.9E-04	I
188899	358.8238	-0.1308	8.31	3	15.0	5.5±0.0	1.5±0.0E+02	7.1±0.0E-05	I
189586	359.1190	0.0497	0.00	303	28.6	4.5±1.7	5.1±6.8E+02	1.4±3.1E-04	I
193986	359.0376	-0.0106	8.56	28	15.0	9.4±0.6	5.1±1.0E+03	0.0±0.0E-00	II
194367	358.8665	-0.1171	0.00	106	36.1	7.6±3.3	2.9±7.2E+03	4.0±9.9E-04	I
194640	358.9834	-0.0455	3.29	6	15.0	6.9±0.1	4.8±0.2E+02	3.5±3.0E-04	I
198456	359.0938	0.0138	6.56	88	16.0	5.8±0.7	9.1±3.7E+02	0.0±0.0E-00	II
201854	359.2106	0.0782	5.57	46	15.0	4.2±0.4	2.5±0.8E+02	2.0±9.5E-06	II
202699	359.1513	0.0397	8.60	189	15.0	9.3±0.6	5.1±1.2E+03	0.0±0.0E-00	III
204187	358.9588	-0.0824	8.50	1	15.0	6.7±0.0	3.2±0.0E+02	4.8±0.0E-05	I
204714	359.0956	0.0007	2.13	51	15.0	4.6±0.7	4.0±3.4E+02	0.2±1.3E-05	II

Table 3—Continued

SST GC #	l	b	χ^2_{min}	nfits	$\langle A_v \rangle$	$\langle M_\star \rangle$	$\langle L_\star \rangle$	$\langle \dot{M}_{env} \rangle$	$\langle \text{Stage} \rangle$
206043	359.3542	0.1572	3.38	31	15.0	6.2±0.5	1.0±0.3E+03	0.0±0.0E-00	III
207736	358.9448	-0.0992	2.03	14	15.2	6.6±0.4	3.4±0.7E+02	2.3±2.0E-04	I
208385	359.3569	0.1534	4.00	17	15.0	4.6±0.4	1.7±0.3E+02	1.3±2.1E-05	I
212351	359.1824	0.0368	1.48	2	15.3	6.7±0.0	3.2±0.0E+02	4.8±0.0E-05	I
212533	358.8852	-0.1468	21.18	4	15.0	6.9±0.1	3.9±0.5E+02	4.1±3.5E-04	I
214283	359.0873	-0.0262	0.15	407	19.2	5.0±0.9	5.6±9.2E+02	0.5±6.5E-05	I
214291	358.9865	-0.0883	5.69	36	15.0	6.5±0.2	1.2±0.1E+03	0.0±0.0E-00	III
214384	359.0151	-0.0708	1.51	4	15.0	6.6±0.0	4.6±0.0E+02	1.7±0.0E-05	I
215021	359.0938	-0.0238	7.90	73	15.0	6.5±0.2	1.2±0.1E+03	0.0±0.0E-00	III
215431	359.1431	0.0056	6.00	3	15.0	5.5±0.0	1.5±0.0E+02	7.1±0.0E-05	I
216691	359.3706	0.1428	2.42	99	21.3	7.9±1.4	3.1±2.5E+03	0.0±0.0E-00	II
219986	359.1208	-0.0185	0.01	471	36.0	7.7±1.1	1.2±0.7E+03	2.3±4.7E-04	I
223624	359.0653	-0.0610	9.33	56	15.4	9.4±0.8	5.2±1.3E+03	0.0±0.0E-00	II
224770	359.4100	0.1489	0.54	219	16.2	6.6±0.8	1.4±0.5E+03	0.0±0.0E-00	II
225677	359.1460	-0.0158	5.60	4	15.0	6.4±0.0	4.1±0.0E+02	7.0±0.0E-05	I
229216	359.0992	-0.0525	0.98	91	15.1	4.6±0.5	2.4±1.0E+02	2.5±9.5E-05	I
231270	359.3173	0.0771	0.00	637	29.8	7.3±1.6	2.2±1.9E+03	1.3±5.7E-04	I
235473	359.4716	0.1627	0.01	683	28.7	5.9±1.2	1.1±0.9E+03	0.1±1.5E-04	I
235995	359.0383	-0.1052	9.89	183	15.0	10.6±0.1	7.5±0.3E+03	0.0±0.0E-00	III
237228	359.1848	-0.0177	20.81	4	15.0	8.5±0.0	3.6±0.0E+03	0.0±0.0E-00	II
238167	359.4078	0.1174	2.40	78	15.3	7.9±0.7	2.9±1.1E+03	0.0±0.0E-00	III
241266	359.2441	0.0096	6.91	53	15.0	6.9±0.5	1.6±0.4E+03	0.0±0.0E-00	III
243433	359.4619	0.1388	6.30	65	15.0	5.0±0.3	4.9±1.2E+02	0.0±0.0E-00	II
243522	359.1801	-0.0348	0.51	20	15.1	5.9±0.4	4.4±2.0E+02	3.7±6.9E-05	I
246410	359.3009	0.0334	2.57	15	18.1	8.8±0.8	1.8±0.4E+03	2.0±1.7E-04	I
251494	359.1027	-0.0992	6.36	10	15.0	7.1±0.2	1.8±0.2E+03	0.0±0.0E-00	II
251914	359.4130	0.0909	0.03	310	32.1	8.0±1.3	1.4±1.2E+03	2.7±4.3E-04	I
253913	359.5316	0.1597	15.95	2	15.0	5.5±0.0	1.5±0.0E+02	7.1±0.0E-05	I
254708	359.0599	-0.1321	0.00	595	38.6	7.7±1.5	3.0±2.7E+03	0.1±1.2E-04	I
255492	359.4145	0.0845	0.00	736	31.6	5.0±1.6	6.5±7.8E+02	1.1±3.5E-04	I
258517	359.0967	-0.1172	9.05	162	15.0	7.2±0.0	1.9±0.0E+03	0.0±0.0E-00	III
258882	359.2085	-0.0492	4.98	23	15.0	7.4±0.6	2.1±0.8E+03	0.0±0.0E-00	II
262648	359.0669	-0.1440	11.83	8	15.0	16.4±1.0	2.7±0.4E+04	0.0±0.0E-00	II
263857	359.2346	-0.0431	0.09	406	38.9	8.9±0.9	4.1±1.5E+03	0.5±2.7E-04	I
264669	359.4653	0.0970	0.00	572	20.6	4.0±0.6	2.3±1.5E+02	0.2±3.6E-07	II
265278	359.3205	0.0067	0.14	104	16.6	4.9±0.6	2.2±0.8E+02	3.2±7.4E-05	I
268132	359.1003	-0.1343	3.01	11	15.0	5.5±0.4	1.7±0.3E+02	4.3±3.9E-04	I
268877	359.2461	-0.0461	0.03	171	36.5	9.7±0.9	5.8±1.8E+03	0.8±1.5E-05	II
272626	359.4288	0.0587	4.57	240	18.8	10.1±0.7	6.5±1.2E+03	0.0±0.0E-00	II
274996	359.2906	-0.0309	1.38	4	28.0	6.8±0.7	8.0±1.1E+02	7.4±8.1E-04	I
275827	359.2791	-0.0397	1.05	9	15.1	8.4±0.3	1.0±0.2E+03	4.8±7.0E-04	I
276597	359.4709	0.0766	5.97	52	15.0	7.5±0.5	2.3±0.7E+03	0.0±0.0E-00	III
277526	359.2104	-0.0854	0.25	255	20.7	5.7±0.7	8.7±4.0E+02	1.5±9.9E-06	II
278053	359.1057	-0.1508	2.38	20	45.1	9.9±4.5	6.4±8.6E+03	0.5±1.5E-03	I
279979	359.1129	-0.1501	4.59	82	17.3	7.0±0.6	1.8±0.5E+03	0.0±0.0E-00	II
282944	359.2387	-0.0788	5.65	28	15.0	4.3±0.5	1.9±0.7E+02	0.6±1.6E-05	I

Table 3—Continued

SST GC #	l	b	χ^2_{min}	nfits	$\langle A_v \rangle$	$\langle M_\star \rangle$	$\langle L_\star \rangle$	$\langle \dot{M}_{env} \rangle$	$\langle \text{Stage} \rangle$
283981	359.2434	-0.0779	3.69	42	15.0	4.3±0.2	2.9±0.7E+02	0.0±0.0E-00	II
284291	359.4287	0.0353	0.07	204	37.6	9.5±1.0	5.2±1.9E+03	0.8±3.8E-04	I
286515	359.1828	-0.1201	0.00	719	32.6	7.2±1.4	2.3±2.0E+03	0.1±1.0E-04	I
288646	359.2087	-0.1085	4.65	15	15.0	9.6±2.4	6.4±4.1E+03	0.0±0.0E-00	III
293719	359.2453	-0.0959	4.27	1261	15.0	6.6±0.0	1.3±0.0E+03	0.0±0.0E-00	III
295788	359.2963	-0.0687	0.07	191	35.3	7.4±1.2	1.7±1.4E+03	2.2±4.4E-04	I
297164	359.4352	0.0140	0.00	739	36.2	8.4±0.9	2.4±1.2E+03	1.3±3.5E-04	I
297494	359.4688	0.0340	0.00	703	34.9	7.5±0.9	1.7±1.0E+03	1.7±4.6E-04	I
300758	359.4562	0.0199	1.66	59	17.6	8.8±1.1	3.3±1.6E+03	5.1±5.2E-05	I
302651	359.3136	-0.0712	0.22	318	19.6	6.6±0.6	1.4±0.3E+03	0.3±2.4E-04	I
302664	359.2228	-0.1270	6.28	15	15.2	6.3±0.7	1.2±0.4E+03	0.0±0.0E-00	III
305505	359.4583	0.0123	0.00	837	38.0	10.1±1.4	5.7±2.2E+03	2.2±5.1E-04	I
306363	359.5484	0.0661	0.01	441	35.1	5.7±1.8	1.2±1.9E+03	0.5±6.7E-05	I
307175	359.4427	-0.0002	0.00	443	36.1	6.9±1.0	1.2±0.9E+03	2.2±5.5E-04	I
307819	359.4249	-0.0123	4.18	20	15.0	6.2±0.6	1.1±0.1E+03	1.0±4.7E-04	I
311087	359.7029	0.1526	9.19	141	15.0	6.4±0.3	1.2±0.2E+03	0.0±0.0E-00	III
311793	359.4072	-0.0300	0.00	453	40.8	8.3±0.8	2.8±1.2E+03	1.0±3.4E-04	I
313278	359.4882	0.0170	1.28	18	16.8	6.3±0.7	2.9±0.8E+02	1.8±2.3E-04	I
314042	359.2046	-0.1584	4.66	106	15.2	4.7±0.5	4.1±1.7E+02	0.0±0.0E-00	II
317583	359.2173	-0.1565	0.00	830	30.3	4.0±1.5	1.9±1.6E+02	0.4±1.3E-04	I
317711	359.4334	-0.0241	0.08	450	24.7	6.5±0.8	8.8±5.9E+02	1.0±2.9E-04	I
320517	359.4441	-0.0221	0.00	784	39.2	9.6±1.1	5.1±1.8E+03	1.4±6.3E-04	I
320729	359.3078	-0.1062	7.32	14	15.0	7.1±0.2	1.8±0.2E+03	0.5±1.0E-06	II
321628	359.3311	-0.0934	0.33	78	28.1	2.9±2.4	2.3±3.3E+02	1.4±3.6E-04	I
323541	359.5125	0.0148	5.03	55	16.6	7.0±1.0	2.0±0.8E+03	0.0±0.0E-00	II
328013	359.4058	-0.0580	0.00	823	32.0	7.7±1.6	3.0±2.8E+03	0.1±1.7E-04	I
329968	359.4136	-0.0565	5.05	73	17.7	8.9±1.0	4.4±1.9E+03	0.0±0.0E-00	II
330325	359.3839	-0.0752	0.01	279	37.5	8.4±0.9	2.3±1.1E+03	2.3±5.8E-04	I
331261	359.2778	-0.1419	6.14	48	15.3	6.0±0.6	1.0±0.3E+03	0.0±0.0E-00	II
331513	359.5929	0.0510	45.54	2	15.0	7.1±0.0	4.5±0.0E+02	7.6±0.0E-04	I
335380	359.4371	-0.0508	0.00	346	30.2	9.5±2.4	5.8±4.6E+03	2.3±9.5E-04	I
336047	359.4591	-0.0384	7.85	6	17.0	11.6±0.8	1.0±0.2E+04	0.0±0.0E-00	II
343554	359.4277	-0.0701	0.24	160	35.3	7.4±1.8	2.6±3.0E+03	1.5±5.3E-04	I
344255	359.3227	-0.1357	3.44	7	15.5	5.2±0.5	6.0±2.2E+02	0.0±0.0E-00	II
344820	359.3390	-0.1266	11.32	2	15.0	6.3±0.0	2.5±0.0E+02	1.8±0.0E-04	I
345503	359.5740	0.0164	1.96	140	17.7	6.6±0.7	1.5±0.5E+03	0.0±0.0E-00	II
346221	359.2843	-0.1625	0.53	3	24.3	5.6±0.6	6.7±3.2E+02	6.5±6.1E-04	I
348310	359.5823	0.0168	1.54	64	16.1	5.0±0.5	5.3±2.0E+02	0.0±0.0E-00	II
349188	359.5809	0.0144	0.13	195	16.5	5.6±0.6	7.9±2.9E+02	0.0±0.0E-00	II
351441	359.4553	-0.0662	0.03	694	39.2	8.7±0.9	3.4±1.4E+03	1.2±4.8E-04	I
358063	359.5668	-0.0086	2.02	33	15.1	9.5±1.4	5.7±2.6E+03	0.0±0.0E-00	II
359581	359.6667	0.0501	3.94	19	15.0	7.1±0.3	1.8±0.3E+03	0.0±0.0E-00	II
359649	359.6652	0.0491	4.13	14	15.0	6.5±0.5	1.1±0.6E+03	1.5±2.9E-05	I
360104	359.4031	-0.1123	1.09	35	15.3	6.6±0.3	4.1±1.1E+02	2.2±3.0E-04	I
360444	359.6817	0.0578	12.18	4	15.0	6.9±0.1	3.9±0.5E+02	4.1±3.5E-04	I
362943	359.8239	0.1410	4.26	24	15.0	4.5±0.3	2.6±0.8E+02	0.7±1.7E-05	I

Table 3—Continued

SST GC #	l	b	χ^2_{min}	nfits	$\langle A_v \rangle$	$\langle M_\star \rangle$	$\langle L_\star \rangle$	$\langle \dot{M}_{env} \rangle$	$\langle \text{Stage} \rangle$
362952	359.5303	-0.0390	3.97	6	15.6	7.1±0.1	4.7±0.2E+02	2.4±1.1E-05	I
363252	359.5781	-0.0101	1.55	12	15.0	5.4±0.3	1.7±0.2E+02	2.9±3.2E-04	I
365847	359.8251	0.1370	0.21	337	32.7	9.1±1.5	5.1±2.9E+03	0.1±1.7E-04	I
366204	359.6598	0.0350	6.06	72	15.7	8.0±1.3	3.3±1.7E+03	0.0±0.0E-00	II
370438	359.5058	-0.0663	0.22	372	37.5	7.8±0.9	1.9±1.0E+03	1.4±3.9E-04	I
370894	359.6155	0.0001	1.21	3	15.0	6.5±0.1	2.5±0.1E+02	1.9±1.0E-04	I
371987	359.8203	0.1238	2.36	32	15.3	5.8±0.5	8.9±3.0E+02	0.0±0.0E-00	II
372254	359.4249	-0.1189	8.40	2	16.8	6.8±0.0	3.4±0.0E+02	6.0±0.0E-05	I
372630	359.5113	-0.0666	0.06	237	31.7	8.8±2.8	4.6±5.0E+03	2.2±7.8E-04	I
373058	359.5164	-0.0641	0.03	99	31.3	7.9±0.6	2.2±1.2E+03	1.9±5.9E-04	I
374813	359.5477	-0.0478	0.03	1000	38.8	9.5±1.0	4.8±1.8E+03	1.0±4.4E-04	I
376861	359.6040	-0.0167	7.40	71	15.5	7.8±1.1	2.9±1.3E+03	0.0±0.0E-00	II
377183	359.3960	-0.1447	5.22	31	16.2	7.8±0.5	2.7±0.6E+03	0.0±0.0E-00	II
380282	359.7906	0.0920	2.73	70	15.0	6.8±0.9	1.6±0.8E+03	1.0±7.7E-06	II
381931	359.4557	-0.1158	0.50	12	27.3	3.6±3.6	7.2±8.5E+02	4.5±6.9E-04	I
384976	359.7965	0.0881	8.82	45	15.0	10.4±0.2	7.2±0.4E+03	0.0±0.0E-00	III
386185	359.4817	-0.1068	3.58	79	15.5	7.4±0.5	2.1±0.6E+03	0.0±0.0E-00	II
387011	359.4816	-0.1082	2.54	22	15.0	5.9±0.7	1.0±0.3E+03	2.7±4.0E-07	II
387018	359.7330	0.0458	8.15	41	15.0	10.2±0.3	6.7±0.8E+03	0.0±0.0E-00	III
390425	359.4830	-0.1129	2.85	47	15.0	5.9±0.9	7.3±8.8E+02	0.5±1.9E-04	I
394544	359.9475	0.1649	0.72	552	27.5	5.7±1.0	9.2±6.1E+02	0.4±5.4E-05	II
395315	359.5677	-0.0690	0.00	1400	34.7	8.7±0.9	3.5±1.3E+03	1.1±4.4E-04	I
397703	359.9313	0.1497	0.00	526	28.8	7.7±1.8	2.7±2.7E+03	1.6±6.7E-04	I
399231	359.9483	0.1576	0.07	528	35.1	8.0±1.8	3.5±4.2E+03	0.1±1.2E-04	I
399927	359.5769	-0.0709	6.83	8	15.0	8.2±0.5	3.2±0.7E+03	1.5±2.6E-09	II
400062	359.5126	-0.1105	0.00	379	33.1	6.5±1.9	1.7±2.2E+03	1.3±4.1E-04	I
401264	359.5329	-0.1000	0.06	281	36.0	8.8±1.0	3.3±1.3E+03	1.9±6.3E-04	I
409238	359.6113	-0.0651	8.31	7	15.0	8.7±0.0	4.0±0.0E+03	0.0±0.0E-00	II
409373	359.5185	-0.1221	2.50	88	17.8	6.5±1.0	1.6±0.6E+03	0.0±0.0E-00	II
411192	359.6193	-0.0633	0.07	303	32.6	7.0±2.0	2.4±2.6E+03	0.5±2.0E-04	I
412509	359.7154	-0.0066	0.09	136	30.8	6.8±1.1	1.2±1.3E+03	1.5±4.0E-04	I
416141	359.9919	0.1567	15.72	13	15.0	10.7±1.3	8.2±3.3E+03	0.0±0.0E-00	II
417301	359.8509	0.0685	0.60	293	29.1	6.2±1.5	1.4±1.5E+03	1.0±7.0E-08	II
419271	359.5965	-0.0903	0.00	1079	39.6	9.0±1.0	3.7±1.4E+03	1.1±4.3E-04	I
420459	359.6870	-0.0368	12.33	26	15.0	13.1±0.9	1.4±0.2E+04	0.0±0.0E-00	II
421092	359.6650	-0.0513	0.02	417	32.7	6.9±1.0	1.3±1.1E+03	1.6±4.4E-04	I
421780	359.5573	-0.1183	0.00	649	33.0	5.6±1.9	1.1±1.5E+03	0.9±3.6E-04	I
431993	359.7828	0.0031	6.64	7	15.0	7.0±0.0	4.8±0.2E+02	2.7±3.2E-04	I
436449	359.6986	-0.0554	5.46	673	15.0	9.9±0.3	6.1±0.8E+03	0.0±0.0E-00	III
440627	359.8361	0.0218	2.03	2	15.0	7.9±0.0	7.5±0.0E+02	4.9±3.3E-04	I
441299	359.7169	-0.0521	6.74	53	15.0	8.5±0.7	3.8±1.1E+03	0.0±0.0E-00	II
442291	359.7696	-0.0215	5.83	5	15.0	7.2±0.2	1.9±0.2E+03	0.6±1.1E-07	II
442669	359.6671	-0.0848	11.06	5	15.0	10.3±0.1	6.8±0.3E+03	0.0±0.0E-00	II
447593	359.8057	-0.0080	4.63	6	15.0	8.5±0.0	3.6±0.0E+03	0.0±0.0E-00	II
448031	359.8111	-0.0054	12.85	10	15.0	8.3±0.7	2.9±1.5E+03	1.8±4.6E-05	I
454105	359.7053	-0.0798	0.00	332	34.0	8.4±2.3	4.5±5.9E+03	0.1±1.9E-04	I

Table 3—Continued

SST GC #	l	b	χ_{min}^2	nfits	$\langle A_v \rangle$	$\langle M_\star \rangle$	$\langle L_\star \rangle$	$\langle \dot{M}_{env} \rangle$	$\langle \text{Stage} \rangle$
454135	359.6046	-0.1414	0.01	328	33.1	5.9±1.9	1.2±1.7E+03	1.7±4.9E-04	I
457947	359.6273	-0.1336	0.08	736	31.3	6.5±0.9	1.0±0.6E+03	0.5±2.0E-04	I
458543	359.7303	-0.0716	0.19	102	31.2	7.3±0.9	2.0±1.0E+03	0.7±3.6E-04	I
460967	359.7678	-0.0526	7.90	4	15.0	7.3±0.0	2.0±0.0E+03	6.1±0.0E-09	II
462136	359.6277	-0.1401	1.96	66	15.3	6.3±1.4	1.4±1.6E+03	0.4±1.5E-05	II
462303	359.6423	-0.1314	4.23	23	15.0	5.7±0.2	2.3±0.5E+02	1.1±3.3E-04	I
464434	359.6721	-0.1166	8.13	10	15.0	7.8±0.7	2.7±1.0E+03	0.0±0.0E-00	III
466603	359.8973	0.0175	2.58	36	15.5	6.9±0.6	9.7±3.2E+02	0.8±1.6E-04	I
470861	359.8013	-0.0478	11.32	9	16.0	7.7±0.4	2.4±0.5E+03	3.4±3.0E-09	II
472034	359.7097	-0.1056	4.29	43	15.3	8.1±0.8	3.1±1.1E+03	0.0±0.0E-00	II
474477	359.8252	-0.0389	0.00	393	31.0	5.4±1.6	0.7±1.1E+03	1.6±4.5E-04	I
475651	359.7068	-0.1132	5.01	46	15.0	9.5±0.6	5.3±1.2E+03	0.0±0.0E-00	III
476516	359.7604	-0.0818	0.00	334	31.3	8.6±2.2	4.5±4.2E+03	1.2±5.6E-04	I
479032	359.6584	-0.1481	1.39	68	16.1	6.8±1.0	1.6±1.0E+03	0.3±2.6E-04	I
482056	359.9953	0.0529	0.00	594	33.7	8.1±1.3	1.7±1.0E+03	2.1±4.4E-04	I
487249	359.7847	-0.0839	5.60	25	15.0	10.6±0.9	7.8±1.8E+03	0.0±0.0E-00	II
487365	359.8346	-0.0536	9.18	45	15.0	8.8±0.6	4.1±1.0E+03	0.0±0.0E-00	II
487447	359.7735	-0.0911	1.25	84	16.4	5.9±0.5	1.0±0.2E+03	0.2±2.3E-04	I
487733	359.8448	-0.0480	7.91	17	15.0	9.6±0.3	5.9±0.6E+03	0.0±0.0E-00	II
491274	359.8231	-0.0669	8.84	31	15.0	8.1±0.8	3.1±1.1E+03	0.0±0.0E-00	II
493379	359.8663	-0.0438	5.65	43	15.2	9.6±0.5	5.9±1.2E+03	0.0±0.0E-00	II
493484	359.8327	-0.0645	6.83	488	16.2	10.0±0.4	6.4±0.9E+03	0.0±0.0E-00	II
496117	359.8746	-0.0431	8.53	25	15.0	10.5±1.0	7.5±2.1E+03	0.0±0.0E-00	II
496149	359.7832	-0.0990	2.07	11	15.6	10.4±2.1	3.6±3.0E+03	0.6±1.4E-03	I
498795	359.9022	-0.0305	0.01	304	30.3	8.3±1.7	3.4±3.0E+03	2.0±7.9E-04	I
503662	359.7937	-0.1044	0.00	255	29.1	6.5±1.5	1.7±1.6E+03	0.0±0.0E-00	II
506001	359.8503	-0.0735	12.05	3	15.0	6.8±0.0	5.1±0.0E+02	2.9±0.0E-04	I
509613	359.8985	-0.0496	0.00	374	33.8	8.3±2.3	4.2±4.5E+03	0.7±4.1E-04	I
513569	359.8789	-0.0677	0.00	403	23.2	5.4±0.6	4.5±2.4E+02	0.3±1.2E-04	I
514061	359.8771	-0.0696	4.17	24	15.1	7.3±0.5	2.1±0.8E+03	4.2±9.5E-07	II
523841	359.8422	-0.1062	0.03	260	34.5	5.6±1.5	7.5±1.1E+03	1.9±3.9E-04	I
526476	359.8701	-0.0933	13.89	26	15.0	8.7±0.6	3.9±1.0E+03	0.6±3.4E-06	II
551160	359.8313	-0.1552	2.95	60	15.8	6.1±0.7	1.0±0.4E+03	0.0±0.0E-00	II
562403	359.9172	-0.1204	5.29	7	15.0	7.1±0.2	1.8±0.2E+03	0.7±1.1E-06	II
569532	359.8820	-0.1529	5.27	37	15.0	10.1±0.4	6.5±0.8E+03	0.0±0.0E-00	III
573348	359.9211	-0.1350	0.00	766	27.0	6.7±1.4	1.6±1.4E+03	1.1±4.4E-04	I
577334	359.9021	-0.1528	3.66	7	15.9	6.1±0.2	2.4±0.2E+02	1.2±0.6E-04	I
580183	359.9629	-0.1201	0.08	107	30.2	7.6±0.8	2.0±1.4E+03	0.9±3.7E-04	I
585293	359.9357	-0.1445	0.05	33	24.2	10.5±1.6	7.9±4.1E+03	1.5±4.5E-06	II

Table 4. The Parameters of the SED Fits to Candidate YSOs in $l > 0^\circ$

SST GC #	l	b	χ_{min}^2	nfits	$\langle A_v \rangle$	$\langle M_\star \rangle$	$\langle L_\star \rangle$	$\langle \dot{M}_{env} \rangle$	$\langle \text{Stage} \rangle$
625950	0.4807	0.1243	2.90	2	15.0	8.8±0.1	1.4±0.2E+03	1.5±0.8E-03	I
630016	0.5217	0.1431	0.35	220	36.5	10.2±1.5	3.8±1.4E+03	0.4±1.1E-03	I
630178	0.3082	0.0130	1.89	43	15.6	6.7±0.4	1.0±0.6E+03	0.6±1.7E-04	I
630480	0.3268	0.0238	5.97	49	15.0	8.3±0.7	3.5±0.9E+03	0.0±0.0E-00	II
630841	0.3311	0.0258	0.00	1087	33.4	7.7±1.0	2.4±1.2E+03	1.0±4.2E-04	I
630883	0.1551	-0.0813	7.85	62	15.1	9.6±0.6	5.7±1.2E+03	0.0±0.0E-00	II
637548	0.5413	0.1433	6.75	7	15.0	6.2±0.3	2.8±0.4E+02	2.7±3.8E-04	I
639320	0.3763	0.0402	10.22	5	21.6	10.0±0.7	3.2±0.6E+03	7.4±2.7E-04	I
640649	0.5798	0.1618	0.00	806	35.8	5.3±1.4	8.8±0.1E+02	0.2±1.6E-04	I
640996	0.5520	0.1443	6.98	14	15.1	15.2±1.7	2.2±0.7E+04	0.0±0.0E-00	II
652737	0.4320	0.0529	3.45	10	15.0	6.9±0.0	1.5±0.0E+00	0.0±0.0E-00	III
656573	0.4443	0.0545	7.51	232	15.6	9.6±0.0	5.5±0.0E+00	0.0±0.0E-00	III
661922	0.1874	-0.1099	14.87	17	15.0	11.2±0.2	8.9±0.5E+03	0.0±0.0E-00	II
662019	0.1358	-0.1414	0.00	726	31.1	5.3±1.3	5.6±6.0E+02	1.5±3.8E-04	I
668833	0.4817	0.0582	0.00	327	33.6	4.8±1.2	6.1±9.0E+02	1.7±7.2E-09	II
673150	0.4771	0.0487	7.37	6	15.0	7.3±0.0	1.9±0.0E+03	0.0±0.0E-00	II
674497	0.4656	0.0395	0.64	58	22.0	6.2±0.9	3.8±1.9E+02	4.1±5.6E-04	I
676058	0.3440	-0.0367	0.00	670	33.8	6.1±1.7	1.2±1.3E+03	1.1±3.6E-04	I
686815	0.5895	0.0954	5.04	17	15.0	6.5±0.4	1.2±0.5E+03	1.2±2.7E-05	I
692917	0.3497	-0.0596	0.00	441	39.3	8.8±1.1	2.3±0.9E+03	3.0±7.4E-04	I
693461	0.4654	0.0097	0.00	953	30.4	5.7±1.2	9.7±7.8E+02	0.1±1.4E-09	II
697182	0.7048	0.1492	3.24	13	15.0	5.1±0.3	1.5±0.1E+02	3.4±2.8E-05	I
697485	0.4753	0.0094	8.75	3	15.0	5.5±0.0	1.5±0.0E+02	7.1±0.0E-05	I
698825	0.7023	0.1450	7.43	292	15.6	10.2±0.1	6.7±0.4E+03	0.0±0.0E-00	II
699821	0.7209	0.1549	5.57	54	20.7	10.1±1.0	6.8±2.3E+03	0.0±0.0E-00	II
701002	0.3521	-0.0708	0.00	268	31.9	7.2±1.9	2.5±2.7E+03	0.1±2.0E-04	I
705059	0.6518	0.1047	0.14	317	22.6	6.2±1.0	1.3±0.8E+03	0.1±2.5E-05	II
708923	0.3715	-0.0714	0.01	187	33.6	6.5±1.4	1.2±1.5E+03	1.7±4.0E-04	I
712604	0.7349	0.1432	11.32	2	15.0	5.5±0.0	1.5±0.0E+02	7.1±0.0E-05	I
719022	0.4264	-0.0541	0.00	831	33.0	7.7±0.9	2.5±1.2E+03	0.3±1.5E-04	I
719445	0.4921	-0.0148	0.37	236	39.1	10.7±2.2	4.2±2.0E+03	0.6±1.3E-03	I
720672	0.5318	0.0073	0.03	319	34.3	6.9±0.8	1.3±0.9E+03	1.5±4.3E-04	I
722141	0.5326	0.0056	0.22	89	43.8	9.4±1.3	2.6±0.8E+03	0.7±1.2E-03	I
725275	0.3765	-0.0941	0.01	263	32.1	5.9±1.4	0.8±1.1E+03	2.2±4.7E-04	I
726772	0.3766	-0.0965	7.54	20	15.0	8.8±0.7	3.8±1.7E+03	0.3±1.4E-04	I
728239	0.4561	-0.0508	0.32	129	26.0	7.8±2.0	3.0±3.1E+03	1.0±2.4E-04	I
730947	0.3978	-0.0908	2.71	24	15.7	8.0±0.9	3.3±1.3E+03	0.5±1.3E-05	II
734229	0.7824	0.1368	4.05	173	19.3	7.7±0.8	2.7±1.3E+03	0.0±0.0E-00	II
735664	0.4206	-0.0849	0.00	1570	28.6	8.6±1.0	3.4±1.4E+03	1.1±4.3E-04	I
735924	0.4521	-0.0663	3.94	7	15.0	8.5±0.0	3.6±0.0E+03	0.0±0.0E-00	II
736152	0.4168	-0.0880	0.20	73	21.7	6.0±0.7	9.3±5.8E+02	0.6±2.6E-04	I
738112	0.3738	-0.1175	0.50	281	16.3	6.4±0.8	1.3±0.6E+03	0.0±0.0E-00	II
738917	0.8269	0.1559	12.34	3	15.0	5.5±0.0	1.5±0.0E+02	7.1±0.0E-05	I
747205	0.6418	0.0293	11.93	29	15.0	14.6±0.0	1.9±0.0E+04	0.0±0.0E-00	III
748963	0.4127	-0.1127	0.00	638	30.3	5.6±1.4	7.2±8.0E+02	1.5±4.1E-04	I
749851	0.6742	0.0442	9.31	38	19.1	7.2±0.8	2.0±0.8E+03	0.0±0.0E-00	II

Table 4—Continued

SST GC #	l	b	χ^2_{min}	nfits	$\langle A_v \rangle$	$\langle M_\star \rangle$	$\langle L_\star \rangle$	$\langle \dot{M}_{env} \rangle$	$\langle \text{Stage} \rangle$
751713	0.6051	-0.0012	0.07	265	31.4	7.9±1.6	2.9±2.8E+03	1.3±4.8E-04	I
753072	0.8050	0.1175	2.25	12	15.0	5.9±0.4	4.0±0.9E+02	5.3±7.4E-05	I
754939	0.8335	0.1313	0.01	523	20.5	4.8±0.6	4.5±2.5E+02	0.2±4.0E-05	II
759523	0.4366	-0.1178	2.95	129	24.6	11.0±1.0	8.9±2.7E+03	0.0±0.0E-00	II
760167	0.4250	-0.1261	3.07	33	18.6	8.3±1.1	3.4±2.0E+03	0.9±3.8E-04	I
760268	0.7882	0.0938	0.00	295	32.7	5.3±1.8	0.9±1.3E+03	0.6±2.4E-04	I
762849	0.4837	-0.0957	0.00	676	29.7	6.3±1.5	1.5±1.9E+03	0.1±1.5E-04	I
763989	0.3742	-0.1642	0.00	613	30.4	6.2±1.8	1.5±2.0E+03	0.7±3.5E-04	I
764024	0.8377	0.1166	0.11	416	31.8	7.3±0.9	2.2±1.2E+03	0.4±1.3E-04	I
769807	0.6417	-0.0130	0.04	671	23.7	5.4±0.9	7.7±5.9E+02	0.3±5.1E-05	II
770318	0.3979	-0.1617	4.30	57	15.2	9.0±0.4	4.4±0.6E+03	0.0±0.0E-00	III
772097	0.7192	0.0294	0.00	548	41.3	8.7±1.0	3.1±1.0E+03	1.6±4.7E-04	I
772886	0.4015	-0.1644	0.22	66	28.3	7.3±1.4	2.2±1.8E+03	0.7±2.0E-05	II
773332	0.6102	-0.0389	0.00	216	36.5	7.5±0.8	2.1±0.9E+03	1.4±5.1E-04	I
776632	0.9188	0.1418	0.14	204	16.4	4.6±0.6	4.0±2.8E+02	0.7±3.5E-08	II
776865	0.7564	0.0429	3.25	36	15.8	4.1±0.3	0.2±6.9E+01	0.0±0.0E-00	II
779211	0.6142	-0.0477	0.02	109	35.9	8.5±0.9	2.9±1.3E+03	2.8±6.7E-04	I
780313	0.9184	0.1345	3.81	2672	15.0	14.6±0.0	1.9±0.0E+04	0.0±0.0E-00	III
784931	0.6437	-0.0405	0.71	120	44.4	9.0±2.0	4.9±4.8E+03	1.7±5.9E-04	I
785382	0.9154	0.1230	0.00	796	39.0	8.9±1.1	3.3±1.2E+03	1.6±5.5E-04	I
787884	0.6428	-0.0466	0.01	475	35.0	9.0±1.2	2.5±1.1E+03	2.8±7.2E-04	I
790413	0.5867	-0.0854	0.37	76	29.1	8.2±0.8	1.3±0.5E+03	3.8±7.3E-04	I
793536	0.6484	-0.0540	47.79	1	15.0	7.9±0.0	7.4±0.0E+02	1.5±0.0E-04	I
793867	0.6818	-0.0344	0.14	336	36.7	8.6±1.0	3.0±1.7E+03	2.0±6.1E-04	I
795418	0.6355	-0.0653	0.00	703	31.9	6.6±1.1	1.1±0.9E+03	1.6±4.3E-04	I
795658	0.5621	-0.1102	0.08	150	38.6	5.7±1.5	1.1±1.7E+03	1.3±4.5E-04	I
795914	0.8815	0.0826	0.39	467	35.6	5.1±1.0	0.6±1.1E+03	1.3±8.7E-05	I
796410	0.6606	-0.0520	0.04	339	32.0	7.5±1.3	2.0±1.8E+03	1.6±5.0E-04	I
797252	0.6810	-0.0413	0.00	405	30.1	7.3±2.0	2.6±3.2E+03	1.4±5.7E-04	I
801788	0.8674	0.0629	4.41	146	15.0	4.5±0.0	3.3±0.0E+02	0.0±0.0E-00	II
802032	0.8693	0.0635	0.00	1040	29.9	4.4±0.9	3.7±3.4E+02	0.1±2.6E-07	II
802748	0.7511	-0.0093	0.12	199	18.2	5.1±0.6	3.2±1.1E+02	0.4±1.5E-04	I
802877	0.8718	0.0634	2.99	14	15.0	3.8±0.3	1.7±0.5E+02	0.0±0.0E-00	II
804299	0.8768	0.0636	0.04	423	17.7	3.7±0.4	1.5±0.8E+02	1.3±4.8E-08	II
805200	0.6179	-0.0948	0.00	462	37.5	8.5±0.9	3.0±1.0E+03	2.1±6.9E-04	I
806191	0.6326	-0.0880	0.02	154	38.9	8.8±1.3	2.0±0.9E+03	0.6±1.1E-03	I
807365	0.9825	0.1211	0.00	502	29.2	6.0±1.5	1.3±1.6E+03	0.7±5.8E-09	II
807789	0.5456	-0.1440	0.00	510	29.4	6.3±1.9	1.6±2.2E+03	0.8±3.7E-04	I
809058	0.5288	-0.1569	8.77	9	15.0	7.6±0.7	2.4±0.8E+03	0.5±1.0E-06	II
809602	0.9572	0.1011	1.05	306	39.1	5.3±1.0	7.6±6.0E+02	0.1±1.1E-04	I
810562	0.6899	-0.0626	0.00	555	35.9	5.9±1.7	1.3±1.8E+03	0.4±2.3E-04	I
811158	0.5871	-0.1260	0.00	1127	37.9	9.4±1.1	4.5±1.7E+03	1.1±4.6E-04	I
811550	0.7552	-0.0252	0.02	615	26.2	6.4±0.7	8.6±4.3E+02	0.7±2.5E-04	I
812377	0.6003	-0.1205	0.12	390	40.8	8.5±0.8	2.9±1.2E+03	1.2±3.6E-04	I
814299	0.7259	-0.0485	0.02	1052	29.3	5.2±1.1	7.2±6.2E+02	0.3±9.9E-06	II
818720	0.7520	-0.0419	0.01	492	30.3	6.5±1.2	1.5±1.1E+03	0.0±0.0E-00	II

Table 4—Continued

SST GC #	l	b	χ^2_{min}	nfits	$\langle A_v \rangle$	$\langle M_\star \rangle$	$\langle L_\star \rangle$	$\langle \dot{M}_{env} \rangle$	$\langle \text{Stage} \rangle$
819806	0.5527	-0.1647	0.02	807	35.0	6.5±1.0	1.3±1.0E+03	0.3±1.2E-04	I
820972	0.8029	-0.0159	6.60	51	15.7	6.7±0.7	1.4±0.5E+03	0.9±4.4E-04	I
821060	0.5660	-0.1594	0.00	706	30.6	5.4±1.4	6.7±7.6E+02	1.3±3.9E-04	I
826501	0.7728	-0.0458	8.19	10	17.0	5.9±0.6	2.2±0.3E+02	4.0±3.6E-04	I
826931	0.9561	0.0640	3.85	69	15.5	5.2±0.4	6.1±1.8E+02	0.0±0.0E-00	II
828786	0.7263	-0.0789	0.06	520	27.2	4.4±0.8	3.6±2.4E+02	0.0±1.4E-05	II
829672	1.0693	0.1266	0.00	985	27.2	4.3±0.7	3.1±2.5E+02	0.1±2.0E-05	II
830399	0.5877	-0.1661	0.38	172	16.8	4.1±0.8	1.2±1.0E+02	2.5±6.6E-05	I
830971	0.9619	0.0588	0.00	838	27.6	5.0±0.8	5.5±3.9E+02	0.1±3.3E-05	II
831103	1.0790	0.1294	7.16	14	15.0	6.4±0.6	1.0±0.6E+03	1.5±2.9E-05	I
831236	0.5899	-0.1665	9.66	1	15.0	6.0±0.0	2.1±0.0E+02	9.8±0.0E-05	I
837363	0.6703	-0.1307	0.13	378	22.3	4.8±1.0	1.7±1.0E+02	8.6±1.8E-04	I
839447	0.6195	-0.1657	0.01	635	41.8	11.1±1.4	8.0±2.6E+03	1.7±6.5E-04	I
841071	0.8188	-0.0487	0.02	438	35.2	6.7±1.1	1.2±1.0E+03	1.3±3.4E-04	I
842086	0.7590	-0.0869	6.51	85	22.8	9.8±0.8	6.1±1.5E+03	0.0±0.0E-00	II
844666	0.8868	-0.0152	8.10	9	46.8	9.8±1.9	6.4±3.8E+03	0.0±0.0E-00	II
848731	0.9049	-0.0128	2.85	11	15.0	3.9±0.2	1.2±0.4E+02	1.5±1.1E-08	II
849203	0.9969	0.0417	10.44	19	15.0	7.9±0.5	2.8±0.7E+03	0.0±0.0E-00	III
849731	0.9969	0.0405	22.12	3	15.0	6.6±0.0	4.6±0.0E+02	1.7±0.0E-05	I
850592	0.8439	-0.0537	0.04	162	33.8	9.2±1.0	4.6±1.6E+03	1.3±7.5E-04	I
853347	1.0547	0.0677	4.64	42	15.0	9.2±0.2	4.7±0.4E+03	0.0±0.0E-00	III
857133	1.0477	0.0553	0.00	213	34.1	7.3±0.7	1.8±0.9E+03	0.5±2.7E-04	I
857708	0.8444	-0.0687	4.52	5	15.0	6.0±0.3	2.4±0.4E+02	0.1±7.3E-05	I
860855	0.8333	-0.0820	2.64	10	15.0	6.9±0.0	1.5±0.0E+03	0.0±0.0E-00	III
861689	0.9902	0.0108	0.62	332	32.1	8.0±1.2	3.1±2.1E+03	0.6±8.6E-05	II
864818	0.8977	-0.0516	4.37	25	43.9	11.2±0.8	9.6±1.9E+03	0.0±0.0E-00	II
866280	0.8145	-0.1051	5.90	1156	15.0	6.6±0.1	1.3±0.1E+03	0.0±0.0E-00	III
868530	0.7986	-0.1198	1.88	65	15.0	6.0±0.5	1.0±0.3E+03	0.0±0.0E-00	III
869198	1.0000	0.0001	5.10	47	15.2	4.1±0.4	2.4±0.8E+02	1.0±6.7E-06	II
869219	0.8074	-0.1161	6.28	3	15.0	5.1±0.0	1.5±0.0E+02	4.6±0.0E-05	I
869244	0.9121	-0.0530	3.99	72	42.1	9.6±0.0	5.5±0.0E+03	0.0±0.0E-00	III
869472	0.9372	-0.0384	0.03	426	28.4	3.7±0.8	1.3±1.2E+02	0.3±1.8E-04	I
871019	0.7332	-0.1652	6.19	735	15.0	10.0±0.3	6.2±0.6E+03	0.0±0.0E-00	III
878691	0.8826	-0.0935	0.69	5	16.5	7.9±0.1	1.0±0.0E+03	3.4±5.5E-04	I
879350	1.0082	-0.0193	5.28	24	16.0	5.9±0.5	9.4±3.2E+02	0.0±0.0E-00	II
879793	0.7827	-0.1564	2.37	16	15.0	7.3±0.2	1.9±0.2E+03	1.6±0.4E-08	II
881125	0.7777	-0.1626	11.09	17	15.0	6.8±0.4	1.4±0.5E+03	2.1±5.7E-05	I
884709	0.9500	-0.0671	0.05	1169	28.5	3.5±0.7	1.5±1.4E+02	0.3±8.0E-06	II
884809	1.0370	-0.0149	4.32	7	15.0	5.5±0.0	1.7±0.1E+02	5.4±1.4E-05	I
887636	0.9713	-0.0612	3.59	9	15.3	5.9±0.6	2.5±0.3E+02	2.5±1.9E-04	I
891214	1.1138	0.0161	0.01	350	28.5	4.3±1.8	4.4±6.3E+02	1.2±2.6E-04	I
891918	1.0501	-0.0239	5.60	74	18.9	7.5±0.5	2.3±0.6E+03	0.0±0.0E-00	II
892828	0.8474	-0.1484	6.14	15	15.0	5.4±0.2	5.0±2.6E+02	1.7±2.5E-05	I
899543	1.1011	-0.0113	0.06	225	29.0	6.9±1.9	2.3±3.0E+03	0.9±4.0E-04	I
899611	0.9782	-0.0856	14.19	2	15.0	5.5±0.0	1.5±0.0E+02	7.1±0.0E-05	I

Table 5. Table of Sources* with $4.5\mu\text{m}$ Excess Emission

Source	Galactic l b	α_{J2000} h m s	δ_{J2000} ° ' "	Description
0	1.041-0.072	17 48 21.37	-28 05 00.7	point
1	0.955-0.786	17 50 56.34	-28 31 24.4	PN, extended?
2	0.868-0.697	17 50 23.32	-28 33 11.6	PN, point
3	0.826-0.211	17 48 23.59	-28 20 20.7	point
4	0.780-0.740	17 50 21.09	-28 39 03.2	PN, extended
5	0.707+0.408	17 45 42.73	-28 07 12.1	extinction of a dark cloud?
6	0.692-0.046	17 47 26.27	-28 22 06.7	extended
7	0.679-0.038	17 47 22.65	-28 22 31.6	point
8	0.667-0.037	17 47 20.60	-28 23 06.6	extended?
9	0.667-0.035	17 47 20.20	-28 23 05.7	point
10	0.665-0.054	17 47 24.28	-28 23 44.2	point
11	0.542-0.476	17 48 45.67	-28 43 10.9	point
12	0.517-0.657	17 49 24.74	-28 50 02.0	point
13	0.483-0.701	17 49 30.15	-28 53 06.8	point
14	0.477-0.727	17 49 35.52	-28 54 15.8	point
15	0.408-0.505	17 48 33.53	-28 50 56.1	extended
16	0.376+0.040	17 46 21.44	-28 35 37.9	extended
17	0.315-0.201	17 47 09.17	-28 46 17.8	point
18	0.167-0.445	17 47 45.38	-29 01 29.7	point?
19	0.091-0.663	17 48 25.71	-29 12 07.4	extended (+point)
20	0.084-0.642	17 48 19.86	-29 11 49.2	point
21	359.972-0.459	17 47 20.94	-29 11 54.0	extended (+point)
22	359.939+0.170	17 44 48.62	-28 53 59.1	extended
23	359.932-0.063	17 45 42.23	-29 01 38.7	point
24	359.907-0.303	17 46 35.04	-29 10 23.2	point
25	359.841-0.080	17 45 33.04	-29 06 49.4	point
26	359.614-0.245	17 45 39.29	-29 23 35.3	extended
27	359.599-0.032	17 44 47.27	-29 17 41.4	point
28	359.570+0.270	17 43 32.36	-29 09 40.8	point
29	359.437-0.102	17 44 40.46	-29 28 10.6	extended
30	359.300+0.033	17 43 48.85	-29 30 55.2	extended
31	359.199+0.041	17 43 32.35	-29 35 51.1	point
32	358.980+0.084	17 42 50.45	-29 45 42.2	2 points

* Visually identified from IRAC data. Many point sources may be multiple or extended sources at higher resolution.

Table 6. Table of 70 μm sources

source	l	b	α_{J2000}	δ_{J2000}	Flux (mJy)	S/N
1	0.95549	-0.78554	17 50 56.34	-28 31 24.4	446	9.19
22*	0.83579	+0.18444	17 46 52.86	-28 07 34.8	98080	43.32
3	0.82608	-0.21067	17 48 23.59	-28 20 20.7	–	–
5	0.70721	+0.40788	17 45 42.73	-28 07 12.1	–	–
10*	0.49639	+0.18764	17 46 04.07	-28 24 52.8	76270	39.54
14	0.47696	-0.72730	17 49 35.52	-28 54 15.8	–	–
24	359.90724	-0.30319	17 46 35.05	-29 10 23.2	–	–
28	359.57031	+0.26985	17 43 32.37	-29 09 40.8	2540	6.53
31	359.19896	+0.04097	17 43 32.35	-29 35 51.2	–	–

* Source # given is for table of methanol class II maser sources.

Table 7. Table of Methanol Class I Maser Sources

Source	Galactic l b	α_{J2000} h m s	δ_{J2000} °'''	v_{LSR} km s ⁻¹	Reference
0	359.617-0.252	17 45 41.32	-29 23 40.5	+19.3	S94,V00
1	359.898-0.066	17 45 38.21	-29 03 27.7	+21	H90,V00
2	359.982-0.075	17 45 52.01	-28 59 26.7	+44.5	H90,V00
3	0.682-0.026	17 47 20.19	-28 22 03.2	+54	M97
4	0.678-0.023	17 47 18.80	-28 22 08.3	+68	M97
5	0.677-0.023	17 47 18.71	-28 22 09.5	+70	M97
6	0.679-0.026	17 47 19.72	-28 22 09.5	+66	M97
7	0.679-0.026	17 47 19.74	-28 22 09.6	+66	M97
8	0.678-0.025	17 47 19.39	-28 22 10.7	+62	M97
9	0.670-0.021	17 47 17.43	-28 22 27.7	+63	M97
10	0.668-0.023	17 47 17.40	-28 22 38.0	+75	M97
11	0.667-0.026	17 47 18.11	-28 22 49.0	+78	M97
12	0.662-0.020	17 47 15.98	-28 22 50.5	+74	M97
13	0.667-0.027	17 47 18.33	-28 22 50.8	+78	M97
14	0.666-0.028	17 47 18.44	-28 22 55.7	+73	M97
15	0.665-0.030	17 47 18.84	-28 23 01.2	+64	M97
16	0.664-0.031	17 47 18.85	-28 23 04.8	+67	M97
17	0.661-0.027	17 47 17.39	-28 23 05.7	+46	M97
18	0.661-0.029	17 47 17.83	-28 23 11.1	+57	M97
19	0.655-0.035	17 47 18.43	-28 23 41.3	+71	M97
20	0.542-0.855	17 50 14.74	-28 54 50.6	+16.9	S94,V00

References: H90 = Haschick, Menten & Baan 1990 (44 GHz); S94 = Slysh et al. 1994 (44 GHz); M97 = Mehringer et al. 1997 (44 GHz, multiple sources in Sgr B2); V00 = Val'tts et al. 2000 (95 GHz)

Table 8. Table of Methanol Class II Maser Sources

Source	Galactic l b	α_{J2000} h m s	δ_{J2000} °'''	v_{LSR} km s ⁻¹	Reference
0	359.138+0.031	17:43:25.69	-29:39:17.4	-4.0	C96,W98
1	359.436-0.104	17:44:40.60	-29:28:16.0	-52.0	C96
2	359.436-0.102	17:44:40.21	-29:28:12.5	-53.6	C96
3	359.615-0.243	17:45:39.09	-29:23:30.0	+22.5	C96
4	359.970-0.457	17:47:20.17	-29:11:59.4	+23.0	C96
5	0.212-0.001	17:46:07.63	-28:45:20.9	+49.2	C96,W98
6	0.315-0.201	17:47:09.13	-28:46:15.7	+18.0	C96,W98
7	0.316-0.201	17:47:09.33	-28:46:16.0	+21.0	C96
8	0.376+0.040	17:46:21.31	-28:35:39.3	+37.0	C96
9	0.393-0.034	17:46:41.12	-28:37:05.1	+28.7	C96
10	0.496+0.188	17:46:03.96	-28:24:52.8	+0.8	C96,W98
11	0.645-0.042	17:47:18.67	-28:24:24.8	+49.1	C96
12	0.647-0.055	17:47:22.07	-28:24:42.3	+51.0	C96
13	0.651-0.049	17:47:21.13	-28:24:18.1	+48.0	C96
14	0.657-0.041	17:47:20.08	-28:23:47.1	+52.0	C96
15	0.665-0.036	17:47:20.04	-28:23:12.8	+60.4	C96,W98
16	0.666-0.029	17:47:18.66	-28:22:54.5	+72.2	C96
17	0.667-0.034	17:47:19.87	-28:23:01.3	+55.2	C96
18	0.672-0.031	17:47:20.03	-28:22:41.7	+58.2	C96
19	0.673-0.029	17:47:19.54	-28:22:32.6	+66.0	C96
20	0.677-0.025	17:47:19.29	-28:22:14.6	+73.4	C96
21	0.695-0.038	17:47:24.76	-28:21:43.2	+68.5	C96
22	0.836+0.184	17:46:52.86	-28:07:34.8	+3.5	C96,W98

References: C96 = Caswell 1996; W98 = Walsh et al. 1998

Table 9. The Parameters of SED Fits to 4.5 μ m Excess Sources near the Galactic Center

Green #	SST GC #	l	b	χ^2_{min}	nfits	$\langle A_v \rangle$	$\langle M_{\odot} \rangle$	$\langle L_{\odot} \rangle$	$\langle \dot{M} \rangle$	$\langle \text{Stage} \rangle$
g0	909173	1.0407	-0.0714	4.36	31	42.4	16.1 \pm 3.5	2.8 \pm 1.4E+04	0.0 \pm 0.0E+00	III
g3	913321	0.8262	-0.2108	11.45	4	43.6	10.6 \pm 0.0	7.6 \pm 0.0E+03	0.0 \pm 0.0E+00	II
g6	803187	0.6934	-0.0451	1.71	46	46.7	29.9 \pm 8.2	1.4 \pm 1.0E+05	1.3 \pm 0.6E-03	I
g7	794899	0.6796	-0.0376	7.33	20	7.5	9.4 \pm 1.2	3.1 \pm 0.7E+03	5.8 \pm 5.8E-04	I
g9	789483	0.6667	-0.0352	1.37	169	27.0	21.7 \pm 7.0	6.1 \pm 6.4E+04	1.6 \pm 1.5E-03	I
g10	798750	0.6655	-0.0535	1.96	12	5.1	9.5 \pm 0.7	2.0 \pm 0.5E+03	3.5 \pm 8.4E-04	I
g16	639320	0.3763	0.0402	10.22	9	14.0	10.1 \pm 0.6	3.2 \pm 0.6E+03	8.1 \pm 2.7E-04	I
g23	530763	359.9316	-0.0626	2.72	32	17.9	12.0 \pm 3.2	9.9 \pm 4.6E+03	1.3 \pm 0.6E-03	I
g25	506137	359.8412	-0.0793	2.76	39	12.5	10.3 \pm 1.2	5.5 \pm 1.9E+03	3.1 \pm 1.8E-04	I
g27	384307	359.5995	-0.0316	4.77	3	35.0	17.5 \pm 3.0	3.2 \pm 1.9E+04	2.2 \pm 3.1E-03	II
g29	366044	359.4362	-0.1017	3.18	70	22.3	14.1 \pm 2.4	1.9 \pm 0.9E+04	1.1 \pm 0.4E-03	I
g30	246410	359.3009	0.0334	1.87	11	9.8	8.9 \pm 0.7	1.7 \pm 0.5E+03	2.0 \pm 1.9E-04	I
g31	214725	359.1994	0.0419	2.75	69	35.9	14.4 \pm 4.6	2.3 \pm 1.6E+04	0.0 \pm 0.0E-00	II
g32	142942	358.9795	0.0840	0.00	374	10.9	10.5 \pm 6.0	0.8 \pm 1.4E+04	0.7 \pm 1.0E-03	I

Table 10. The Parameters of SED Fits to $4.5\mu\text{m}$ Excess Sources foreground to the Galactic Center

Green #	SST GC #	l	b	χ_{min}^2	nfits	$\langle A_v \rangle$	$\langle M_\star \rangle$	$\langle L_\star \rangle$	$\langle \dot{M}_{env} \rangle$	$\langle \text{Stage} \rangle$
g1	1060982	0.9555	-0.7853	0.96	12	5.6	2.4 ± 0.6	$2.4 \pm 0.7\text{E}+01$	$6.2 \pm 2.4\text{E}-06$	I
g2	1043897	0.8679	-0.6963	1.97	547	33.1	5.5 ± 1.3	$8.0 \pm 5.7\text{E}+02$	$1.0 \pm 3.0\text{E}-05$	I
g4	1042278	0.7800	-0.7395	0.77	161	10.3	6.9 ± 1.9	$8.9 \pm 8.0\text{E}+02$	$9.5 \pm 6.3\text{E}-05$	I
g5	532335	0.7062	0.4075	1.11	89	4.7	6.0 ± 3.0	$1.7 \pm 4.4\text{E}+03$	$1.2 \pm 1.4\text{E}-04$	I
g11	946558	0.5418	-0.4759	0.25	152	5.0	5.2 ± 2.5	$0.7 \pm 2.4\text{E}+03$	$1.1 \pm 1.2\text{E}-04$	I
g12	992035	0.5172	-0.6569	0.00	2643	9.9	2.1 ± 1.2	$3.1 \pm 3.4\text{E}+01$	$3.4 \pm 7.3\text{E}-05$	I
g13	997790	0.4835	-0.7004	1.82	4	4.7	9.9 ± 1.7	$3.3 \pm 2.5\text{E}+03$	$0.6 \pm 1.0\text{E}-03$	I
g14	1003258	0.4771	-0.7268	1.69	24	4.9	7.4 ± 1.7	$1.0 \pm 1.3\text{E}+03$	$2.7 \pm 1.4\text{E}-04$	I
g15	929122	0.4084	-0.5042	0.31	45	10.3	14.3 ± 4.2	$1.3 \pm 0.8\text{E}+03$	$1.0 \pm 0.4\text{E}-03$	I
g17	764611	0.3153	-0.2010	0.66	75	11.6	12.7 ± 2.6	$1.0 \pm 0.2\text{E}+04$	$1.0 \pm 2.8\text{E}-04$	I
g18	842427	0.1667	-0.4455	1.15	43	19.5	14.0 ± 4.3	$1.7 \pm 1.0\text{E}+04$	$2.1 \pm 1.2\text{E}-03$	I
g19	916902	0.0915	-0.6624	6.10	45	4.4	5.5 ± 1.3	$2.7 \pm 1.9\text{E}+02$	$1.5 \pm 1.4\text{E}-04$	I
g20	906570	0.0842	-0.6415	4.54	33	15.2	7.3 ± 1.3	$9.3 \pm 7.7\text{E}+02$	$2.8 \pm 2.0\text{E}-04$	I
g21B	789457	359.9695	-0.4573	0.38	135	23.7	23.8 ± 6.6	$4.4 \pm 5.5\text{E}+04$	$0.5 \pm 1.1\text{E}-03$	I
g21A	788629	359.9700	-0.4554	0.73	7648	13.9	11.8 ± 2.5	$1.1 \pm 0.7\text{E}+04$	$0.8 \pm 3.1\text{E}-04$	I
g22	387542	359.9386	0.1709	0.01	396	8.3	4.9 ± 1.8	$1.8 \pm 0.9\text{E}+03$	$3.2 \pm 5.2\text{E}-04$	I
g24	676294	359.9072	-0.3026	0.44	50	8.6	6.3 ± 2.5	$2.0 \pm 0.7\text{E}+03$	$3.3 \pm 2.4\text{E}-04$	I
g26	523105	359.6148	-0.2438	3.63	3447	0.0	7.1 ± 0.9	$0.0 \pm 0.0\text{E}+00$	$0.0 \pm 0.0\text{E}+00$	I
g28	214738	359.5701	0.2704	1.16	148	4.2	4.0 ± 1.3	$1.1 \pm 0.8\text{E}+02$	$6.0 \pm 6.0\text{E}-05$	I